Supporting Information:

Gold(III) Macrocycles: Nucleotide-Specific Unconventional Catalytic Inhibitors of Human Topoisomerase I

Kate J. Akerman[1], Alexander M. Fagenson[2], Vidusha Cyril[2], Michael Taylor[2], Mark T. Muller[2], Matthew P. Akerman[1], and Orde Q. Munro[1,†]*

*[1]School of Chemistry and Physics, University of KwaZulu-Natal, Private Bag X01, Scottsville, Pietermaritzburg, 3209, South Africa, [2]College of Medicine, Biomedical Research, University of Central Florida, 6900 Lake Nona Boulevard, Orlando, FL 32827, USA; [†]Visiting Fulbright Scholar to the University of Central Florida; *e-mail: munroo@ukzn.ac.za*

The current document contains supporting information for compounds **1**–**5**.

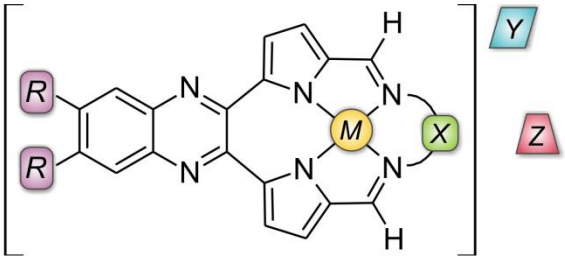

	M	X	R	Y	Z
1, **6**, **7**	Au, 2H, Ni	$-CH_2CH_2CH_2-$	H	+, 0, 0	PF_6^-, 0, 0
2a, **2b**	Au, Au	$-CH_2C(CH_3)_2CH_2-$	H	+, +	PF_6^-, $CF_3SO_3^-$
3	Au	$-CH_2(CH_2)_2CH_2-$	H	+	PF_6^-
4	Au	$-CH_2CHClCH_2-$	H	+	PF_6^-
5	Au	$-CH_2CH_2CH_2-$	CH_3	+	PF_6^-

Figure S1. Structures of Au^{3+} complexes **1**–**5**, free-base **6**, and Ni^{2+} complex **7**.

1. Experimental Section

1.1 Synthesis

1.1.1 General Information

All solvents were purified with a Pure Solv™ Solvent Purification System (Innovative Technology) before use. Chemical synthons and solvents for NMR spectroscopy were from Aldrich and used as supplied without further purification.

Electronic spectra were recorded using a Shimadzu UVPC-1800 double beam UV-vis scanning spectrometer with acetonitrile, DMSO or DMSO-buffer mixtures (15% DMSO in TRIS-HCl buffer at pH 7.0) as the solvent (1.0 cm path length cuvette). FTIR spectra were recorded on solid crystalline samples with a Bruker Alpha FTIR spectrophotometer fitted with a diamond ATR (32 scans, spectral resolution = 1.0 cm^{-1}). ^{1}H and ^{13}C NMR spectra of the compounds dissolved in $CDCl_3$ or DMSO-d_6 were recorded with a 500 MHz BrukerAvance III spectrometer equipped with an Oxford magnet (11.744 T) or a 400 MHz BrukerAvance III equipped with a Bruker magnet (9.395 T) and autosampler accessory. The proton and carbon NMR spectra were assigned with the use of DEPT and 2D COSY and HSQC data. For protons attached to nitrogen atoms (free ligands), DFT-calculated shielding tensors were used to assign the experimental proton chemical shifts. Mass spectrometry: samples were analysed using positive electrospray ionization (ESI+) on a Waters LCMS TOF LCT Premier spectrometer. Fluorescence spectra were recorded with a Photon Technologies Int. (PTI) fluorescence spectrometer controlled by Felix 32© Version 1.1 software (PTI) at 25.0 ± 0.1 °C. A quartz emission sample cell (1 cm path length) served as the solution sample holder. Steady-state emission spectra were recorded using PTI's XenoFlash™ 300 Hz pulsed light source and gated emission scans with a delay of 95 μs, an integration window time of 100 μs and 45 pulses per channel (shots). The detector used was PTI's model 814 analog photomultiplier detector.

1.1.2 Synthetic Methods

The macrocyclic ligands for complexes **1**–**5** were synthesized following the method described by Wang *et al.*[1] Typical yields were within 5% of the reported values; all characterization data were consistent with the literature. Gold(III) chelates were synthesized by direct metalation of the free base macrocycle (Route A, Figure S2) or a metal-templated Schiff base condensation reaction (Route B).[2]

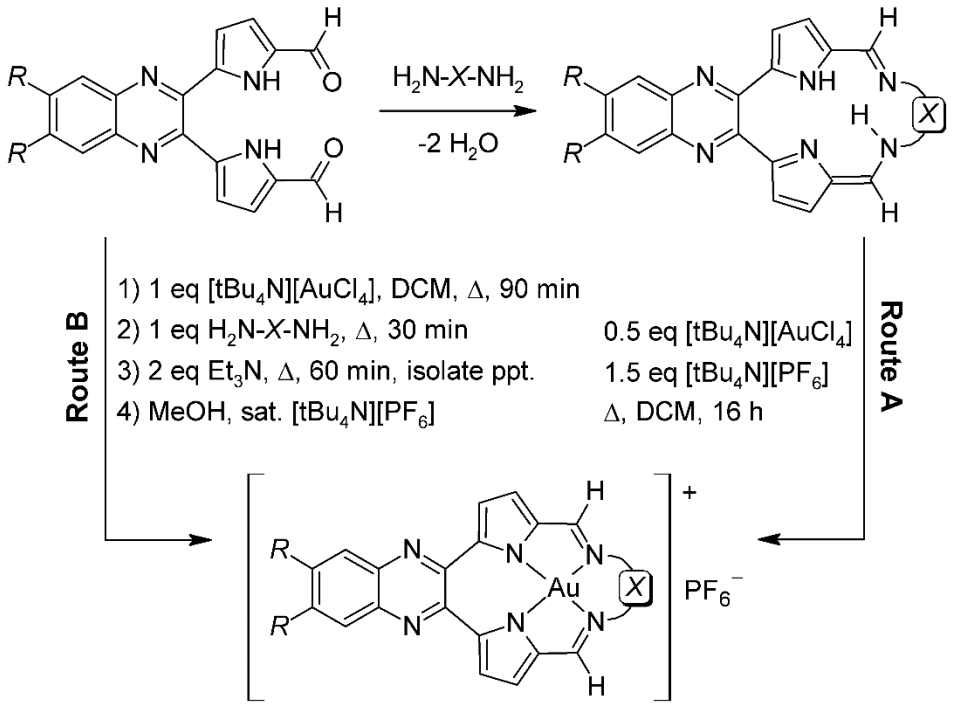

Route A: X = -$CH_2CH_2CH_2$-

Route B: X = -$CH_2(CH_2)_2CH_2$-, -$CH_2C(CH_3)_2CH_2$-, -$CH_2CHClCH_2$-

Figure S2. Synthetic routes to macrocyclic Au^{3+} complexes **1**–**5**.[2] Route A depicts a conventional metalation reaction between a pre-formed macrocycle and a lipophilic Au^{3+} salt under gentle reaction conditions that limit reduction of the Au^{3+} salt to metallic gold. The method primarily works for the propyl-bridged species, **1**. Route B depicts a more general metal-templated synthesis in which the bis(pyrrole-2-carbaldehyde) precursor is reacted with the lipophilic Au^{3+} salt prior to ring closure with the desired bridging diaminoalkane. Compounds **2**–**5** were prepared in acceptable yields using this method as detailed below. (*R* is defined in Figure S1.)

Preliminary characterization data for **1**, **2a**, and **3** were reported as part of our earlier patent application.[2] Full characterization details for these compounds and all other novel compounds of this study are given below along with exemplary spectral data for the gold(III) macrocycles and selected free base macrocycles.

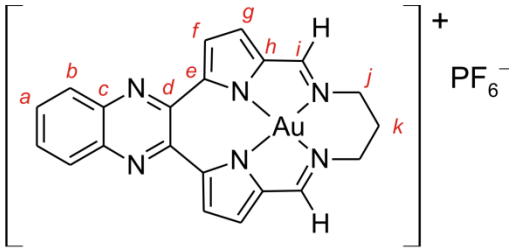

1

Compound 1: 12,13-dihydro-14*H*-6,9:17,20-diepimino[1,6]diazacyclo-heptadecino[12,13-β]quinoxalinato]-gold(III) hexafluorophosphate(V). As described earlier,[2] a solution of *tert*-butylammoniumtetrachloroaurate(III) (80 mg, 0.138 mmols) and *tert*-butylammonium hexafluorophosphate(V) (160 mg, 0.414 mmols) in dichloromethane (15 mL) was added dropwise to the free ligand, 12,13-dihydro-14*H*-6,9:17,20-diepimino[1,6]diazacyclo-heptadecino [12,13-β]-quinoxaline (99 mg, 0.275 mmols) in dichloromethane (20 mL). The solution was refluxed for 16 hours. Over this time a precipitate formed which was filtered, washed with dichloromethane and dried to afford a brick red powder of **1** (44 mg, 37%). Crystals suitable for single crystal X-ray diffraction were grown by vapour diffusion of diethylether into a benzonitrile solution of the product. ^{1}H NMR: (500 MHz, DMSO-d_6) δ 2.43 (q, br, 2H, ***k***), 3.96 (t, br, 4H, ***j***), 7.35 (d, $^{3}J_{HH}$ = 4.4 Hz, 2H, ***f***), 7.91 (d, $^{3}J_{HH}$ = 4.4 Hz, 2H, ***g***), 7.96-7.80 (dd, $^{4}J_{HH}$ = 3.3 Hz, $^{3}J_{HH}$ = 6.2 Hz, 2H, ***a***), 8.11-8.13 (dd, $^{4}J_{HH}$ = 3.3 Hz, $^{3}J_{HH}$ = 6.2 Hz, 2H, ***b***), 8.80 (s, 2H, ***i***). ^{13}C NMR: (125.7 MHz, DMSO-d_6) δ 34.32 (***k***), 51.86 (***j***), 119.34 (***g***), 123.06 (***f***), 129.03 (***b***), 132.24 (***a***), 136.28 (***d***), 139.62 (***h***), 139.95 (***c***), 148.15 (***e***), 163.71 (***i***). IR (cm^{-1}): 2955 (br), 1649 (m), 1572 (w), 1472 (w), 1400 (m), 1294 (m), 1115 (m), 1068 (w), 832 (s), 760 (s), 664 (w), 497 (s), 424 (m). UV-vis: (CH_3CN) λ_{max} [nm] (ε/M^{-1} cm^{-1}): 246 (23 346), 309 (30 077), 346 (18 001), 373 (15 237), 455 (12 041). HRMS (*m/z*): [M^{+}] calcd. for $C_{21}H_{16}N_6Au$, 549.1102; found, 549.1104.

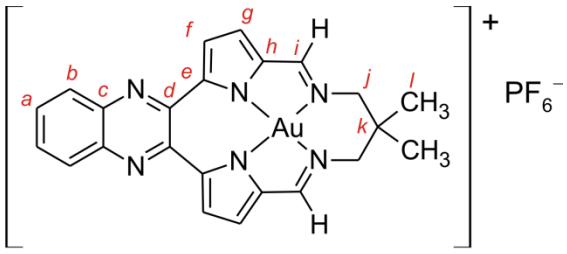

2a

Compound 2a: {12,14-dihydro-13,13-dimethyl-6,9:17,20-diepimino[1,6]diazacyclo-heptadecino[12,13-β]quinoxalinato}gold(III) hexafluorophosphate(V). 2,3-Bis(5'-formylpyrrol-2'-yl)quinoxaline, alternatively named 5,5'-quinoxaline-2,3-diylbis(1*H*-pyrrole-2-carbaldehyde), was synthesized by the literature method[1]. As described earlier,[2] a solution of 2,3-bis(5'-formylpyrrol-2'-yl)quinoxaline (54 mg, 0.172 mmols) in CH_2Cl_2 (10 mL) was added dropwise to *tert*-butylammoniumtetrachloroaurate(III) (100 mg, 0.172 mmols) in CH_2Cl_2 (20 mL). The solution was heated under reflux for 90 min before the addition 1,3-diamino-2,2-dimethylpropane

(18 mg, 0.172 mmols); immediate precipitation of a yellow solid indicated macrocycle formation. The reaction mixture was heated under reflux for a further 30 min prior to adding triethylamine (35 mg, 0.344 mmols), which led to the precipitate turning orange. After further reflux (1 h), the orange solid (chloride salt) was isolated and dried. To the orange solid dissolved in methanol was added a saturated aqueous solution of ammonium hexafluorophosphate(V), which precipitated the Au^{3+} complex cation as its PF_6^- salt. The precipitate was filtered and dried to afford an orange powder of **2a** (45 mg, 36%). ^{1}H NMR: (500 MHz, DMSO-d_6) δ 1.19 (s, 6H, ***l***), 3.72 (s, 4H, ***j***), 7.44 (d, $^3J_{HH}$ = 4.4 Hz, 2H, ***f***), 7.97-7.99 (dd, $^4J_{HH}$ = 3.3 Hz, $^3J_{HH}$ = 6.3 Hz, 2H, ***a***), 7.99 (d, $^3J_{HH}$ = 4.4 Hz, 2H, ***g***), 8.17-8.19 (dd, $^4J_{HH}$ = 3.3 Hz, $^3J_{HH}$ = 6.3 Hz, 2H, ***b***), 8.83 (s, 2H, ***i***). ^{13}C NMR: (125 MHz, DMSO-d_6) δ 23.59 (***l***), 43.05 (***k***), 61.57 (***j***), 119.35 (***g***), 123.39 (***f***), 129.09 (***b***), 132.31 (***a***), 136.73 (***d***), 139.67 (***h***), 140.03 (***c***), 148.43 (***e***), 164.56 (***i***). IR (cm^{-1}): 1569 (m), 1471 (w), 1405 (m), 1339 (w), 1238 (w), 1107 (m), 835 (s), 557 (m), 433 (m). UV-vis: (CH_3CN) λ_{max} [nm] (ε/M^{-1} cm^{-1}): 230 (17 642), 249 (14 463), 309 (16 131), 348 (8 795), 375 (8 680), 458 (6 640), 481 (6 360). HRMS (*m/z*): [M$^+$] calcd. for $C_{23}H_{20}N_6Au$, 577.1415; found, 577.1416.

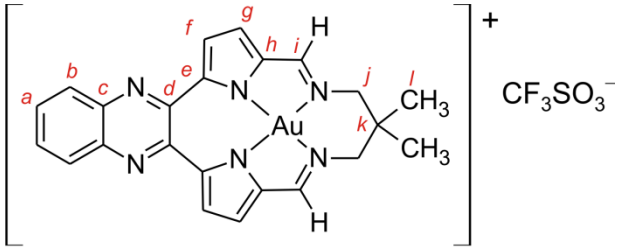

2b

Compound 2b: {12,14-dihydro-13,13-dimethyl-6,9:17,20-diepimino[1,6]diazacyclo-heptadecino[12,13-β]quinoxalinato}gold(III) triflate. Since **2a** was difficult to crystallize, we prepared the $CF_3SO_3^-$ salt **2b** by using a saturated aqueous solution of lithium trifluoromethanesulfonate instead of ammonium hexafluorophosphate(V) to precipitate the Au^{3+} complex of the macrocycle from the reaction solution as described above. Compound **2b** was isolated and dried as for **2a** (48 mg, 38%, orange powder). Single crystals suitable for X-ray diffraction were grown by diffusion of diethylether into a solution of **2b** dissolved in acetonitrile. ^{1}H NMR: (500 MHz, DMSO-d_6) δ 1.19 (s, 6H, ***l***), 3.71 (s, 4H, ***j***), 7.47 (d, $^3J_{HH}$ = 4.4 Hz, 2H, ***f***), 7.97-7.99 (dd, $^4J_{HH}$ = 3.3 Hz, $^3J_{HH}$ = 6.5 Hz, 2H, ***a***), 8.02 (d, $^3J_{HH}$ = 4.4 Hz, 2H, ***g***), 8.19-8.21 (dd, $^4J_{HH}$ = 3.4 Hz, $^3J_{HH}$ = 6.4 Hz, 2H, ***b***), 8.85 (s, 2H, ***i***). ^{13}C NMR: (125 MHz, DMSO-d_6) δ 23.10 (***l***), 42.51 (***k***), 61.05 (***j***), 118.85 (***g***), 122.88 (***f***), 128.55 (***b***), 131.78 (***a***), 136.29 (***d***), 139.18 (***h***), 139.52 (***c***), 147.94 (***e***), 164.07 (***i***). ^{19}F NMR (377 MHz, DMSO-d_6) δ –77.74 (s, 3F, 99% $^{12}CF_3SO_3^-$), –77.87 (d, $^1J_{FC}$ = 322 Hz, 1% $^{13}CF_3SO_3^-$). IR (cm^{-1}): 2953 (w), 2922 (m), 2852 (m), 1570 (s), 1470 (m), 1406 (w), 1338 (m), 1258 (s), 1235 (s), 1144 (m), 1104 (m), 1027 (s), 841 (w), 788 (w), 767 (w), 664 (w), 635 (s), 572 (w), 516 (m), 432 (m). HRMS (*m/z*): [M$^+$] calcd. for $C_{23}H_{20}N_6Au$, 577.1415; found, 577.1413.

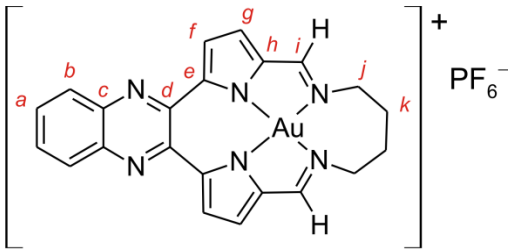

3

Compound 3: (12,13,14,15-tetrahydro-6,9:18,21-diepimino[1,6]diazacycloctadecino[12,13-b]quinoxalinato]gold(III) hexafluorophosphate(V). This complex was prepared by the same method[2] used for **2** with 1,4-diaminobutane (15.2 mg, 0.172 mmols) to give a brown powder of **3** (20 mg, 16%). ^{1}H NMR: (500 MHz, DMSO-d_6) δ 2.04 (br, 4H, ***k***), 4.32 (br, 4H, ***j***), 7.46 (d, $^{3}J_{HH}$ = 4.4 Hz, 2H, ***f***), 7.95-7.97 (dd, $^{4}J_{HH}$ = 3.3 Hz, $^{3}J_{HH}$ = 6.3 Hz, 2H, ***a***), 8.06 (d, $^{3}J_{HH}$ = 4.4 Hz, 2H, ***g***), 8.17-8.18 (dd, $^{4}J_{HH}$ = 3.3 Hz, $^{3}J_{HH}$ = 6.3 Hz, 2H, ***b***), 8.74 (s, 2H, ***i***). ^{13}C NMR: (125 MHz, DMSO-d_6) δ 24.21 (***k***), 55.94 (***j***), 119.43 (***g***), 122.77 (***f***), 129.05 (***b***), 132.22 (***a***), 136.17 (***d***), 140.15 (***h***), 140.24 (***c***), 148.43 (***e***), 165.34 (***i***). IR (cm^{-1}): 2964 (w), 1590 (m), 1400 (m), 1354 (m), 1100 (m), 1059 (m), 829 (s), 555 (s), 446 (w). UV-vis: (CH_3CN) λ_{max} [nm] (ε/M^{-1} cm^{-1}): 244 (16 439), 306 (19 364), 347 (13 712), 370 (13 425), 449 (9 825). HRMS (*m/z*): [M^{+}] calcd. for $C_{22}H_{18}N_6Au$, 563.1259; found, 563.1265.

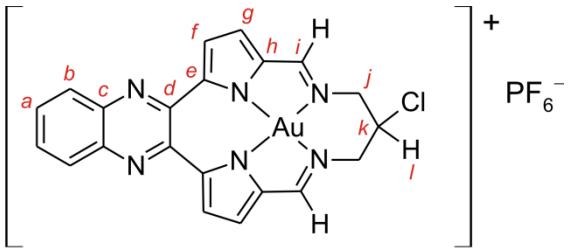

4

Compound 4: 13-chloro-12,14-dihydro-6,9:17,20-diepimino[1,6]diazacyclo-heptadecino-[12,13-β]quinox–alinato}gold(III) hexafluorophosphate(V). To a solution of *tert*-butyl-ammoniumtetrachloroaurate (100 mg, 0.172 mmol) in dichloromethane (20 mL), 2,3-bis(5'-formylpyrrol-2'-yl)quinoxaline (54 mg, 0.172 mmol) in dichloromethane (10 mL) was added dropwise before refluxing the reaction mixture for 90 min. Compound **4b** (32 mg, 0.172 mmol), 2-chloro-1,3-diaminopropane dihydrochloride,[2] was ground together with sodium carbonate (36 mg, 0.344 mmol) using a mortar and pestle until a paste formed. Ethanol was added to extract the product and the mixture was filtered. The filtrate was added to the gold solution and it was refluxed for a further 30 min before triethylamine (35mg, 0.344 mmol) was added. The solution turned a deep orange colour and was refluxed for a further hour. A saturated solution of ammonium hexafluorophosphate(V) was added to the solution which was left undisturbed overnight. Compound **4** precipitated as a red powder, which was filtered and dried (7 mg, 6 %). ^{1}H NMR: (400 MHz, DMSO-d_6) 4.23-4.28 (dd, $^{4}J_{HH}$ = 4.3 Hz, $^{3}J_{HH}$ = 14.3 Hz, 2H, ***j***), 4.39-4.43 (d, $^{3}J_{HH}$ = 14.3 Hz, 2H, ***j***), 5.38 (s, 1H, ***k***), 7.57 (d, $^{3}J_{HH}$ = 4.3 Hz, 2H, ***f***), 7.98-8.01 (dd, $^{4}J_{HH}$ = 3.2 Hz, $^{3}J_{HH}$ = 6.2 Hz, 2H, ***a***), 8.09 (d, $^{3}J_{HH}$ = 4.3 Hz, 2H, ***g***), 8.21-8.24 (dd, $^{4}J_{HH}$ = 3.2 Hz, $^{3}J_{HH}$ = 6.2 Hz, 2H, ***b***), 8.99 (s, 2H,***i***). ^{13}C NMR: (100

MHz, DMSO-d_6) 56.06 (***k***), 61.78 (***j***), 119.79 (***g***), 124.04 (***f***), 129.10 (***b***), 132.43 (***a***), 136.61 (***d***), 139.51 (***h***), 140.06 (***c***), 149.21 (***e***), 165.19 (***i***). IR: (cm^{-1}) 2964 (w), 1569 (m) 1400 (m), 1335 (m), 1262 (m), 1235 (m), 1085 (m), 828 (s), 662 (m), 556 (s), 496 (m), 431 (m). UV-vis: (CH_3CN) λ_{max} [nm] ($\varepsilon/M^{-1}\ cm^{-1}$): 246 (21 525), 308 (26 968), 348 (15 730), 376 (16 424), 455 (12 038), 481 (11 542). HRMS (*m/z*): [M^+] calcd. for $C_{21}H_{15}N_6ClAu$, 583.0712; found, 583.0717.

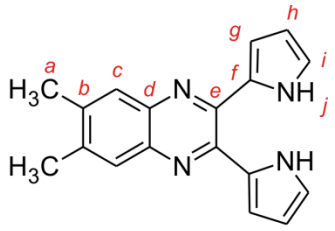

5a

Compound 5a: 6,7-dimethyl-2,3-di-1*H*-pyrrol-2-ylquinoxaline. A solution of 4,5-dimethyl-benzene-1,2-diamine (902 mg, 6.62 mmol) in glacial acetic acid (30 mL) was added to 1,2-bis(1*H*-pyrrole-2-yl)ethane-1,2-dione (570 mg, 3.03 mmol) in acetic acid (70 mL) with stirring. The solution was then refluxed under an atmosphere of nitrogen for 90 min before removing the majority of acetic acid under vacuum. The residue was dissolved in a mixture of water (30 mL) and dichloromethane (30 mL). The organic phase was separated off and the aqueous phase was extracted with dichloromethane (2 × 20 mL). The combined organic phases were washed with saturated aqueous sodium bicarbonate solution (50 mL), water (50 mL) then brine (50 mL) and dried over anhydrous magnesium sulfate, filtered and evaporated to dryness. The crude product was purified using silica gel column chromatography (dichloromethane eluent) and recrystallized from dichloromethane/hexane to afford a yellow crystalline powder of 6,7-dimethyl-2,3-di-1*H*-pyrrol-2-ylquinoxaline (625 mg, 66%). ^{1}H NMR (500 MHz, DMSO-d_6): δ 2.45 (s, 6H, ***a***), 6.10-6.12 (m, 2H, ***h***), 6.12-6.14 (m, 2H, ***g***) 6.93-6.95 (m, 2H, ***i***), 7.71 (s, 2H, ***c***), 11.41 (br, 2H, ***j***). ^{13}C (125 MHz, DMSO-d_6): δ 20.33 (***a***), 109.21 (***h***), 111.40 (***g***), 121.27 (***i***), 127.56 (***c***), 129.34 (***b***), 138.83 (***f***), 139,67 (***d***), 144.75 (***e***). IR (cm^{-1}): 3261 (br), 1546 (w), 1428 (m), 1128(m), 1037(m), 899 (m), 870 (m), 826 (m), 722 (s), 603 (m), 488 (m), 408 (w). HRMS (*m/z*): [M^+] calcd. for $C_{18}H_{17}N_4$, 289.1453; found, 289.1450.

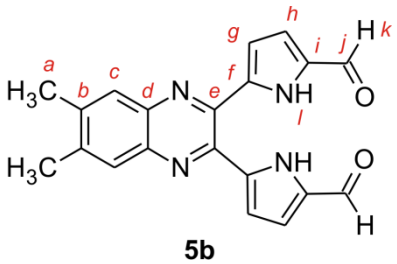

5b

Compound 5b: 5,5'-(6,7-dimethylquinoxaline-2,3-diyl)bis(1*H*-pyrrole-2-carbaldehyde). Under an atmosphere of nitrogen, phosphorus oxychloride (240 µL, 2.57 mmol) was added to

dimethylformamide (454 µL, 5.86 mmol) at 0 °C. After stirring the solution for 10 min at room temperature, 1,2-dichloroethane (3 mL) was added. A solution of 6,7-dimethyl-2,3-di-1*H*-pyrrol-2-ylquinoxaline (312 mg, 1.00 mmol, **5a**) in 1,2-dichlorethane (15 mL) was then added to the reaction mixture over a 10 min period. The reaction mixture was then refluxed for 30 min before being cooled to 0 °C whereupon a saturated aqueous solution of sodium acetate (3 mL) was then added. The mixture was refluxed for a further 30 min and, once cooled to room temperature, was washed with dichloromethane (3 × 20 mL). The combined organic phases were washed with water (30 mL) and brine (30 mL). The organic phase was dried over anhydrous magnesium sulfate, filtered and evaporated to dryness. The crude product was purified using silica gel column chromatography (methanol/dichloromethane eluent, 1:100) and recrystallized from dichloromethane/hexane to afford a yellow crystalline powder of 5,5'-(6,7-dimethylquinoxaline-2,3-diyl)bis(1*H*-pyrrole-2-carbaldehyde) (285 mg, 83%). ^{1}H NMR (500 MHz, $CDCl_3$): δ 2.49 (s, 6H, ***a***), 6.72-6.74 (m, 2H, ***g***), 6.94-6.96 (m, 2H, ***h***), 7.77 (s, 2H, ***c***), 9.62 (s, 2H, ***k***), 10.40 (br, 2H, ***l***). ^{13}C (125 MHz, $CDCl_3$) δ 20.74 (***a***), 113.86 (***g***), 120.98 (***h***), 128.00 (***c***), 133.95 (***i***), 135.68 (***f***), 139.85 (***d***), 141.74 (***b***), 142.23 (***e***), 179.69 (***j***). IR (cm^{-1}): 3165 (br), 1651 (s), 1547 (m), 1485 (m), 1350 (m), 1253 (m), 1197 (s), 1044 (w), 752 (m) 628 (w), 489 (w), 407 (w). HRMS (*m/z*): [Na-M$^+$] calcd. for $C_{20}H_{16}N_4O_2Na$, 367.1171; found, 367.1171.

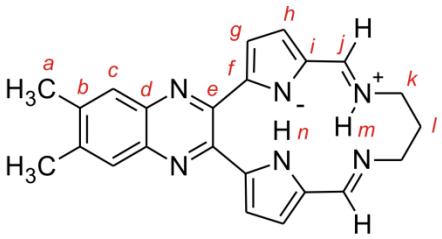

5c

Compound 5c. Triethylamine (80 µL) was added to 5,5'-(6,7-dimethylquinoxaline-2,3-diyl)bis(1*H*-pyrrole-2-carbaldehyde, **5b**) (69 mg, 0.2 mmol) in dry methanol (40 mL) and the reaction was stirred under reflux for 30 min. After this time, 1,3-diaminopropane (15 mg, 0.2 mmol) in dry methanol (2 mL) was added dropwise to the solution which was then refluxed for an additional 2 hours resulting in the precipitation of an orange solid of **5c** (55 mg, 72 %). ^{1}H NMR: (500 MHz, DMSO) 2.06 (m, br, 2H, ***l***), 2.49 (s, 6H, ***a***), 4.02 (m, br, 4H, ***k***), 6.98 (dd, $^{3}J_{HH}$ = 3.8 Hz, $^{5}J_{HH}$ = 0.85 Hz, 2H, ***g***), 7.39 (dd, $^{3}J_{HH}$ = 3.8 Hz, $^{4}J_{HH}$ = 0.87 Hz, 2H, ***h***), 7.80 (s, 2H, ***c***), 8.24 (d, $^{3}J_{HH}$ = 7.6 Hz, 2H, ***j***), 12.16 (t, br, $^{1}J_{HN}$ = 7.6 Hz, 1H, ***m***), 17.65 (s, 1H, ***n***). ^{13}C NMR: (125 MHz, $CDCl_3$) 20.34 (***a***), 31.43 (***l***), 55.00 (***k***), 116.91 (***h***), 121.49 (***g***), 127.64 (***c***), 131.77 (***i***), 139.05 (***d***), 140.08 (***b***), 142.94 (***e***), 144.04 (***f***), 151.44 (***j***). IR (cm^{-1}): 2835 (br), 1650 (s), 1438 (m), 1290 (s), 1203 (m), 997 (m), 911 (m), 867 (m), 769 (m), 540 (w), 504 (w), 446 (w). HRMS (*m/z*): [H-M$^+$] calcd. for $C_{23}H_{23}N_6$, 383.1984; found, 383.1982.

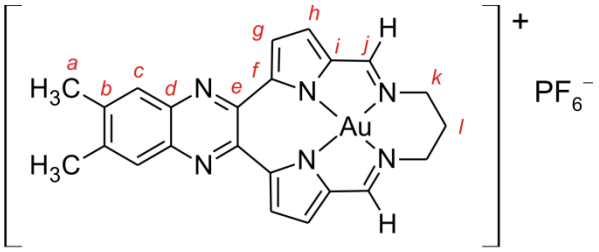

5

Compound 5: 12,14-dihydro-6,9:17,20-diepimino-[1,6]-diazacycloheptadecino-[12,13-β]-6,7-dimethylquinoxalinato}gold(III) hexafluorophosphate(V). This complex was prepared by the same method used for **1** with macrocycle **5c** as the chelating agent (105 mg, 0.275 mmols) to give a red powder of **5** (23 mg, 23%). ^{1}H NMR: (500 MHz, DMSO) 2.42 (m, br, 2H, ***l***), 2.57 (s, 6H, ***a***), 3.95 (t, $^{3}J_{HH}$ = 4.6 Hz, br, 4H, ***k***), 7.40 (d, $^{3}J_{HH}$ = 4.4 Hz, 2H, ***g***), 7.91 (s, 2H, ***c***), 7.93 (d, $^{3}J_{HH}$ = 4.4 Hz, 2H, ***h***), 8.83 (s, 2H, ***j***).^{13}C NMR: (125 MHz, DMSO) 20.59 (***a***), 34.43 (***l***), 51.85 (***k***), 119.00 (***h***), 123.15 (***g***), 127.55 (***c***), 135.58 (***e***), 139.23 (***i***), 139.40 (***d***), 143.41 (***b***), 148.62 (***f***), 163.48 (***j***). IR (cm^{-1}): 1573 (m), 1396 (w), 1335 (m), 1237 (m), 1116 (m), 830 (s), 555 (m), 423 (m). UV-vis: (CH_3CN) λ_{max} [nm] (ε/M^{-1} cm^{-1}): 248 (25 332), 316 (33 978), 350 (21 241), 378 (18 569), 457 (15 356), 484 (14 097). HRMS (*m/z*): [M^{+}] calcd. for $C_{23}H_{20}N_6Au$, 577.1415; found, 577.1425.

Compound 7: [12,13-dihydro-14H-6,9:17,20-diepimino[1,6]diazacyclo-heptadecino [12,13-β]quinoxalinato]nickel(II). The synthesis of this complex followed the literature method using macrocycle **1**, produced purple crystals of **7** after recrystallization from a binary mixture of dichloromethane and hexane, and gave bulk material with spectroscopic data in agreement with those reported in the literature.[1]

1.1.3 Plots of Selected Primary Spectral Characterization Data

Fully assigned high-field proton and carbon NMR spectra for **1**–**5** are displayed in Section 2.2.4; high-resolution mass spectra are given in Section 2.2.5.

1.2 Specialized Spectroscopy

1.2.1 Octanol/Water Partition Coefficients

Solutions of water-saturated octanol and octanol-saturated water were prepared by shaking high purity octanol (≥ 99%) with ultra-pure water (18.0 MOhm cm^{-1} resistivity). The layers were left to separate over a period of 24 hours before they were centrifuged and collected separately. These solvents were used for all further partition coefficient determinations. Although compounds **1**–**5** were soluble in octanol, they were not sufficiently soluble in pure water to permit the determination of their aqueous phase molar absorptivities (extinction coefficients) from the Beer-Lambert law. However, since the spectra of dilute aqueous solutions of the complexes matched those in pure acetonitrile, particularly around 300 nm, molar absorptivities were determined for the gold(III) chelates in pure acetonitrile in order to calculate the concentrations of the compounds from their 300 nm absorbance values in dilute aqueous solution. Beer-Lambert law plots were

determined for each complex (**1**–**5**) in acetonitrile by monitoring the absorption spectrum in a 1.0 cm path length cuvette from 200 to 800 nm with increasing concentration of the complex. The extinction coefficient at the wavelength of maximum absorbance (or wavelength of interest) was calculated using the equation $A = \varepsilon cl$, where A is the absorbance at λ_{max}, ε is the extinction coefficient ($mol^{-1}\ dm^3\ cm^{-1}$), c is the concentration ($mol\ dm^{-3}$) and l is the path length (cm). A solution of each complex in water-saturated octanol (~2×10^{-5} M; the *ratio* is independent of concentration and therefore the exact concentration is not important) was shaken with an equal volume of octanol-saturated water and allowed to settle for 1 hour before the two phases were separated. The absorption spectrum of each phase was recorded and the concentration of the gold(III) complex determined using the measured absorption and molar absorptivity at 300 nm. The octanol/water partition coefficients were then calculated using equation (1):

$$logP_{o/w} = \log\left(\frac{[Au^{III}\ complex]_{octanol}}{[Au^{III}\ complex]_{water}}\right) \quad (1)$$

All partition coefficients were calculated in duplicate and the results are a mean of the duplicated data.

1.2.2 Competitive Binding Fluorescence Studies

Aliquots of stock solutions of the gold(III) complexes **1**–**5** dissolved in DMSO were added to solutions containing 15 μM calf thymus DNA (ctDNA) base pairs and 15 μM ethidium bromide (EB) in 15% DMSO 25 mM Tris-HCl buffer (pH 7.0) at 25 °C to give final complex concentrations ranging from 0 to 200 μM. The concentration of ctDNA, per base pair (bp), was determined spectroscopically in the same buffer at 260 nm using an extinction coefficient[3] of 13 200 bp $M^{-1}\ cm^{-1}$. A solution of ctDNA in the above buffer gave an absorbance ratio ($A_{260\ nm/280\ nm}$) of 1.9:1, indicating that the DNA was sufficiently free of protein.[4] All samples were excited at 500 nm and emission was recorded between 530 and 800 nm. The apparent binding constants at 25 °C were calculated using equation (2):

$$K_{app} = \frac{K_{EB}[EB]}{[complex]} \quad (2)$$

where K_{EB} is the binding constant of ethidium bromide to ctDNA, [EB] is the molar concentration of ethidium bromide (1.50×10^{-5} M in our experiments), K_{app} is the apparent binding constant of the complex to ctDNA and [complex] is the concentration of the complex (C_{50}) that causes 50% quenching of the initial EB fluorescence, I_0, as determined from a nonlinear least-squares fit of the change in ethidium bromide emission at 614 nm, $f(x)$, with the concentration of the metal chelate, x, to equation (3):

$$f(x) = \frac{I_0 \times C_{50}}{x + C_{50}} \quad (3)$$

K_{EB} was determined *beforehand* in an independent experiment in the buffer system of choice using a standard ctDNA absorption spectroscopy titration as described below. The concentration of

ethidium bromide was fixed at 4.36 × 10^{-5} M in 15% pH 7.0 DMSO-Tris HCl buffer at 25 °C in a 1.0 cm pathlength quartz cuvette. Aliquots (5-200 μL) of a concentrated ctDNA stock solution were added and the absorption spectra recorded in the 700-200 nm spectral region after a 10 minute incubation period. Absorbance values at 492 nm were corrected for dilution and prior to fitting the optical density data to equation (4):[5]

$$(\varepsilon_a - \varepsilon_f)/(\varepsilon_b - \varepsilon_f) = \left[b - \left(b^2 - 2K_b^2 C_t[\mathrm{DNA}]/s\right)^{\frac{1}{2}}\right]/2K_b C_t \qquad (4)$$

where $b = 1 + K_b C_t + K_b[\mathrm{DNA}]/2s$ and where [DNA] is the concentration of ctDNA base pairs, ε_a is the molar absorptivity of the band at a given [DNA], ε_f is the molar absorptivity of the free ethidium bromide, ε_b is the molar absorptivity of the fully intercalated ethidium bromide, K_b is the equilibrium binding constant, C_t is the concentration of the ethidium bromide and s is the binding site size (number of nucleotides per ethidium bromide). The binding constant of ethidium bromide, K_{EB}, to ctDNA under these specific solution conditions was 4.6(1.1) × 10^6 M^{-1} (bp) (Figure S3).

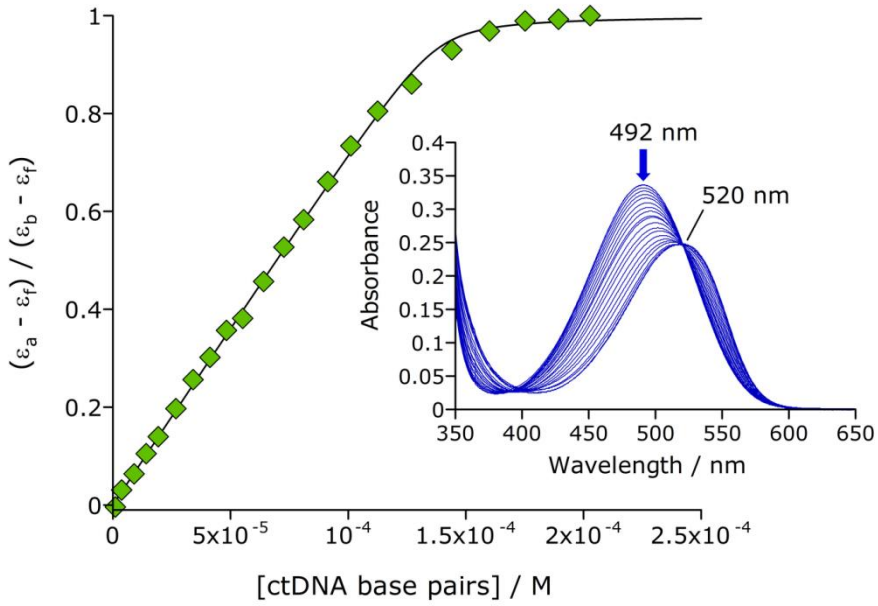

Figure S3. Determination of the binding constant, K_{EB}, of ethidium bromide (EB) to ctDNA (15% DMSO-Tris HCl buffer, pH 7.0, 25 °C). The main graph shows a nonlinear least squares fit of equation (4) to the variation of the optical density factor at 492 nm, $(\varepsilon_a - \varepsilon_f)/(\varepsilon_b - \varepsilon_f)$, with the concentration of added ctDNA. From the fit, K_{EB} = 4.6(1.1) × 10^6 M^{-1} (bp) and s = 1.6(8) (R = 0.9996). The inset shows the change in the visible absorption spectrum of ethidium bromide as a function of [ctDNA]; the absorbance at 492 nm decreases and red-shifts to 520 nm with increasing [ctDNA].

It is noteworthy that attempts to determine the binding of **1**–**5** to ctDNA directly using an absorption titration (as done for EB above) were unsuccessful due to complications arising from the slow precipitation of the compounds in the buffer system of choice. This necessitated the use of

competitive binding experiments with a sensitive, fluorescent reporter dye (intercalated EB) to measure the ctDNA affinity constants of **1**–**5**.

1.3 X-ray Crystallography

Single crystals of **1**, **2b** and **3** suitable for X-ray structure determinations were obtained by slow diffusion of diethylether into a solution of acetonitrile containing the respective salts. X-ray data for **1** and **2b** were collected with an Oxford Diffraction Xcalibur 2 Diffractometer (CCD area detector, four-circle goniometer, and Enhance Mo Kα X-ray source employing a 3kW ceramic X-ray tube). Data were acquired at an X-ray power of 2 kW (λ = 0.71703 Å) and temperatures of 173(2) K and 120(2) K for compounds **1** and **2b**, respectively. Raw intensity data were collected, indexed, and reduced using CrysAlis CCD and CrysAlis RED.[6] Both structures were solved by direct methods using SHELXS-97[7] and refined with SHELXL-97[7] operating within OLEX2.[8]

The especially small needle-shaped crystals of **3** (the crystal used for data collection had the approximate dimensions 0.017 × 0.022 × 0.120 mm^3) required data collection on a Bruker X8 Prospector instrument employing an Apex II CCD detector, three-circle goniometer, and Cu Kα radiation generated by an Incoatec IμS microsource (30 W, λ = 1.54178 Å) with a multilayer X-ray beam monochromator. The best-diffracting crystal of **3** was a 3-fold twin with approximate fractional domain ratios of 0.6:0.3:0.1. The data were thus processed taking all three domains into account for the final refinement. The best *R*-factors were obtained using the second domain plus overlapping reflections. Use of domains 1 and 2 and all overlapping reflections with any other domain gave higher *R* factors but somewhat better completeness. The structure was solved with SHELXS-97 and the final model refinements made with SHELXL-97 operating within OLEX2, using the orthorhombic space group $Pna2_1$, with $Z = 24$ for the formula unit, $C_{22}H_{18}AuN_6 \cdot F_6P \cdot C_2H_3N$ (i.e., the mono-acetonitrile solvate of the salt).

For structures **1**–**3**, all non-H atoms were refined anisotropically. H atoms were refined in calculated positions using the standard riding model of SHELXL-97. The best-fitting models of both **2b** and **3** required the use of the SHELXL restraints DELU and SIMU for all chemically-related C and N atoms within the macrocycle to allow for stable anisotropic refinement of the structural model. Selected atoms that had exceedingly poor anisotropic thermal parameters were, furthermore, constrained to have more isotropic thermal displacement parameters using the ISOR restraint of SHELXL.

The total potential solvent accessible void volume (located with a probe radius of 1.2 Å and grid of 0.2 Å) in the asymmetric unit of **2b** was 698.7 $Å^3$ and a single disordered water molecule was located 3.55 Å (O atom site) from C22B (a methyl group carbon atom) within this void. Stable anisotropic refinement of the solvent molecule was not possible, irrespective of the restraints or geometrical constraints applied, and this necessitated removal of the diffuse reflections due to the disordered solvent from the X-ray data using PLATON's SQUEEZE algorithm.[9] Given that two independent ion pairs occur in the asymmetric unit of **2b**, compound **2b** actually crystallizes as a disordered hemi-hydrate with the chemical moiety formula $C_{23}H_{20}AuN_6$, CF_3O_3S, $0.5H_2O$.

Table S1 lists the unit cell parameters and refinement details for **1**–**3**; bond distances and bond angles are available for the three structures from their CIF files. The data have been deposited with the Cambridge Crystallographic Data Centre (CCDC numbers: 928389 – 928391).

1.4 Molecular Biology & Biochemistry

1.4.1 General

Enzymes, DNA substrates and assay kits were kindly provided by TopoGEN, Inc. (Port Orange, Florida). By definition, 2 units of Top1 enzyme relaxed 100 ng of DNA in 30 minutes at 37 °C. All test compounds (polycrystalline material, > 99% purity) were dissolved in 100% DMSO prior to use and stored at –20 °C.

1.4.2 Electrophoretic Mobility Shift Assays

For these experiments, 6.3 ng μL^{-1} of negatively supercoiled pHOT1 plasmid DNA (TopoGEN, Inc.) was used as the dsDNA substrate. Reaction solutions were prepared by mixing 1.0 μL of a 188 ng μL^{-1} pHOT1 stock solution, 3.0 μL pH 7.9 1X TGS buffer (100 mM Tris-HCl, 10 mM EDTA, 1.5 M NaCl, 1 mM spermidine, 1% BSA, 50% V/V glycerol), and 25.0 μL of deionized water in 1 mL polyethylene microcentrifuge tubes. To these solutions were added 1.0 μL aliquots of standard solutions of ethidium bromide (EB, a cationic DNA intercalator control), compound **1**, compound **6** (the free base analogue of **1**), and compound **7** (the Ni^{2+} analogue of **1**) in DMSO (molecular biology-grade, Sigma) to give final control compound concentrations of 500 nM, 5.0 μM, and 50 μM for **6** and **7**. In the case of the Au^{3+} macrocycle compound **1**, aliquots of standard solutions of the compound were diluted to give two additional final concentrations such that a more narrowly-stepped range could be investigated (500 nM, 1.0 μM, 5.0 μM, 15 μM, and 50 μM). The solutions were incubated at 37 °C for 15 min before adding 6.0 μL of 6X electrophoresis loading dye (50% aqueous glycerol, 0.025% bromophenol blue) and mixing by vortex centrifugation. Aliquots from each dyed solution (5.0 μL) were loaded on a freshly-cast 1% agarose gel and electrophoresed in 1X TBE buffer (88 mM boric acid, 88 mM TRIS base, 10 mM EDTA, pH 7.8) at 50 V for 60 min. The gel was rinsed in deionized water and stained for 10 min in an aqueous 1X TBE-buffered ethidium bromide solution (0.5 μg mL^{-1}) prior to imaging with UV transillumination (302 nm) on a Syngene ChemGenius system followed by quantification and analysis with ImageJ 1.46r.[10]

1.4.3 HTS Discrimination Assay for Top1 Interfacial Poisons and Catalytic Inhibitors

We used our recently-developed high-throughput screening (HTS) method for distinguishing between interfacial poisons (IFPs) and catalytic inhibitors of Top1 to gauge whether **1**, **2a**, and **3**–**4** are catalytic inhibitors or IFPs of the enzyme. The method is described in detail elsewhere.[11] For the present work, camptothecin (CPT, an interfacial poison of Top1) and mitoxantrone (MTX, a catalytic inhibitor of Top1) were used as control compounds at concentrations of 100 nM, 1 μM, 10 μM, and 100 μM. The actions of compounds **1**, **2a**, and **3**–**4** on Top1 were analysed over the same concentration range.

1.4.4 Product-Trapping Assay for the Discrimination of Top1 Interfacial Poisons and Catalytic Inhibitors

Inhibition of Top1-catalyzed relaxation of negatively supercoiled pHOT1 plasmid DNA was studied by two methods: (1) conventional DNA unwinding assays as designed, marketed, and distributed by TopoGEN Inc. (Port Orange, FL) and (2) our new gel-based DNA-cleavage assay that discriminates between a Top1 catalytic inhibitor and a Top1 interfacial poison.[12] In a nutshell, Top1 interfacial poisons (IFPs) are identifiable by high levels of both NOC (nicked-open circular) and linear DNA reaction products in the assay while catalytic inhibitor compounds (CICs), which do not trap the intermediate covalent DNA-enzyme cleavage complexes, cause dose-dependent reduction in the yield of NOC DNA. Thus, CICs are distinguished by the *absence of linear DNA products* in this assay.

The specific procedure for our assay[12] used in this study is as follows. By definition, one unit (1 U) of Top1 relaxes 50% of 200 ng of supercoiled pHOT1 plasmid DNA in 30 min at 37 °C. Cleavage reactions were carried out in 1 mL polyethylene microcentrifuge tubes with typically 100 U μL^{-1} of Top1 (TopoGEN, Inc.) and 188 ng μL^{-1} of supercoiled pHOT1 plasmid DNA (TopoGEN, Inc.) in a master mix of 1X TGS buffer (100 mM Tris-HCl, pH 8.0, 10 mM EDTA, 1 mM spermidine, 1% bovine serum albumin (BSA), 5% glycerol, 0 mM NaCl) at a total initial volume of 29 μL. To each of these solutions was added a 1.0-μL aliquot of an appropriate standard solution of **1**, **2a**, and **3–5** dissolved in molecular biology grade DMSO (Sigma). Final test agent concentrations ranged from 500 nM to 33 μM in a final reaction volume of 30 μL. Two controls were included: (1) reactions in the presence of several concentrations (0.5–50 μM) of camptothecin (CPT, Top1 interfacial poison) and (2) reactions in the absence of drug (i.e. gold(III) macrocycle) with increasing concentrations of Top1 from 0 to 100 units (U). Reactions were prepared on ice and initiated by incubation for 30 minutes at 37 °C. Following incubation, reactions were stopped by the addition of 3.0 μL of 10% SDS and digested with proteinase K (0.5 mg mL^{-1}) for 30 minutes at 37 °C. To each solution was added 6 μL of 6X DNA electrophoresis loading dye (50% aqueous glycerol, 0.025% bromophenol blue) prior to brief vortex mixing. A 5.0-μL aliquot of each solution was pipetted into a pre-cast 1% EB-agarose gel (to give 40 ng DNA per lane) prior to electrophoresis at 50 V for 1 h in 1X TBE-EB buffer. (Both the gel and the electrophoresis buffer contained ethidium bromide, EB, at a final concentration of 0.5 mg mL^{-1}; this permits optimal resolution of DNA cleavage products.) The resulting agarose gels were de-stained and imaged as described earlier.

1.4.5 DNA Unwinding Assay with Human TOP1

Supercoiled pHOT1 as substrate. This method is essentially the standard Top1 DNA unwinding assay manufactured and distributed by TopoGEN, Inc. Briefly, reactions were carried out in 1X TGS buffer (10 mM Tris-HCl, pH 7.9, 1mM EDTA, 150mM NaCl, 5% glycerol, 0.1% BSA and 0.1 mM spermidine) containing 100 ng supercoiled pHOT1 plasmid DNA. The indicated amount of the test agent was added prior to incubating reactions at 37 °C for 30 minutes, stopping the reaction by the addition of SDS (sodium dodecylsulfate, final concentration 4%), and removal of excess protein by Proteinase K digestion (final concentration 1 mg mL^{-1}). Following phenol-chloroform extraction (25:24:1 w/v phenol:chloroform:isoamyl alcohol), 6 μL of 6X DNA electrophoresis loading dye (50% aqueous glycerol, 0.025% bromophenol blue) was added to each solution, the solution briefly

mixed by vortex agitation, and a 5 μL aliquot loaded onto a pre-cast 1% agarose gel. Electrophoresis was carried out for 1 hour at 50 V. The gel was stained for 5 min in aqueous ethidium bromide (5 μg mL^{-1}), rinsed in deionized water by soaking (5 min) and imaged as described before.

Relaxed pHOT1 as substrate. The same reaction described above was also carried out starting from relaxed pHOT1 plasmid DNA substrate. Briefly, reactions were assembled on ice with 200 ng of supercoiled pHOT1 plasmid DNA substrate and incubated with 10U of Top1 for 30 min. at 37 °C in a final volume of 29 μL containing 1X TGS buffer. After the relaxation step, *m*-AMSA (DNA intercalator control; 4'-(9-acridinylamino)methanesulfon-*m*-anisidide or amsacrine) and the test drugs were added to their specific reaction tubes (final conc. of DMSO = 0.1%) and allowed to incubate for another 30 minutes at 37 °C. To account for the DMSO in the drug solutions, a solvent control (DMSO at final conc. of 0.1%) was used. After the 30-minute incubation, all reactions were stopped with SDS (sodium dodecylsulfate, final conc. of 1%) and treated with proteinase K (final conc. of 0.5 mg mL^{-1}) for 30 min at 37 °C. Following digestion, DNA loading dye was added and the organic-soluble compounds removed by phenol-choloroform extraction using an equal volume of PCI (phenol:chloroform:isoamyl alcohol; 25:24:1 w/v), brief vortex mixing (10 s), and centrifugation for 5 min at 13,000 RPM. The upper phase (aqueous layer) was transferred to a new tube and 33 ng of DNA (per reaction) was loaded into each well of a 1% agarose gel. The gel was developed over 2 h at 25 V. The gel was stained for 5 min in aqueous ethidium bromide (5 μg mL^{-1}), rinsed in deionized water by soaking (5 min) and imaged as described before.

1.4.6 Surface Plasmon Resonance Studies

All SPR binding studies were performed with a Reichert SR7000 SPR refractometer (Reichert, Inc.: Depew, NY, USA) at a flow rate of 41 μL min^{-1} and a temperature of 37 °C unless otherwise indicated. Two sensor chips were prepared and utilized: (i) a DNA-derivatized chip with a 20-bp DNA duplex as the surface species and (ii) a protein-derivatized chip with the catalytically inactive Y723F Top1 mutant, mTop1 (TopoGEN, Inc.: Port Orange, FL, USA), as the surface species.

In the first set of experiments, DNA served as the ligand where a biotinylated 20-bp duplex DNA segment (synthesized by Dr. Bongyong Lee, post-doc to M.T.M. at the University of Central Florida) was immobilized on a NeutrAvidin Sensor Chip (part number 13206065, Reichert, Inc.) in 1X HBS buffer (10 mM HEPES, pH 7.4, 150 mM NaCl and 3 mM EDTA, 10% DMSO). The 20-bp duplex DNA sequence used on the chip is given below:

```
Biotin-5′-GCTA GGGA TAAC AGGG TAAT-3′
          3′-CGAT CCCT ATTG TCCC ATTA-5′
```

A total of 60 ng of the above DNA was flow-equilibrated over the chip in HBS buffer to saturate all binding sites on the chip. Gold(III) macrocycles (in 1X HBS buffer solution) were then flow-equilibrated over the DNA chip as analytes, each at a set concentration of 50 nM to check for binding. Gold(III) macrocycles that bound to the immobilized DNA with a significant SPR response (notably compounds **1** and **3**) were then investigated further at concentrations of 5 nM, 50 nM, 500 nM, and 5 μM to establish appropriate K_D values.

The binding of Top1 to the chip-immobilized 20-bp duplex DNA target was studied using the catalytically inactive Y723F Top1 mutant, mTop1. In this experiment, a solution comprising 150 ng of mTop1 dissolved in 100 μL of 1 X HBS buffer solution was flow-equilibrated with the chip as before for a period of 250 s to detect association of the catalytically inactive enzyme with the immobilized DNA target. After flushing the chip with buffer solution, a second solution of mTop1 (150 ng/100 μL) containing 50 nM of compound **3** was passed over the chip as before for a period of 250 s to quantify the impact of the gold(III) macrocycle on the SPR response function.

Inverse experiments (primarily as a check for the foregoing tests) were performed with Top1 affixed to an SPR sensor chip. For these experiments, the catalytically inactive Y723F Top1 mutant, mTop1, was conjugated to the SPR sensor chip (Reichert, Inc.: Depew, NY, USA) via an anti-TOP1 mouse monoclonal antibody (TopoGEN, Inc.: Port Orange, FL, USA). The sensor chip was first activated with N-hydroxysuccinimide (NHS) and 1-(3-(dimethylamino)propyl)-3-ethylcarbodimide hydrochloride (EDC) in a 1:1 ratio. NHS and EDC were prepared as 0.5 M and 0.2 M solutions, respectively, in deionized water and stored at –80 °C until the time of the experiment. NHS and EDC were mixed in a 1:1 ratio and flow-equilibrated over the chip surface. Following activation, an antibody solution containing 950 ng of Top1 antibody in sodium acetate buffer (10 mM, pH 5.4) was flow-equilibrated over the activated sensor chip. (The coupling reagents allow the antibody to cross-link to the activated chip surface through amide bond formation.) This was followed by flow-equilibrating 320 ng of mTop1 in a solution of 0.05% Tween-20 phosphate-buffered saline (10 mM PBS-T, pH 7.4) to facilitate highly specific binding of mTop1 to the surface-supported Top1 antibody. The mTop1-derivatzed chip was then used in three key experiments:

(1) A 100-μL aliquot of a 500 nM solution of compound **3** (dissolved in 10% DMSO/buffer) was injected into the 1X HBS buffer solution stream flowing over the chip surface and flow-equilibrated with the surface-bound mTop1 to determine whether or not the Au^{3+} macrocycle binds to the protein.
(2) The mTop1-derivatized sensor chip was flushed with 1X HBS buffer solution and a 100-μL aliquot of the biotin-free 20-bp DNA duplex described above (0.35 ng μL^{-1}, pH 7.4, 37 °C) flow-equilibrated with the chip as before to verify that the surface-bound mTop1 was capable of binding its DNA substrate.
(3) The mTop1-derivatized sensor chip was flushed with 1X HBS buffer and a 100-μL aliquot of a pre-equilibrated (5 min., 37 °C) 1X HBS buffer solution of DNA (0.35 ng μL^{-1}) and compound **3** (50 nM) flow-equilibrated over the chip to determine if DNA binding by the protein was inhibited in the presence of **3**.

1.4.7 High Resolution DNA Melt Studies to Detect Intercalation

All high resolution DNA melting curve studies were carried out using a Rotor-Gene 6000 real-time PCR machine with 5-plex fluorescence channels and high resolution melt application from Corbett Research. The software used to analyze the data was the Rotor-Gene 6000 series application software (version 1.7).

Compounds **1**–**3** and **6** were added post-PCR and pre-melt. PCR reactions were effected using a PCR buffer master mix (Invitrogen), appropriate primers (to amplify a 291-bp portion of the ACTN3 gene corresponding to exon 15), genomic DNA extracted from human saliva as the template, and CYBR® Green at a final concentration of 1.5 μM for amplicon detection (λ = 510 nm). The primers used were: 5'-CTGTTGCCTGTGGTAAGTGGG-3' (forward) and 5'-TGGTCACAGTATGCAGGAGGG-3' (reverse).[13-15] The primer concentrations were 200 nM each and the template DNA was approx.7 ng/μL. The total volume for each reaction was 20 μL (0.2 mM pH 8.4 TRIS-HCl, 1.5 mM $MgCl_2$). Post-PCR, the run was paused and test compounds were added. A five-fold serial dilution, in DMSO, was performed for each compound. Aliquots (1.0 μL) of each drug solution were then added to successive reaction tubes to give final concentrations spanning the range 80 nM–50 μM for the metal complexes and 212 nM–135 μM for the metal-free macrocycle (compound **6**). A no template control (NTC) and no drug control (NDC, DMSO only) were included. Melting points were determined as standard high resolution melt (HRM) runs in 0.1 °C steps from 82–88 °C with the instrument. The DNA concentration of the amplified fragment was ca. 35 ng/μL (or roughly 0.2 μM).

The HRM curves for **1**–**3** and **6** are shown as first derivative plots in Figure S57.

The authors are indebted to Dr. Greg Watson (Biochemistry, University of KwaZulu-Natal) for carrying out the PCR run and for collecting the HRM data.

1.4.8 Top2 Kinetoplast DNA Decatenation Reaction

An exploratory check of the ability of **3** to inhibit Top2 was conducted using the procedure described elsewhere in the literature.[12] The results are shown in Figure S55.

1.5 NCI-60 Cytotoxicity Screens

Compounds **1**, **2a**, and **3**–**5** underwent initial single-dose NCI-60 cytotoxicity screens (NCI, National Cancer Institute, Bethesda) at a concentration of 10^{-5} M against their panel of 60 human cancer cell lines. Compound **3** (butyl-bridged macrocycle) was sufficiently cytotoxic and proceeded further to a 5-dose NCI-60 screen spanning the concentration range 10^{-8} to 10^{-5} M, thereby allowing the determination of GI_{50}, TGI and LC_{50} values for the compound. (GI_{50}, compound concentration effecting 50% growth inhibition; TGI, compound concentration effecting 100% growth inhibition; LC_{50}, compound concentration inducing a 50% cell kill.) The compound was selected for a repeat 5-dose screen followed by further biological evaluation (hollow fiber assay). The methodology followed and more formal definitions of the foregoing cytotoxicity parameters are available on the NCI's Developmental Therapeutics Program (DTP) website.[16] The set of 60 GI_{50} values measured for **3** were compared (in negative log format) to the analogous publically available DTP data for 26 well-known anticancer drugs that have established mechanisms of action (MOAs). More specifically, the data were analyzed using KyPlot[17] with a statistical multivariate cluster analysis algorithm (group average method, Minkowski distances) to calculate a dendrogram on which the analyzed set of anticancer drugs cluster according to similarities in their GI_{50} profiles and thus mechanisms of action (MOAs).

1.6 Molecular Simulations

1.6.1 Force Field Parameterization

A set of force field parameters to simulate the structures of gold(III) macrocycles **1**–**5** (and related non-macrocyclic derivatives) was developed as an augmented parameter set for the SP4 force field of the macromolecular molecular mechanics simulation program AMMP[18] running within VEGA ZZ 3.0.0[19] as the graphical user interface. This entailed first defining an atom type scheme to describe the coordination sphere of the gold(III) macrocycles followed by iteratively changing the initial estimates of appropriate electrostatic, angle bending, torsional angle deformation, and van der Waals parameters of the force field to produce simulated structures with progressively better fits to the X-ray structures of the cations of **1**, **2b**, and **3** (nine experimental cation structures in total).

No specific bond stretching terms were employed for the Au–N bonds of the present series of macrocycles. The bonding between the metal and ligand donor atoms is thus mainly based on the van der Waals parameter for the metal ion, its electrostatic interactions with the N-donors, and all other force field terms involving the metal ion. Although this is a simplified bonding model, it is highly effective in the case of macrocyclic complexes of metal ions because the macrocycle cavity radius and conformation together determine the in-plane M–L bonding interactions. The metal ion essentially "rides" on the donor atoms within the plane of coordination group in this model. This strategy is not new and emanates from the seminal work of Busch's group published in 1974.[20]

Importantly, this type of force field bonding model for metal complexes of macrocyclic ligands permits facile modulation of the M–L bonds during structure optimization, particularly in response to external perturbations, and is certainly less restrictive than using fixed force constants and strain-free distances for the M–L bonds. Furthermore, although not pertinent to the present study, modeling the M–L bonds in asymmetric macrocycles is likely to be more accurate with this approach. We felt that these advantages were important when attempting to simulate the noncovalent binding of the present Au(III) macrocycles to dsDNA because conformational distortions might well accompany intercalation of the metal complexes (an expectation consistent with the simulation results, especially for minor groove insertion adducts).

1.6.2 Atom Type Definitions

Atom types for the modified SP4 force field are depicted graphically in Figure S4 using the structure of **3** as an example. In VEGA ZZ, the atom type editor was used to set the atom types after initial computation of the Gasteiger charges and bond types for the structure. Four distinct nitrogen atom donors were defined for the new force field: **npw**, **npx** (the two imine nitrogen atoms); **npy**, and **npz** (the two pyrrole nitrogen atoms). The new atom type **au3** for gold(III) was also included. The charge on the atom was assigned as +1.0, as this is the formal charge of the Au(III) ion within the macrocycles of interest. This partial charge assignment is in fact a good estimate as the DFT-calculated Mulliken charges on the gold(III) ions of **1**–**5** were in the range +1.1 to +1.2. Note that four unique nitrogen donor atom types are mandatory to define the structurally unique *cis* and *trans* N–Au–N angles in the coordination sphere of the square planar metal ion.

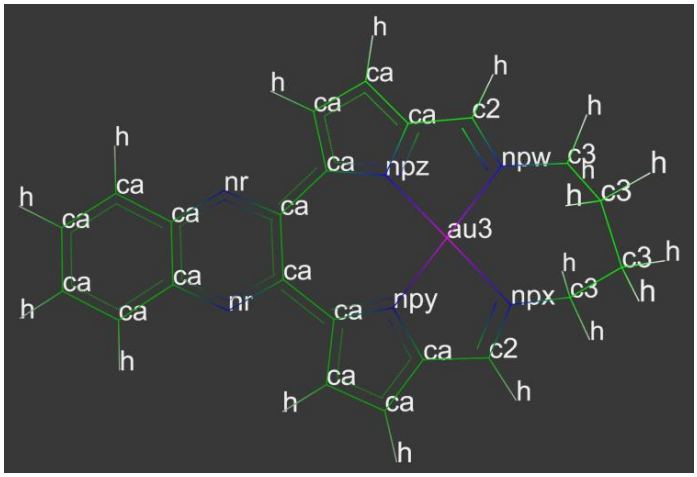

Figure S4. SP4 atom type designations for gold(III) macrocycles **1**–**5**. All atom types are standard in the force field with the exception of those for the gold(III) ion and the four nitrogen donor atoms.

Key van der Waals, bond angle deformation, electrostatic, and torsion angle deformation terms were then added to complete the augmented SP4 parameter set. The new parameters for the force field are listed in Section 1.6.3 along with their standard SP4 definitions.

1.6.3 New Parameters Added to the SP4 Force Field

```
#FF_Param SP4

; ************************************
; ****        VEGA Parameters      ****
; ****      for SP4 force field    ****
; ************************************

#Atoms

; Description:
; ~~~~~~~~~~~~
; Atom type -> Atom type
; R         -> Combining bond radius
; Theta     -> Combining angle term
; Sigma     -> VdW parameter
; Emin      -> VdW parameter
; Z         -> Effective charge
; AngleInc  -> ?
; X         -> Electronegativity
; Jaa       -> Self coulomb term
; Mass      -> Atom mass
; Charge    -> Atomic charge
; V         -> Torsion term for evaluation
; U         -> Torsion term for evaluation
; Hybrid    -> Default hybrid force (ignored if <= 0)

; Atom type  R       Theta   Sigma  Emin   Z        AngleInc  X        Jaa      Mass      Charge  V       U
Hybrid
```

```
;
=============================================================================================================================
=======
  au3        1.2800   90.00  2.912  0.013  2.43000   0.0      15.4010  30.5000   197.000   1.000   0.000  0.000
0.000
  npw        0.6400  118.00  3.660  0.069  1.71900   0.0       7.6490  11.0100   14.0067   0.000  -1.000  1.250
0.000
  npx        0.6400  118.00  3.660  0.069  1.71900   0.0       7.6490  11.0100   14.0067   0.000  -1.000  1.250
0.000
  npy        0.6380  110.00  3.660  0.069  1.90000   0.0       6.8990  11.7600   14.0067   0.000  -1.000  1.250
150.000
  npz        0.6380  110.00  3.660  0.069  1.90000   0.0       6.8990  11.7600   14.0067   0.000  -1.000  1.250
150.000


#Bonds

; Description:
; ~~~~~~~~~~~~
; Atom I,J     -> Bonded atoms
; Force        -> Force constant
; Length       -> Bond length

; Atom I  Atom J  Force  Length
; ==============================

; Bond stretching parameters for the cis and trans Au—N bonds were omitted as a simplifying
; approximation. The interaction between the metal ion and macrocycle donor atoms is based mainly
; on the van der Waals parameter for the metal ion and the electrostatic terms for Au and N
; plus other terms that involve the metal ion. This simplification was chosen to allow the
; M–L bonds to be freely adjustable during geometry optimization and essentially dictated by
; the cavity size and conformation of the macrocycle.
;
; All structures and energies in the paper are calculated with this “riding” model.

#Angles

; Description:
; ~~~~~~~~~~~~
; Atom I,J,K   -> Bonded atoms
; Force        -> Force constant
; Theta        -> Angle value

; Atom I  Atom J  Atom K  Force  Theta
; ====================================
  npw     au3     npy    600.0   180.0
  npy     au3     npw    600.0   180.0
  npx     au3     npz    600.0   180.0
  npz     au3     npx    600.0   180.0
  npw     au3     npx     10.0    90.0
  npx     au3     npy     10.0    90.0
  npy     au3     npz     20.0    90.0
  npw     au3     npz     10.0    90.0


#Torsions

; Description:
; ~~~~~~~~~~~~
; Atom I,J,K,L -> Atoms defining the torsion
; Force        -> Force constant
; N            -> Multiplicity
; Offset       -> Torsion offset
```

```
; Atom I  Atom J  Atom K  Atom L  Force  N  Offset
; ================================================
  ca      c2      npx     c3     46.0    2  180.0
  ca      c2      npw     c3     46.0    2  180.0
  c3      npx     c2      ca     46.0    2  180.0
  c3      npw     c2      ca     46.0    2  180.0
  npz     au3     npw     c2     16.0    2    0.0
  npy     au3     npz     c2     16.0    2    0.0
  npz     ca      ca      ca     16.0    2    0.0
  npy     ca      ca      ca     16.0    2    0.0
  ca      ca      ca      npy    16.0    2    0.0
  ca      ca      ca      npz    16.0    2    0.0
  npz     ca      ca      nr     56.0    2  180.0
  npy     ca      ca      nr     56.0    2  180.0
  c2      ca      ca      ca     46      2  180.0


#Hybrids

; Description:
; ~~~~~~~~~~~~
; Atom I,J,K,L -> Atoms defining the improper angle
; Force        -> Force constant
; Offset       -> Inproper offset

; Atom I  Atom J  Atom K  Atom L  Force  Offset
; ============================================
   npw     au3     npx     c3      46.0   0.0
   npx     au3     npw     c3      46.0   0.0
   c3      npx     au3     npw     46.0   0.0
   c3      npw     au3     npx     46.0   0.0


#TemplateFF SP4 1.0

; ******************************
; ****  VEGA Template V4.0  ****
; ****    Force Field SP4   ****
; ******************************


; ATDL atom description:
; ~~~~~~~~~~~~~~~~~~~~~~
; Element (2) - Bond order (1) - Ring indicator (1) - Aromatic indicator (1)
;
; The brackets indicates the length in characters of each field.

; Generic elements:                    Bond order:
; ~~~~~~~~~~~~~~~~~                    ~~~~~~~~~~~
; X = Any atom                         0   = Atom not bonded
; # = Heavy atom                       1-6 = Bond order
; $ = Any atom excluding C and H       9   = Any bond order
; @ = Halogen
; - = None

; Ring indicator:                      Aromatic indicator:
; ~~~~~~~~~~~~~~~                      ~~~~~~~~~~~~~~~~~~
; 0     = Don't check ring             0 = Don't check
; 2     = Not inside a ring            1 = Aromatic
; 3...7 = From 3 to 7 member ring
; 9     = Generic ring
```

```
; Logical operators:
; ~~~~~~~~~~~~~~~~~~
; to use the logical operators AND, OR and NOT (&, | and !), you must
; place the expression between square brackets at the specified position:
;
; Examples:
; [C- |  N-]900  -> the element can be carbon or nitrogen
; [X- & !Cl]900  -> all elements but not chlorine
; C-[4 | 3]00    -> sp3 or sp2 carbon
; C-4[9 & 9]0    -> sp3 carbon in a double condensed ring
; C-3[6 | 5][!1] -> sp2 carbon in 5 or 6 member ring not aromatic

; Atom types:
; ~~~~~~~~~~~
; each not blank and not commented line (; is the remark indicator) must
; include at least the atom type name (max. 8 characters) and the ATDL
; description. Optionally, you can specify the bonded atoms placing them
; between round brackets.


; Type    Atm    Bonded atoms
; ========================================================================
  npw       N-300 (C-300 (N-300 N-300 N-300))
  npw       N-300 (C-300 (O-100))
  npw       N-300 (C-391)
  npw       N-300 (C-300)
  npw       N-300 (O-200 O-100 O-100)
  npw       N-300 (C-900 O-100 O-100)
  npx       N-300 (C-300 (N-300 N-300 N-300))
  npx       N-300 (C-300 (O-100))
  npx       N-300 (C-391)
  npx       N-300 (C-300)
  npx       N-300 (O-200 O-100 O-100)
  npx       N-300 (C-900 O-100 O-100)
  npy       N-300 (C-300 (N-300 N-300 N-300))
  npy       N-300 (C-300 (O-100))
  npy       N-300 (C-391)
  npy       N-300 (C-300)
  npy       N-300 (O-200 O-100 O-100)
  npy       N-300 (C-900 O-100 O-100)
  npz       N-300 (C-300 (N-300 N-300 N-300))
  npz       N-300 (C-300 (O-100))
  npz       N-300 (C-391)
  npz       N-300 (C-300)
  npz       N-300 (O-200 O-100 O-100)
  npz       N-300 (C-900 O-100 O-100)
  au3       Au900
```

1.6.4 Force Field Verification

Simulation protocol. We used a three-step geometry optimization protocol with AMMP running within VEGA ZZ to obtain the lowest energy conformations of all structures. Initial structures were input using their X-ray coordinates or 3D coordinates produced with Discovery Studio Visualizer or the model builder within VEGA ZZ. The structures were then prepared for simulations in three steps (calculation of Gasteiger charges and atom types, automatic determination of the bond types, and specification of any unconventional atom types and charges) prior to execution of three optimization runs. The first run typically employed the polytope simplex optimizer of AMMP (this operates much like an iterative quenched molecular dynamics simulation) with at least 3000 minimization steps, a tolerance of 0.025 kcal mol^{-1}, and starting variance of 0.5. The resulting conformation was then optimized by the method of conjugate gradients with the same tolerance as before. The final optimization proceeded with the truncated Newton algorithm, a tolerance of 0.025 kcal mol^{-1}, and distance tolerance of 0.01 Å. A dielectric constant of 80 D was used for all calculations with a short-range nonbonded cutoff of 6.00 Å (no long-range cutoff was used).

Fit statistics. As noted above, the SP4 force field was parameterized to allow accurate calculation of the structures of **1**–**5**. The degree of similitude between the calculated and crystallographically observed (X-ray) structures (compounds **1**, **2b**, and **3**) was determined by least-squares fits of the calculated structures to the 3D X-ray coordinates of the compounds. From Figure S5, the structures and conformations of the cations of **1**, **2b**, and **3** are accurately simulated by the empirical force field. A further comparison of the structural accuracy of the force field is given in Table S2, which compares selected parameters for the X-ray, DFT-calculated, and SP4-simulated structures of the cations of **1**, **2b**, and **3**. The molecular mechanics (MM) structures exhibited bond distances and bond angles that were within 4% and 2%, respectively, of those determined experimentally, comparable to the accuracy of the DFT-simulated structures (Table S2) at the PBE1PBE/LANL2DZ level of theory.

We also checked the accuracy of the force field for macromolecular simulations using the high-resolution X-ray structure of an AT-rich 16-bp DNA duplex,[21] 5′-ACTACAATGTTGCAAT-3′, a sex-

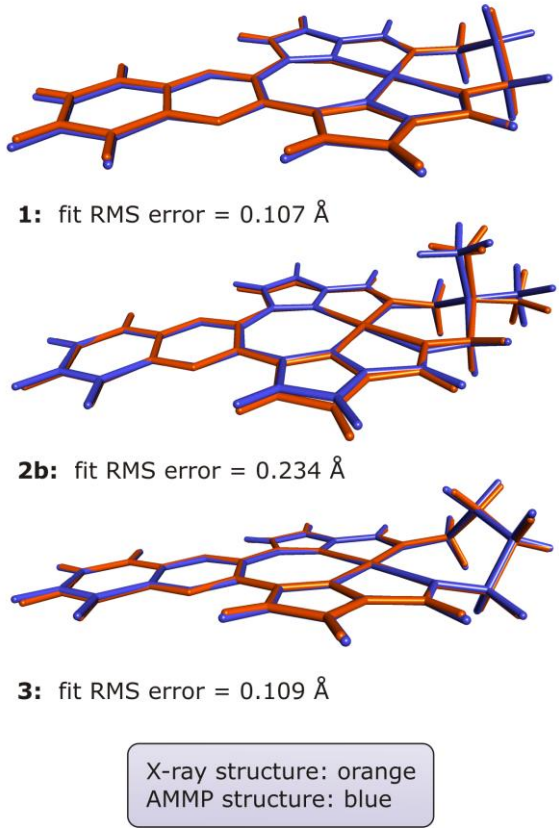

Figure S5. Non-linear least-squares fits of the AMMP/SP4-calculated and X-ray structures of cations from the experimental structures of compounds **1**, **2b**, and **3**. The fit root mean square (RMS) errors are shown and are determined from the fit of all atoms in each structure.

specific enhancer element derived from *Drosophila melanogaster*. For this simulation, the fully hydrated X-ray structure (PDB code 3BSE) was used as the input structure. All water molecules and Ca(II) ions were used for the simulation with a dielectric constant of 80 D. From the fit similarity index (0.893), the standard SP4 force field of AMMP gives an acceptable level of accuracy for macromolecular simulations in our hands, consistent with other studies in the literature.[18]

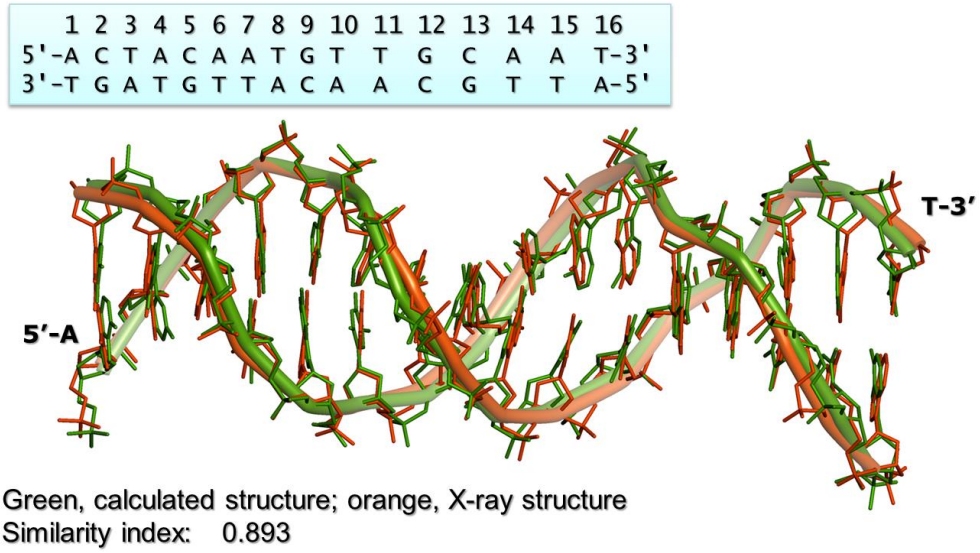

Figure S6. Comparison of the AMMP-calculated structure of a 16-bp DNA duplex with the X-ray structure (PDB code 3BSE). All hydrogen atoms, water molecules, and Ca(II) ions in the structure were included in the simulation but have been removed from the figure for clarity. The DNA sequence is shown; the fit similarity index was 0.893.

1.6.5 Macromolecular Simulations

The primary objective of these simulations was to determine the energetically preferred intercalation site (adjacent nucleotide pair) for compound **3** with a 22-bp duplex DNA target[22] favoured by Top1:

```
5'-1 2 3 4 5 6 7 8 9 10 11 12 13 14 15 16 17 18 19 20 21 22-3'
   A A A A A G A C T T  A  G  A  A  A  A  A  T  T  T  T  T
   T T T T T C T G A A  T  C  T  T  T  T  T  A  A  A  A  A
```

A conformational search was performed along the above B-form DNA duplex for all unique adjacent nucleotide pairs spanning the 5–17 index range since the four terminal nucleotides at each end of the duplex do not interact with the enzyme. We assumed that the planar aromatic quinoxaline ring system of the Au^{3+} macrocycle (as opposed to the alkyl bridge) would have the correct shape and dimensions to be the primary intercalating region capable of inserting between π-stacked DNA base pairs. Following from this assumption, there are four possible conformational types that an intercalation adduct may assume at each intercalation point along the DNA double helix since the compound may insert via the major- or minor-groove and have its bridging alkyl chain pointing in

an upstream or downstream direction. The conformational search strategy is depicted graphically below.

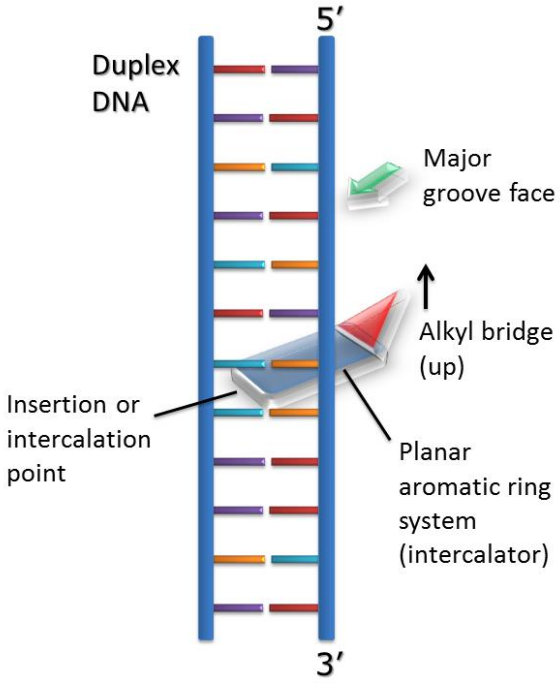

Figure S7. Illustration of the key idea behind the conformational search strategy for determining the lowest-energy noncovalent intercalation adduct between compound **3** and duplex DNA. The intercalator may insert between π-stacked base pairs from either the major-groove side (back face) or minor-groove side (front face) of the DNA duplex. Further, due to the asymmetric non-planar shape of the compound, the alkyl bridge at the non-intercalating end of the molecule may be oriented either upstream (pointing to the 5′ end) or downstream (pointing to the 3′ end) as depicted.

The same simulation protocol described earlier (Section 1.6.4) was applied to the starting structures of each of the four possible conformational types at each intercalation point along the DNA duplex. Each starting conformation was typically subject to between 3 and 15 geometry optimization runs. Single point energy determinations on the optimized structures from these runs permitted evaluation of the total and component energy terms. The process was repeated in a stepwise fashion akin to the intercalator "climbing the rungs of the ladder" until all relevant intercalation adducts had been evaluated. The conformation having **3** intercalated at a TA site, specifically T10-A11 in the above duplex DNA sequence with entry via the major groove and with the butyl bridge oriented over the molecular face pointing in a downstream direction, was the lowest in energy and assigned as the global minimum energy structure (E_{rel} = 0 kJ mol^{-1}). All other conformational energies are reported relative to the energy of the global minimum conformation. The data are summarized in Table S4 along with the free energy penalties for DNA duplex unwinding (i.e. DNA double helix stability) calculated using the program WEB-THERMODYN.[23]

Once the energetically preferred intercalation site had been determined (T10-A11 for **3**) by the above conformational search, the ternary noncovalent complex between Top1, its 22-bp DNA

duplex target substrate, and compound **3** was simulated using the same geometry optimization strategy described earlier. For these simulations, the X-ray structure of the binary noncovalent complex between the Y723F mutant form of Top1 (mTop1) and its bound 22-bp DNA duplex target (PDB code: pdb1a36[22]) was used to generate the starting structure for the simulations (all waters of crystallization included). However, the enzyme was first converted back to its wild-type form (Y723) and the DNA duplex removed prior to docking the global minimum energy structure of the binary noncovalent DNA•**3** intercalation adduct (T10-A11 intercalation site) calculated above within the enzyme's substrate-binding channel. The geometry optimization simulations of this ternary Top1•DNA•**3** noncovalent complex permitted a structure-based analysis of whether or not the enzyme could (a) recognize its target DNA base sequence[22] and (b) potentially still make a transient covalent cleavage complex via Y723-mediated hydrolysis of the phosphate ester link between T10 and A11.

1.6.6 DFT Simulations

DFT calculations were performed with Gaussian 09W (Rev. C.01 SMP)[24]. Geometry optimizations were effected *in vacuo* at the B3LYP[25]/6-311G(d,p)[26] and PBE1PBE[27]/LANL2DZ[28] levels of theory for the metal-free macrocycles and Au^{3+} complexes, respectively. The results of the calculations were analysed using GaussView version 5.09.[29] Structures were symmetrized when appropriate to their highest point group symmetry. NMR shielding tensors were calculated using the GIAO[30] method at the same level of theory used for the geometry optimizations. Frequency calculations were used on all refined geometries to determine the nature of the stationary point located; all structures were minima on the potential energy surface as evidenced by the lack of negative eigenvalues.

2. Supplementary Figures

2.1 Crystallographic Data

*2.1.1 Compound **1***

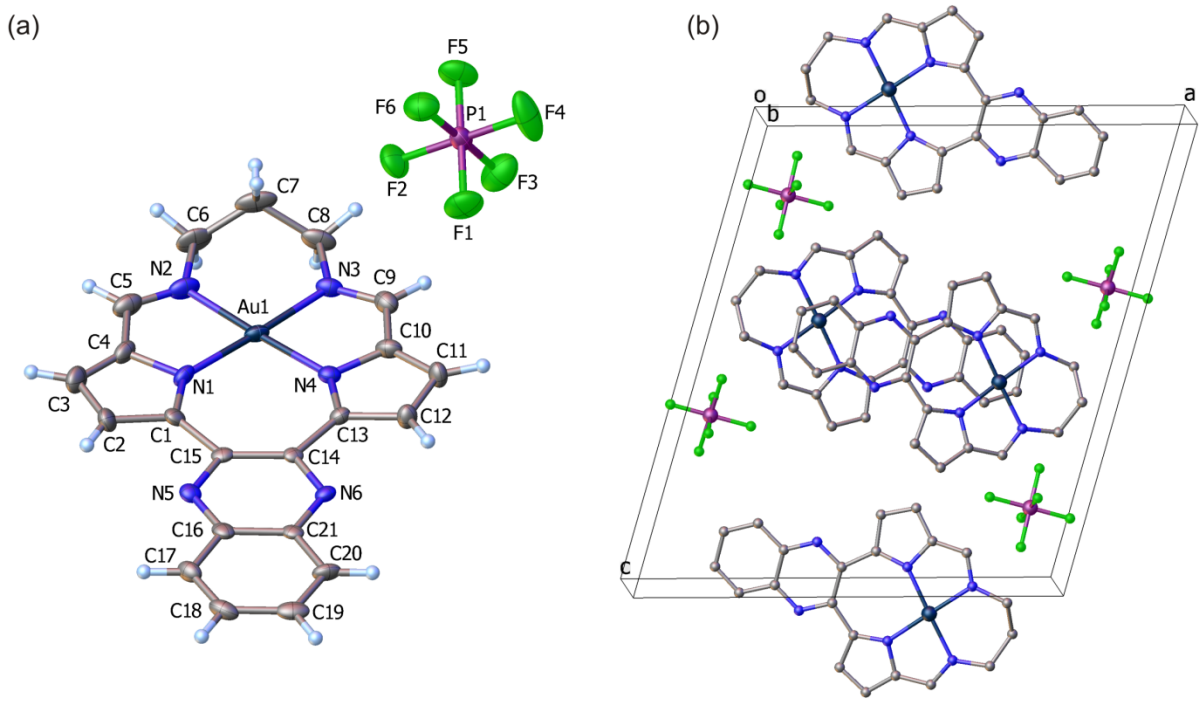

Figure S8. (a) Asymmetric unit of **1** with crystallographic labelling scheme. Thermal ellipsoids for all non-hydrogen atoms are rendered at the 50% probability level. H atoms are shown as spheres of arbitrary radius. Colour scheme: grey, C; pale blue, H; medium blue, N; dark blue, Au; purple, P; green, F. (b) Unit cell packing diagram for **1** viewed approximately down the crystallographic *b*-axis. Hydrogen atoms have been omitted for clarity and all other atoms are shown as spheres of arbitrary radii. Bonds between atoms are shown as cylinders in both diagrams.

*2.1.2 Compound **2b***

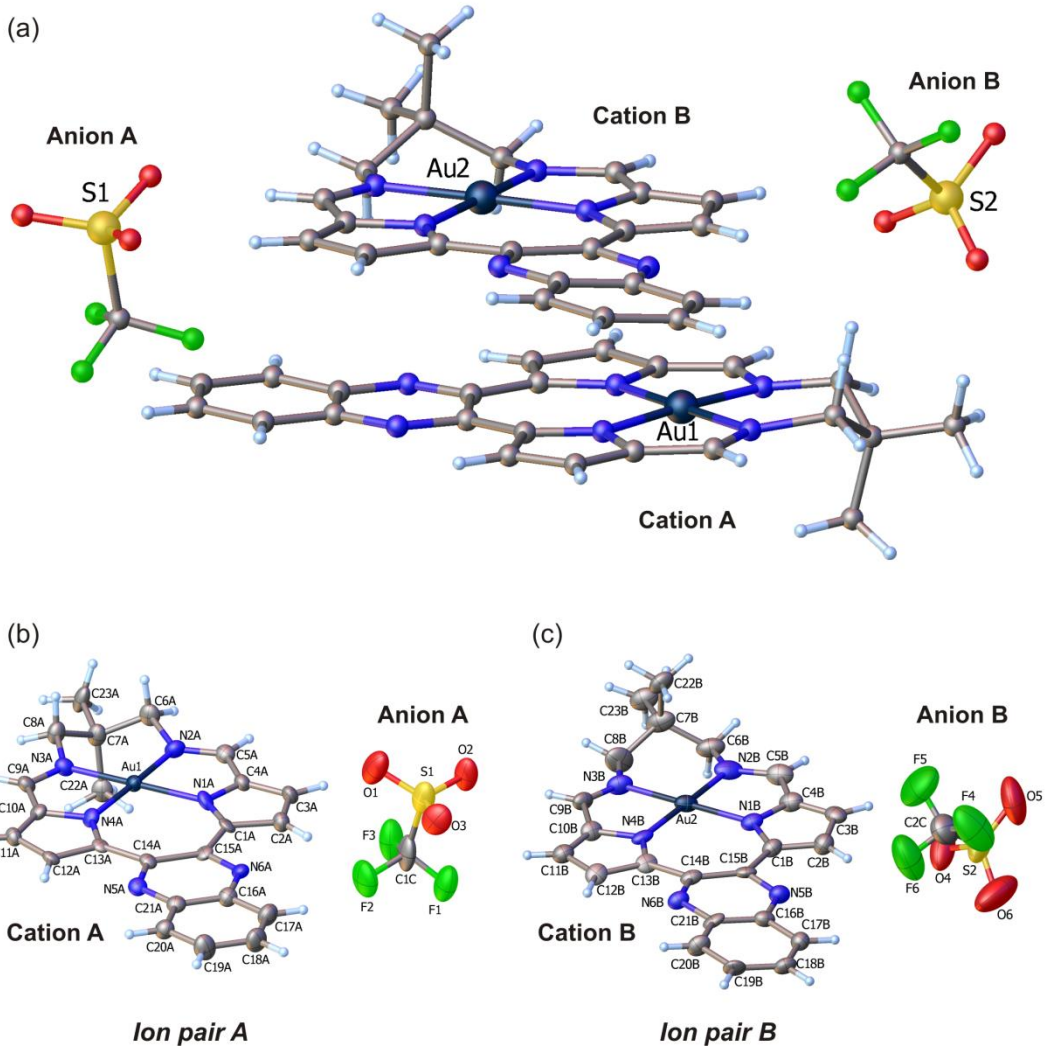

Figure S9. (a) Asymmetric unit of **2b** with partial crystallographic labelling scheme. All atoms are shown as spheres of arbitrary radius. (b) Labelled thermal ellipsoid views (35% probability surfaces) of ion pairs A and B within the asymmetric unit of **2b**. Hydrogen atoms are shown as spheres of arbitrary radii. Colour scheme: grey, C; pale blue, H; medium blue, N; dark blue, Au; yellow, S; green, F. Bonds between atoms are shown as cylinders in all diagrams.

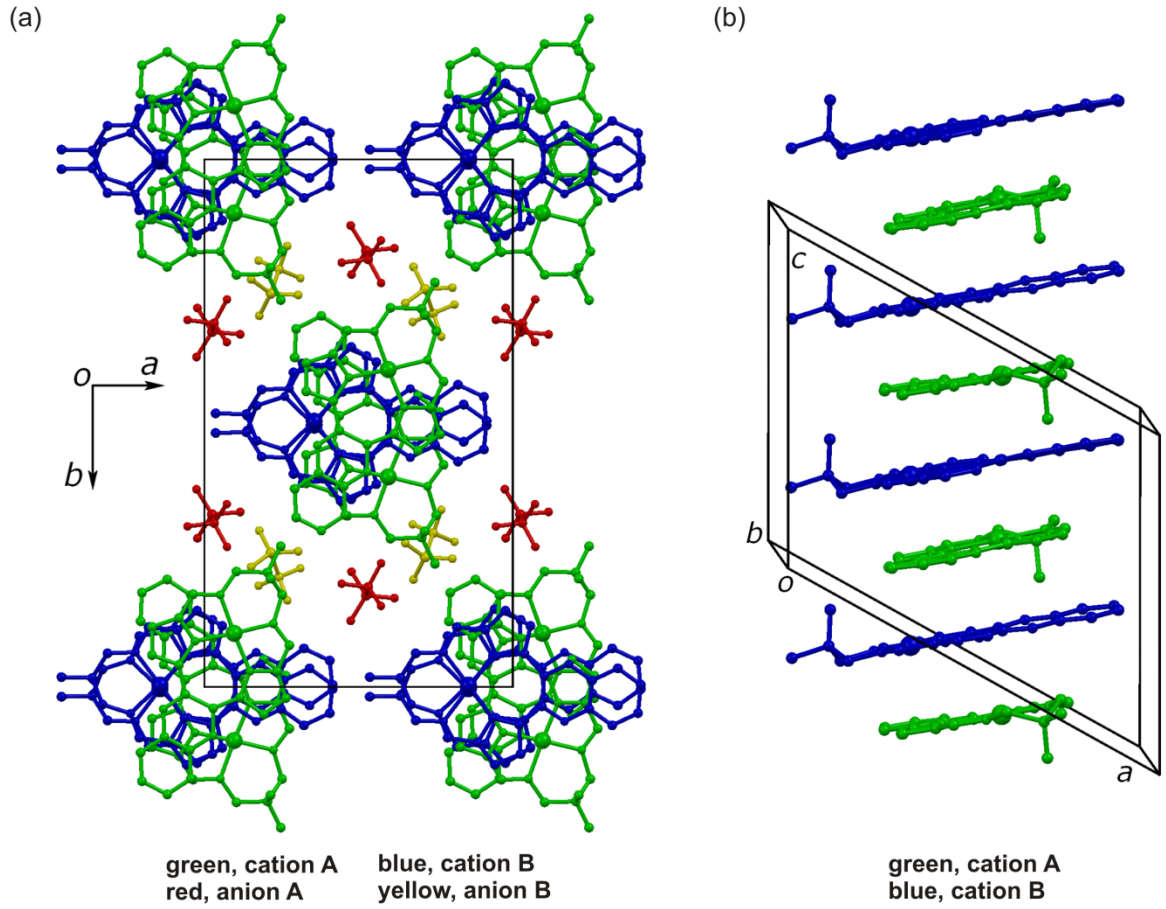

Figure S10. (a) Unit cell packing diagram for **2b** viewed down the crystallographic *c*-axis. (All atoms are rendered as spheres of arbitrary radii and H atoms have been omitted for clarity; bonds between atoms are shown as cylinders.) Cations and anions are coloured by symmetry equivalence. The cation stacks are collinear with the *c*-axis; the mean plane passing through each cation is, however, not perpendicular to the *c*-axis. (b) View of the cation stack running through the centre of the unit cell and collinear to the *c*-axis. Each cation pair (A,B) is related to the next by a glide plane along the *a*-axis direction, meaning that the cation stack does not have a uniform inter-planar spacing or cation orientation. More specifically, every third dimer has an equivalent orientation to the first dimer while every fifth cation has an equivalent orientation to the first cation.

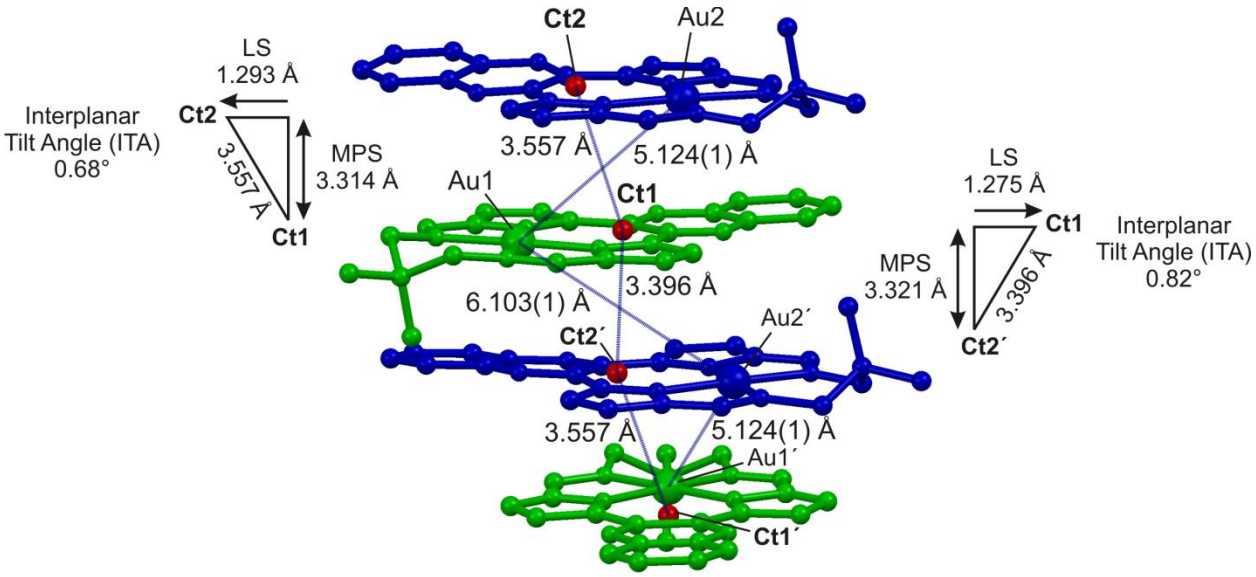

Figure S11. Illustration of the geometry and metrics of cation···cation π-stacking in **2b**. The cation 25-atom mean planes are defined by the 24 sp^2-hybridized carbon and nitrogen atoms of the macrocycle and the chelated Au^{3+} ion. The mean plane separation (MPS) assumes two values, both of which are less than the typical graphite spacing (3.35 Å) and reflect stabilization of the stack by significant π···π interactions. The 25-atom mean planes are slightly canted: the interplanar tilt angles (ITA) are less than 1°, consistent with pseudo-parallel stacking of the cation planes. The centre of gravity of each plane (**Ct**) is indicated along with distances between each centre. The lateral shift (LS) of each pair of cations, defined by the translation vector of the centre of gravity of each plane, is < 1.3 Å as indicated. The Au···Au distances alternate down the stack and take on the values 5.124(1) Å and 6.103(1) Å. (All atoms are rendered as spheres of arbitrary radii and H atoms have been omitted for clarity; bonds between atoms are shown as cylinders.)

*2.1.3 Compound **3***

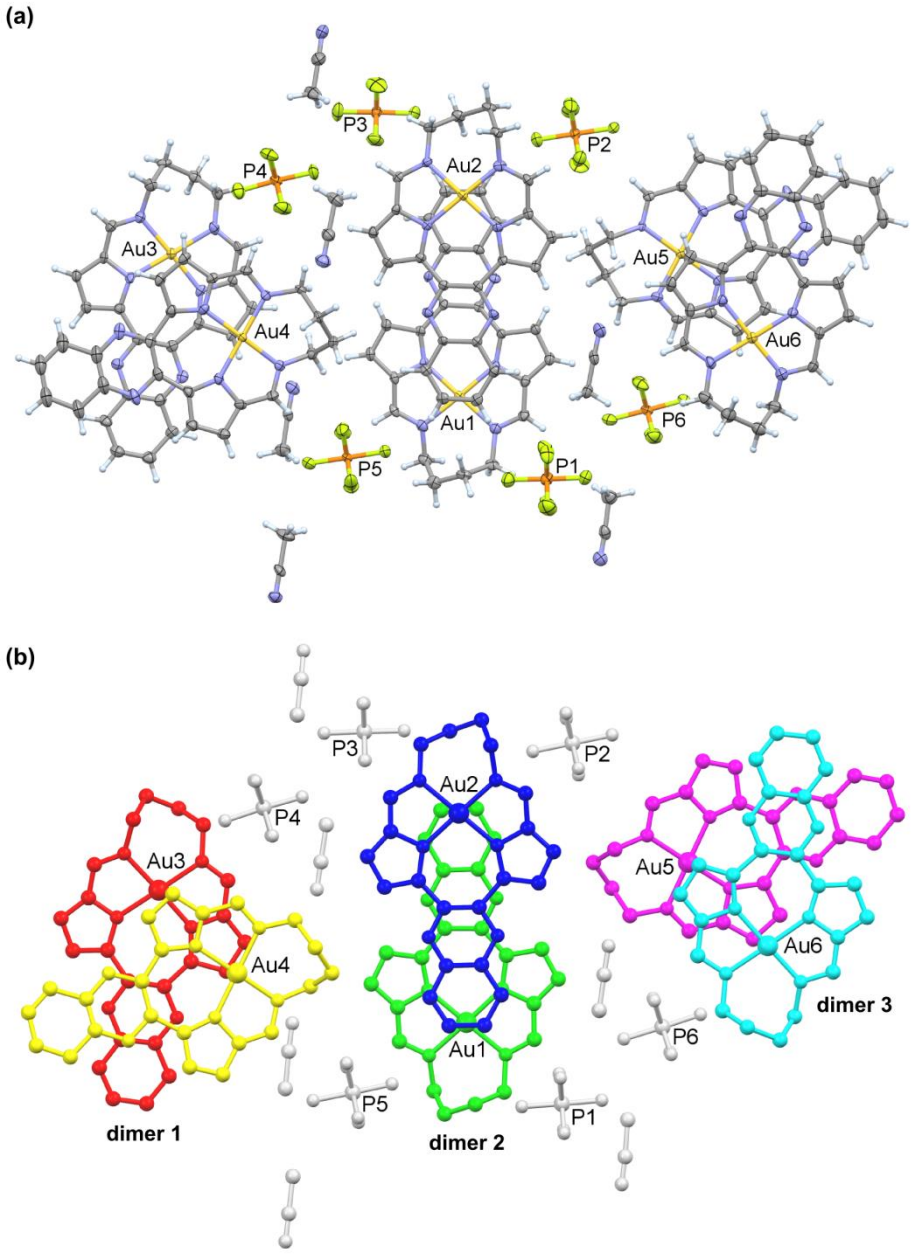

Figure S12. (a) Contents of the asymmetric unit of **3** viewed down [0,1,0]. Thermal ellipsoids are drawn at the 50% probability level; H atoms are shown as spheres of arbitrary radii. Selected atoms are labelled. The asymmetric unit comprises six independent ion pairs and six symmetry-unique acetonitrile solvent molecules. (b) View (ball and cylinder model) of the asymmetric unit of **3**. Cations are coloured according to their symmetry operators and solvent molecules and anions are uniformly shaded in grey; H atoms are omitted for clarity. The diagram clearly illustrates the propensity for π–π dimer formation between cations of **3**. Dimers 1 and 3 are best described as oblique, while dimer 2 has a head-to-tail geometry.

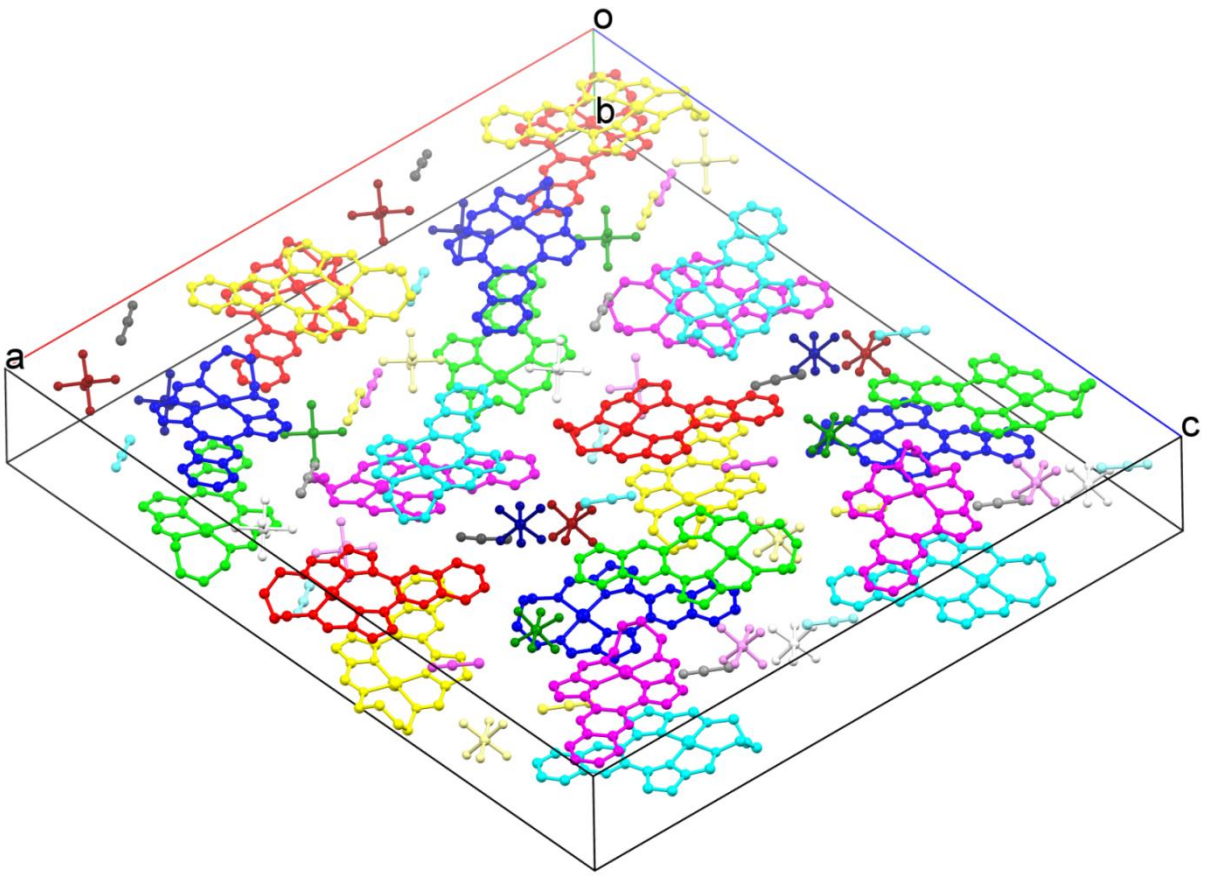

Figure S13. Unit cell contents (ball and cylinder model) for **3** coloured by symmetry operators.

*2.1.4 Overview of Cation···Cation π–π Dimers in **1–3***

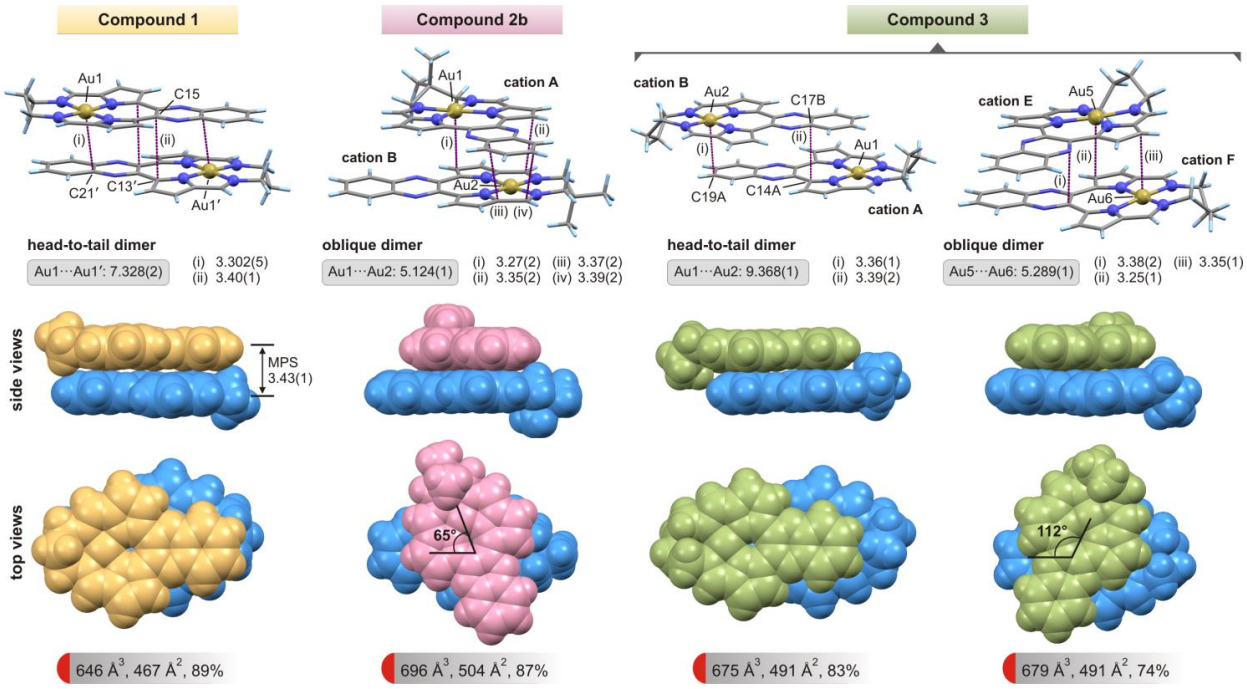

Figure S14. Views of the π–π dimers formed by cations of compounds **1–3** in the crystalline solid state. Top row, ball and cylinder structural representations; middle and bottom rows, space-filling structure diagrams (van der Waals radii) viewed perpendicular and down the axis normal to the upper cation's 25-atom mean plane. Cations of **1** (left) form symmetric head-to-tail dimers with crystallographically-imposed inversion symmetry and short intradimer nonbonded contact distances (broken lines) of 3.3–3.4 Å. The mean plane separation (MPS) between the 25-atom mean planes of the two macrocycles is indicated. Cations of **2b** (centre left) form non-centrosymmetric oblique dimers in which the uppermost cation is rotated ca. 65° clockwise about the mean plane normal relative to the line bisecting the lower cation. Cations of **3** form non-centrosymmetric head-to-tail (centre right) and oblique (right) π-π dimers (the uppermost cation of the latter is rotated by ca. 112° clockwise about the mean plane normal relative to the line bisecting the lower cation). The asymmetric unit of **3** had an additional oblique π-π dimer (cations C and D; not shown) best described as a near mirror image of the structure adopted by cations E and F. All interaction distances are given in Å (with s.u. values in parentheses). Dimer volumes, surface areas, and percentage overlaps are highlighted (bullets) in the last row of the figure.

2.2 Spectroscopy

2.2.1 Beer's Law Linearity Test

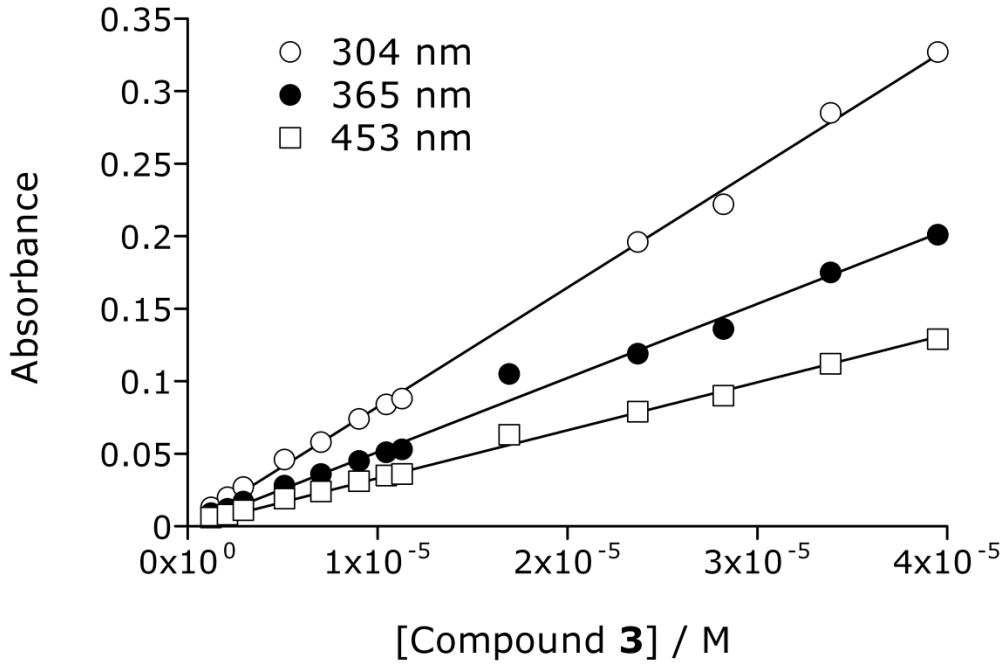

Figure S15. Plot of absorbance at several wavelengths against the molar concentration of **3** over the typical concentration range used for biological experiments. The solvent system was 5% DMSO in 95% 25 mM TRIS-HCl buffer (pH 7.0, 298 K). The linearity of the plots from 0 to 40 μM demonstrates that compound **3** does not aggregate under typical conditions appropriate for enzyme inhibition and cytotoxicity assays.

2.2.2 Solution Stability in the Presence of Glutathione

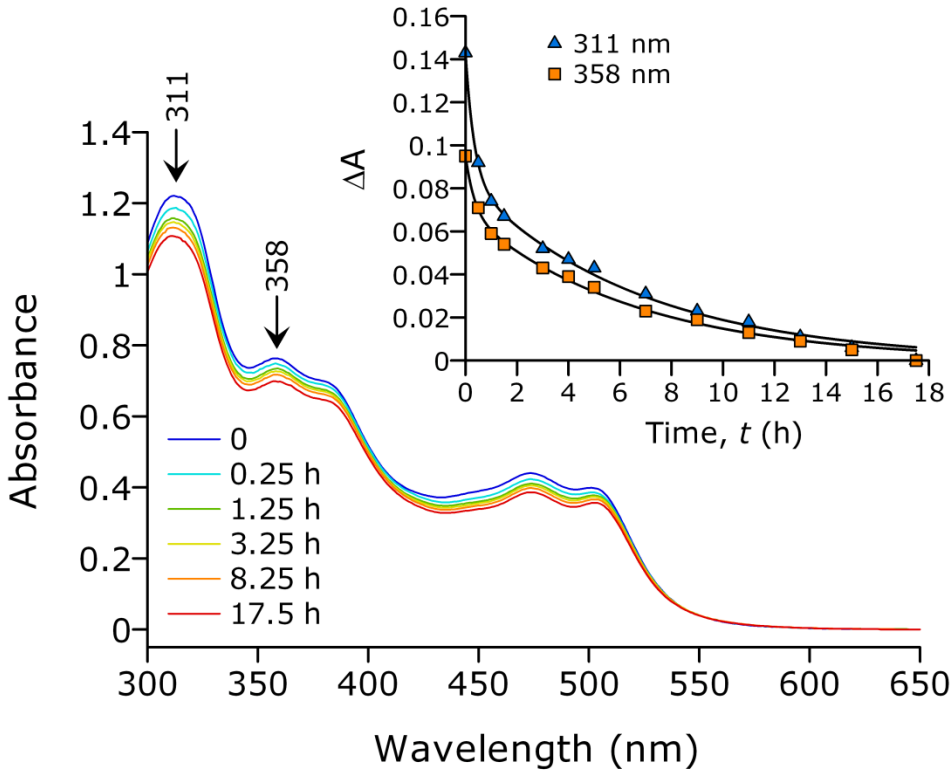

[GSH] (μM)	k_1 (h^{-1}) 311 nm	k_2 (h^{-1}) 311 nm	k_1 (h^{-1}) 358 nm	k_2 (h^{-1}) 358 nm
50.0	2.97(59)	0.149(9)	2.84(96)	0.154(9)
150.0	1.37(52)	0.160(7)	2.06(46)	0.141(5)

Figure S16. Time-dependent spectra of compound **1** (38 μM) in the presence of glutathione (GSH, 50 μM) at pH 7.0 (25 mM TRIS-HCl, 15% DMSO) and 37 °C. The inset shows the change in absorbance with time at two wavelengths in the spectrum. The data at each wavelength are fit to two consecutive exponential decay functions. The tabulated rate constants are, within experimental error, independent of [GSH]. The loss of spectral intensity without the establishment of isosbestic points and any new bands reflects slow, biphasic precipitation of the chromophore from solution. The experiment confirms that **1** (representative of the Au^{3+} macrocycles of this study) is stable to reduction by glutathione.

2.2.3 Spectral Characterization: NMR Spectroscopy

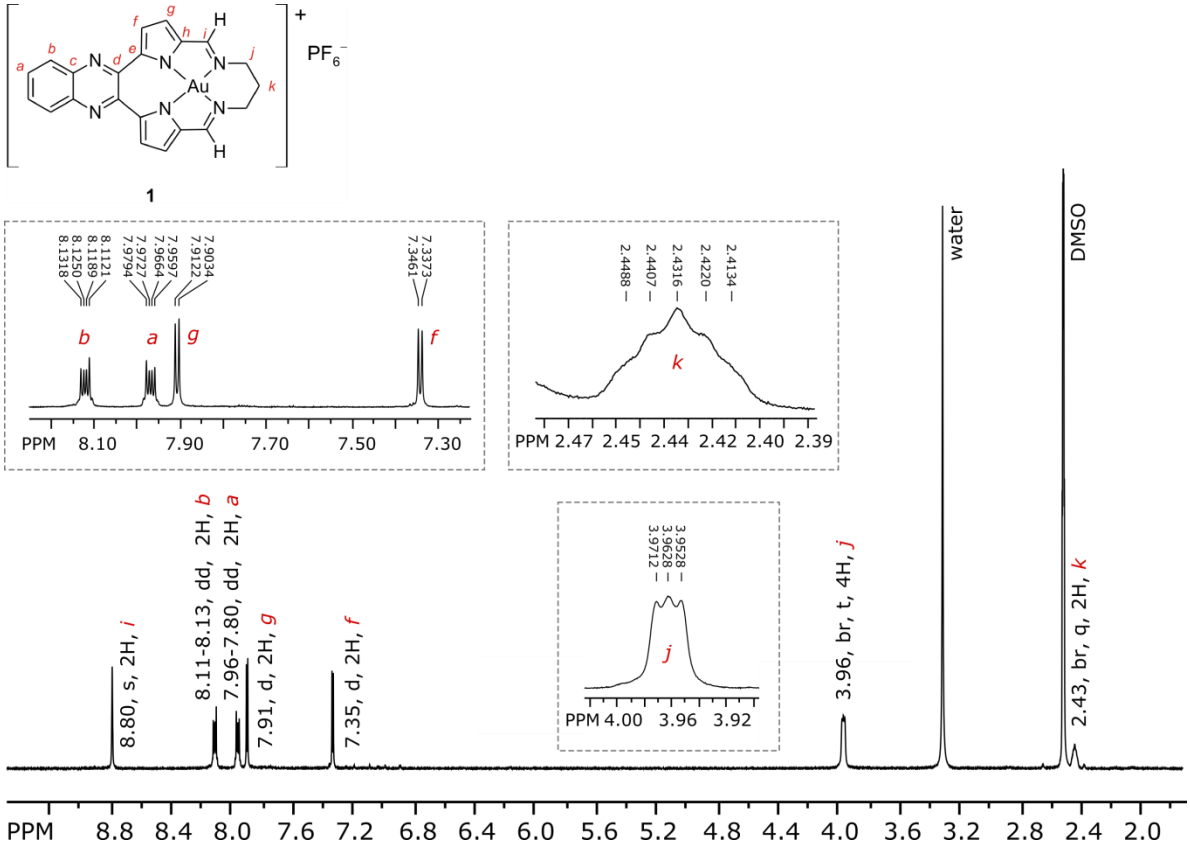

Figure S17. 500 MHz ^{1}H NMR spectrum of compound **1** recorded in DMSO-d_6 at 303 K. Insets display expansions of selected spectral regions.

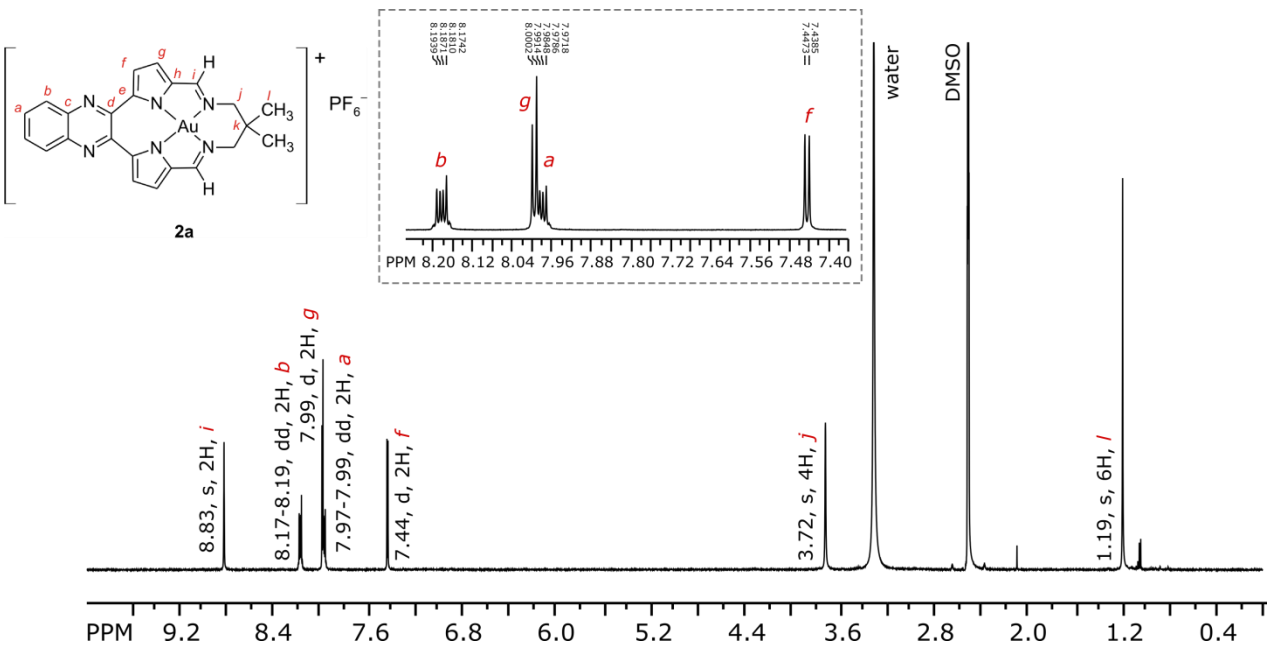

Figure S18. 500 MHz ^{1}H NMR spectrum of compound **2a** recorded in DMSO-d_6 at 303 K. The inset displays an expansion of the downfield spectral region.

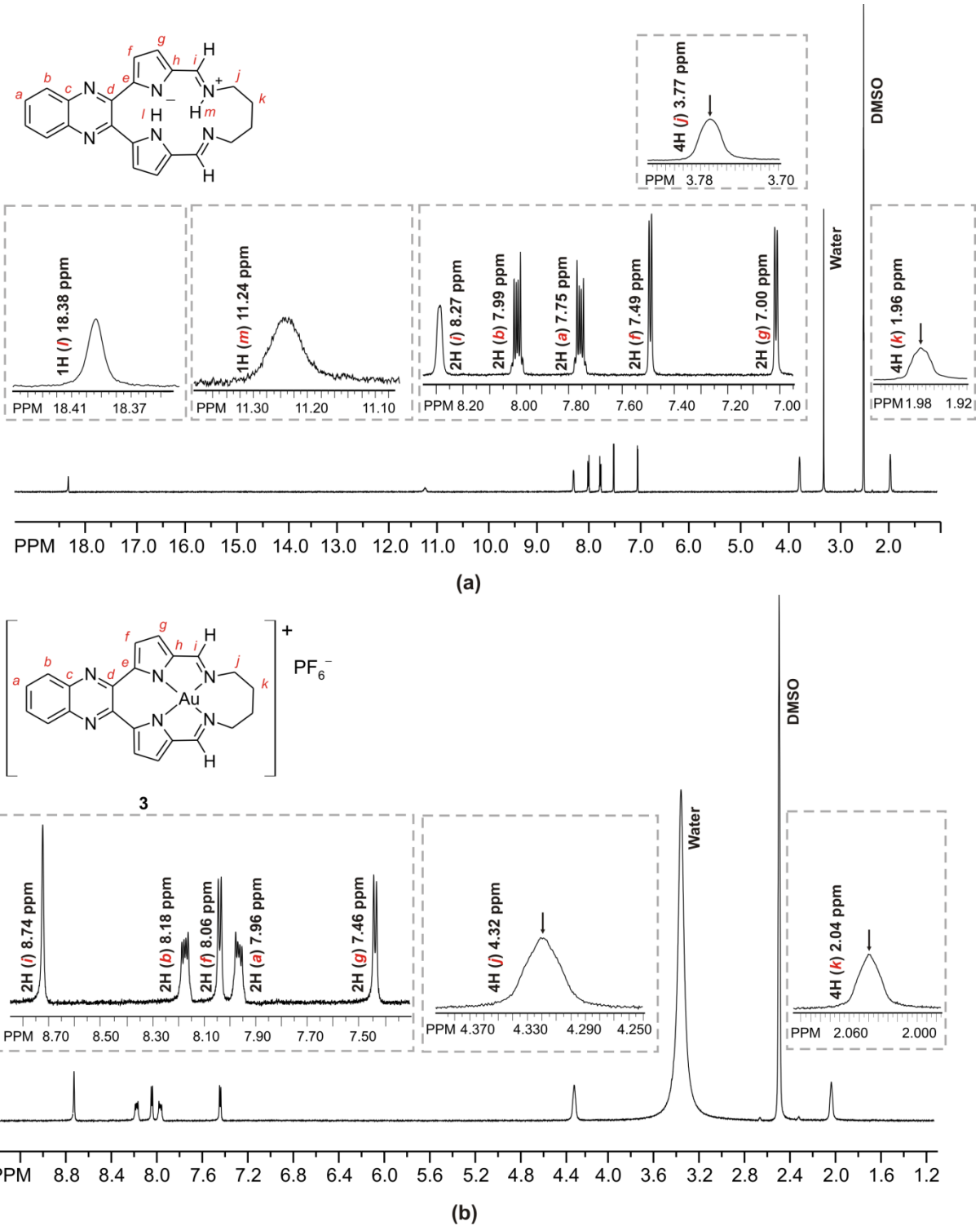

Figure S19. 500MHz ^{1}H NMR spectra of the free ligand (a) and complex **3** (b) recorded in DMSO-d_6 at 303 K. For the free ligand, chemical shift assignments for the pyrrole NH proton (*l*) and iminium NH proton (*m*) were made based on DFT-calculated shielding tensors for these nuclei.

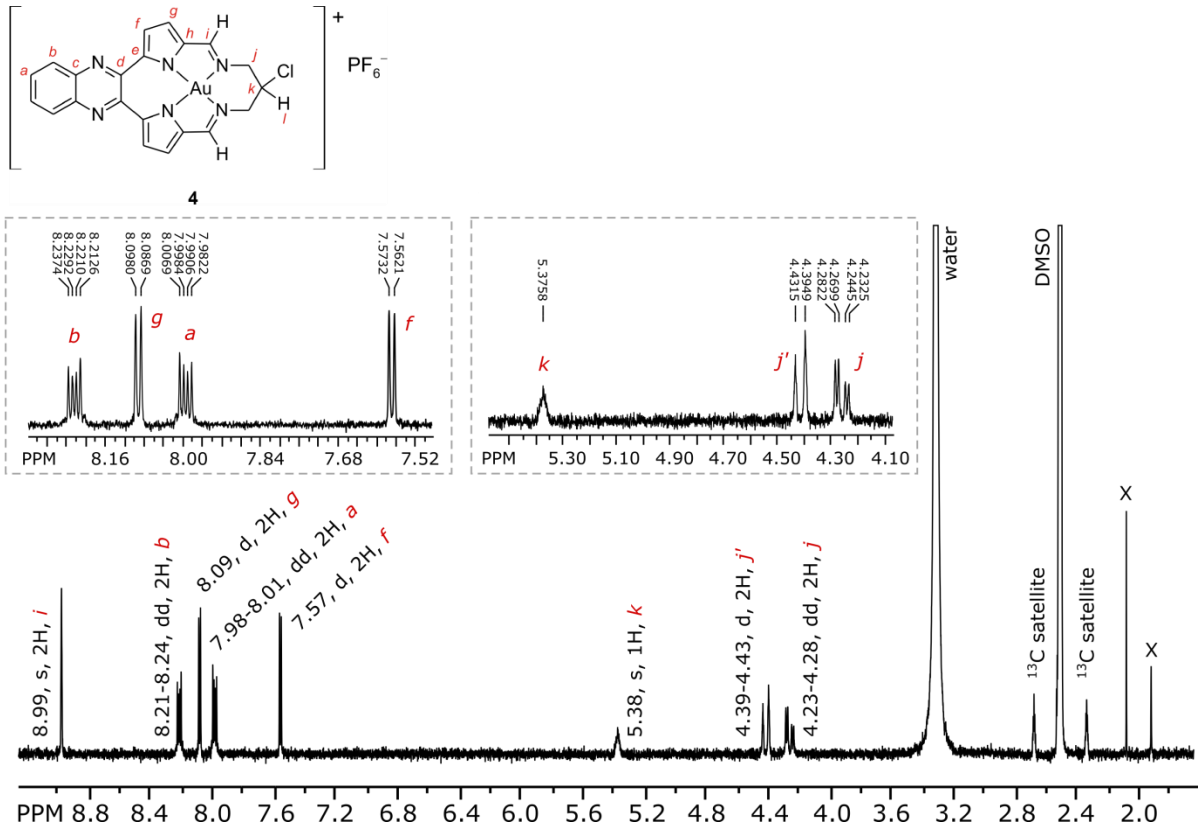

Figure S20. 400 MHz ^{1}H NMR spectrum of compound **4** recorded in DMSO-d_6 at 303 K. Insets display expansions of selected spectral regions.

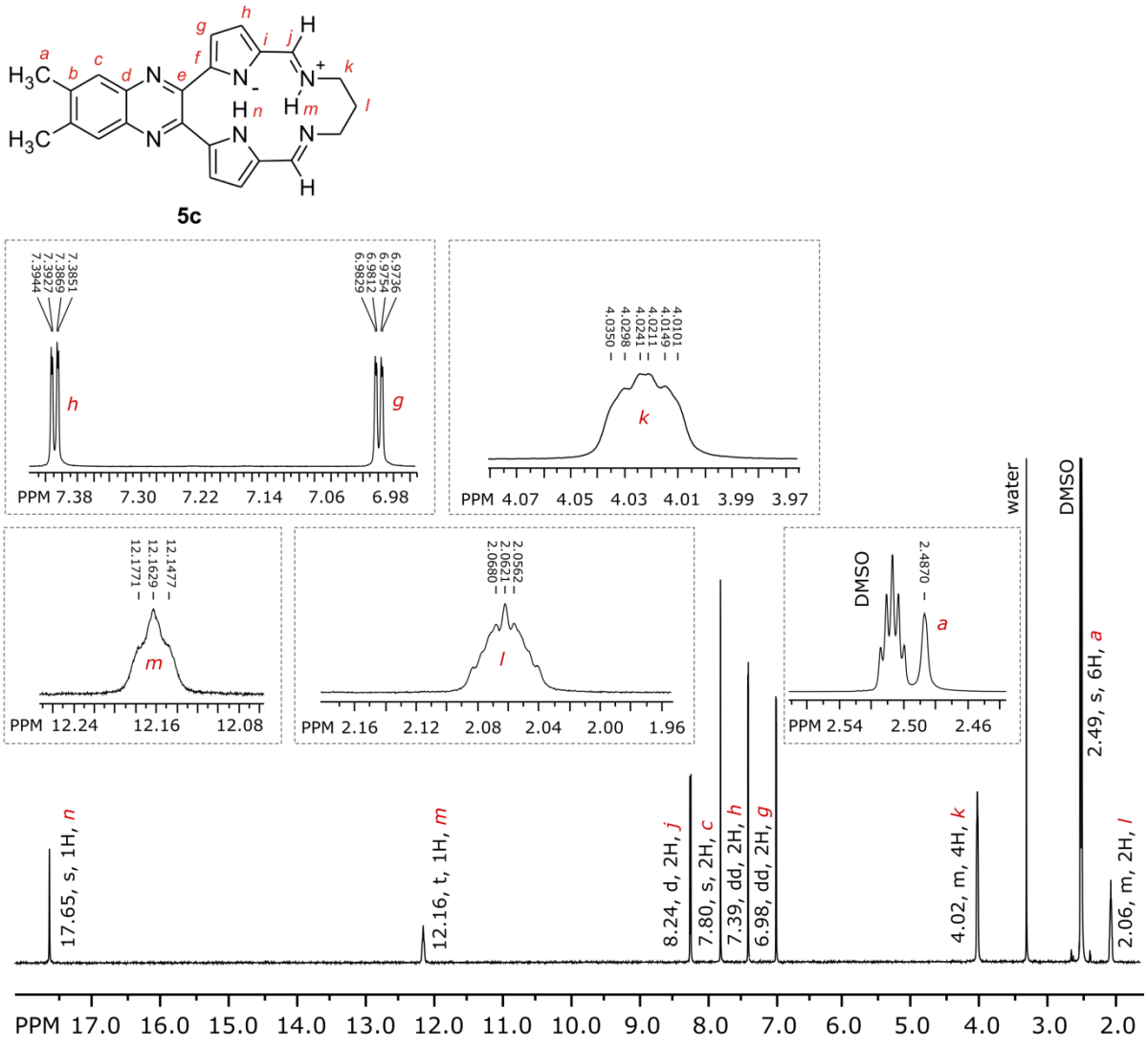

Figure S21. 500 MHz ^{1}H NMR spectrum of macrocycle (free ligand) **5c** recorded in DMSO-d_6 at 303 K. Insets display expansions of selected spectral regions.

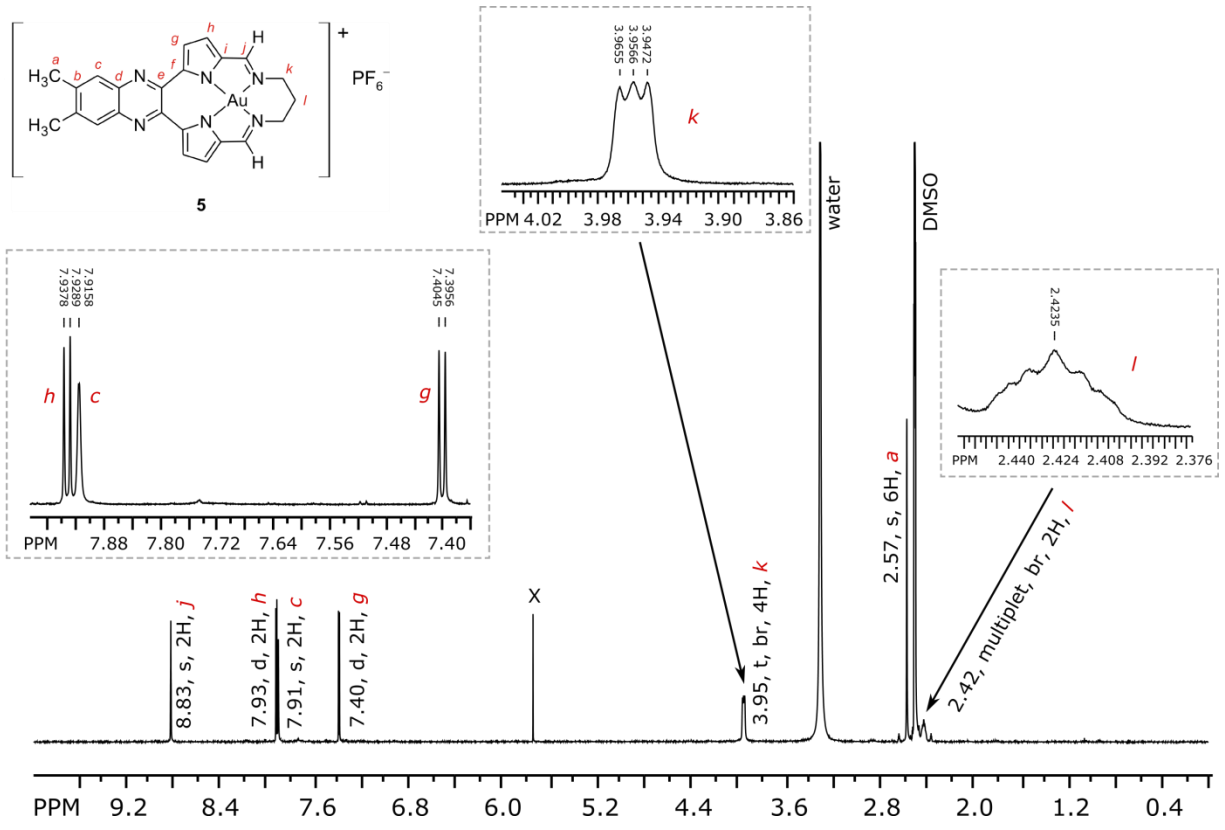

Figure S22. 500 MHz ^{1}H NMR spectrum of compound **5** recorded in DMSO-d_6 at 303 K. Insets display expansions of selected spectral regions. (X, CH_2Cl_2.)

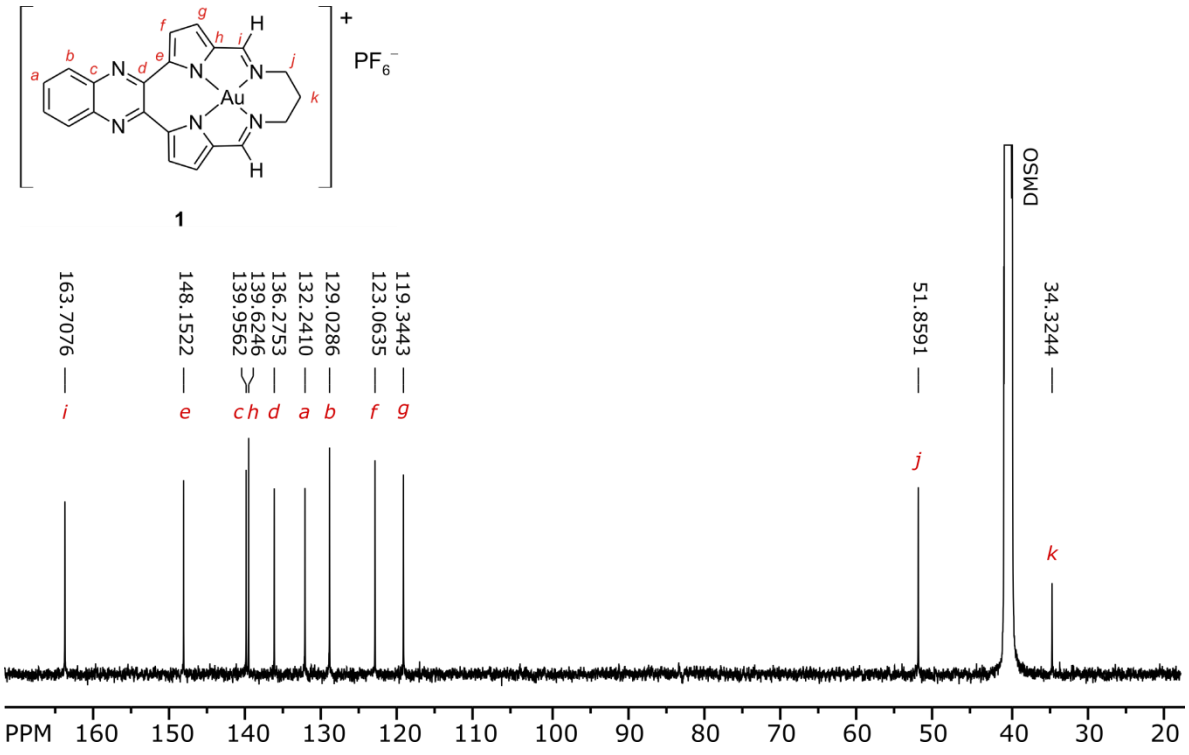

Figure S23. 125.7 MHz ^{13}C NMR spectrum of compound **1** recorded in DMSO-d_6 at 303 K.

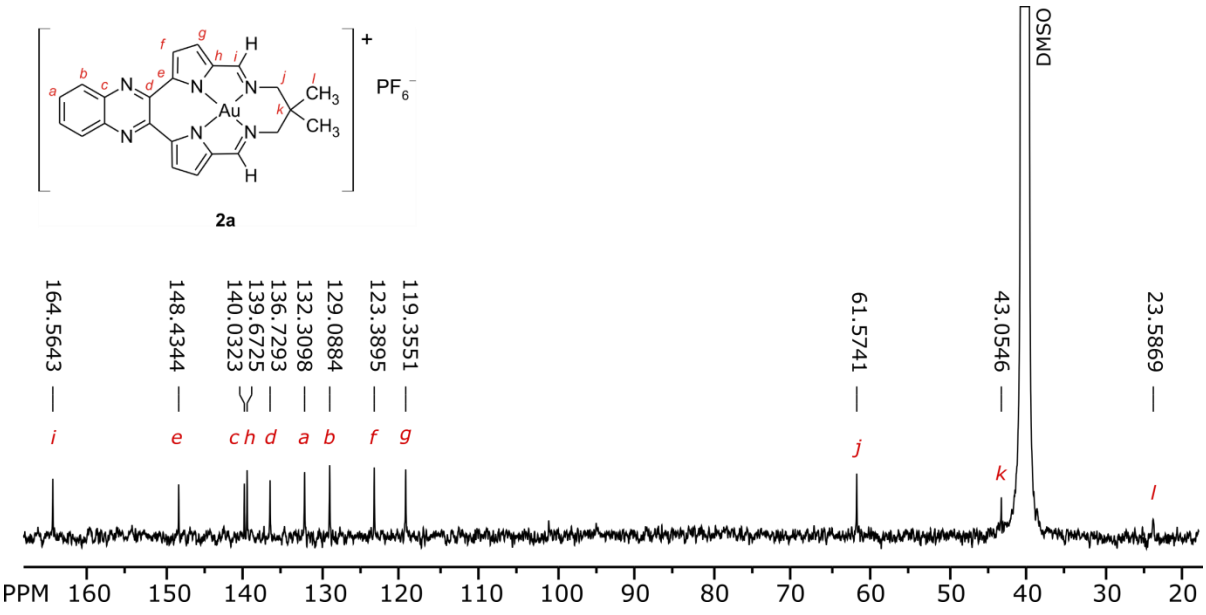

Figure S24. 125.7 MHz ^{13}C NMR spectrum of compound **2a** recorded in DMSO-d_6 at 303 K.

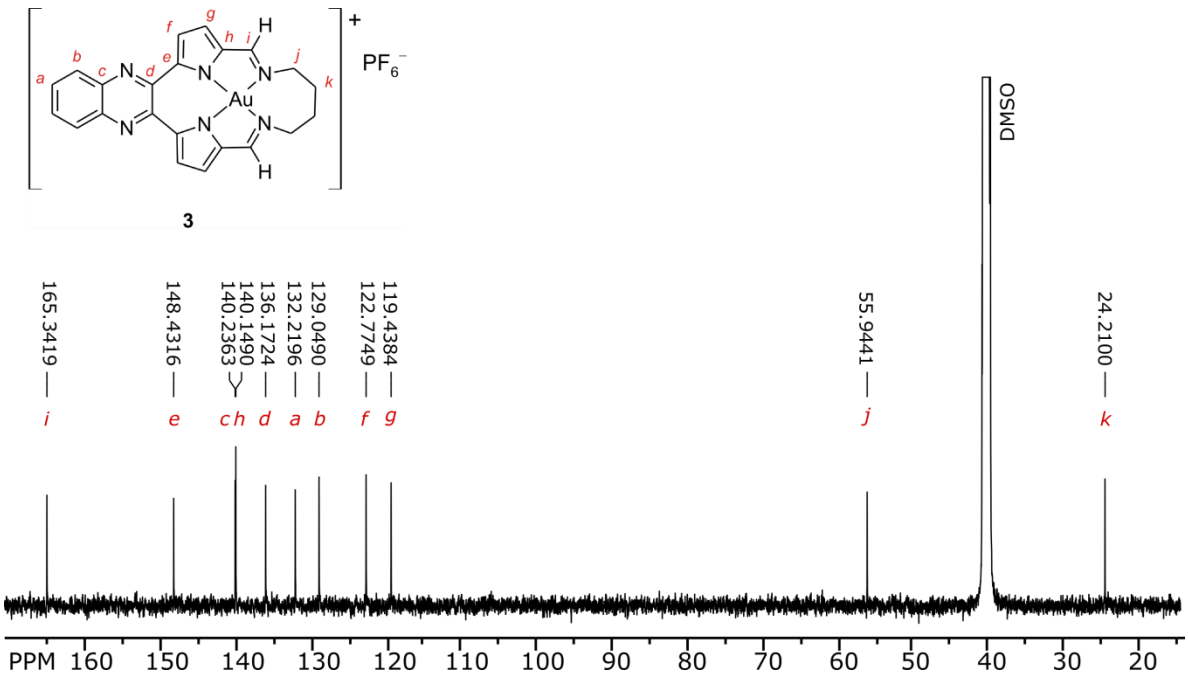

Figure S25. 125.7 MHz ^{13}C NMR spectrum of compound **3** recorded in DMSO-d_6 at 303 K.

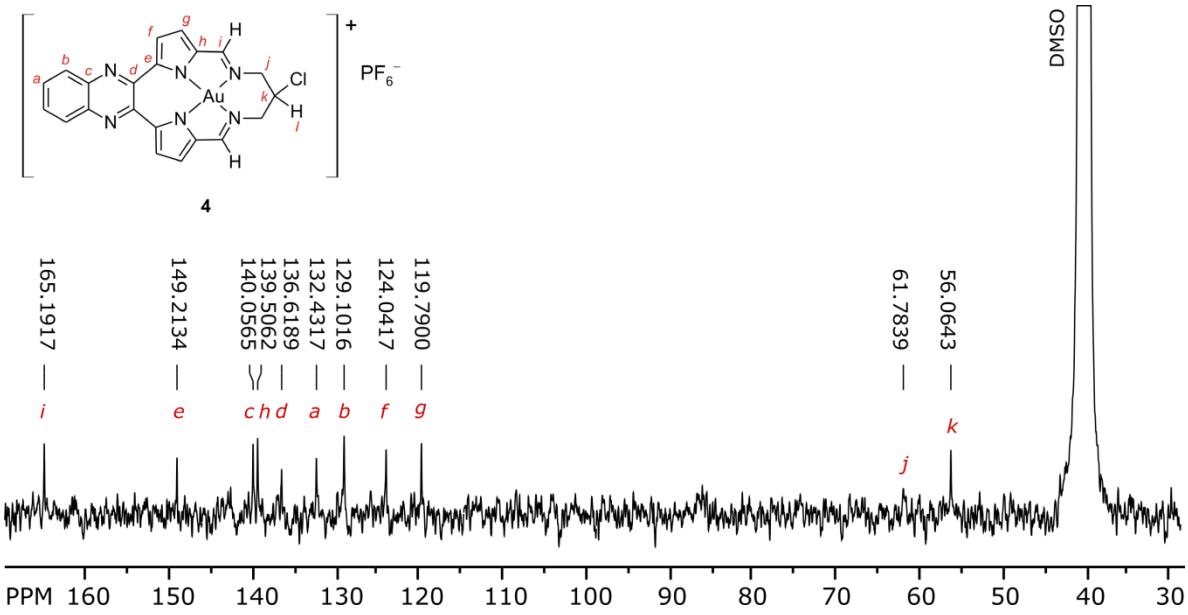

Figure S26. 100.6 MHz ^{13}C NMR spectrum of compound **4** recorded in DMSO-d_6 at 303 K.

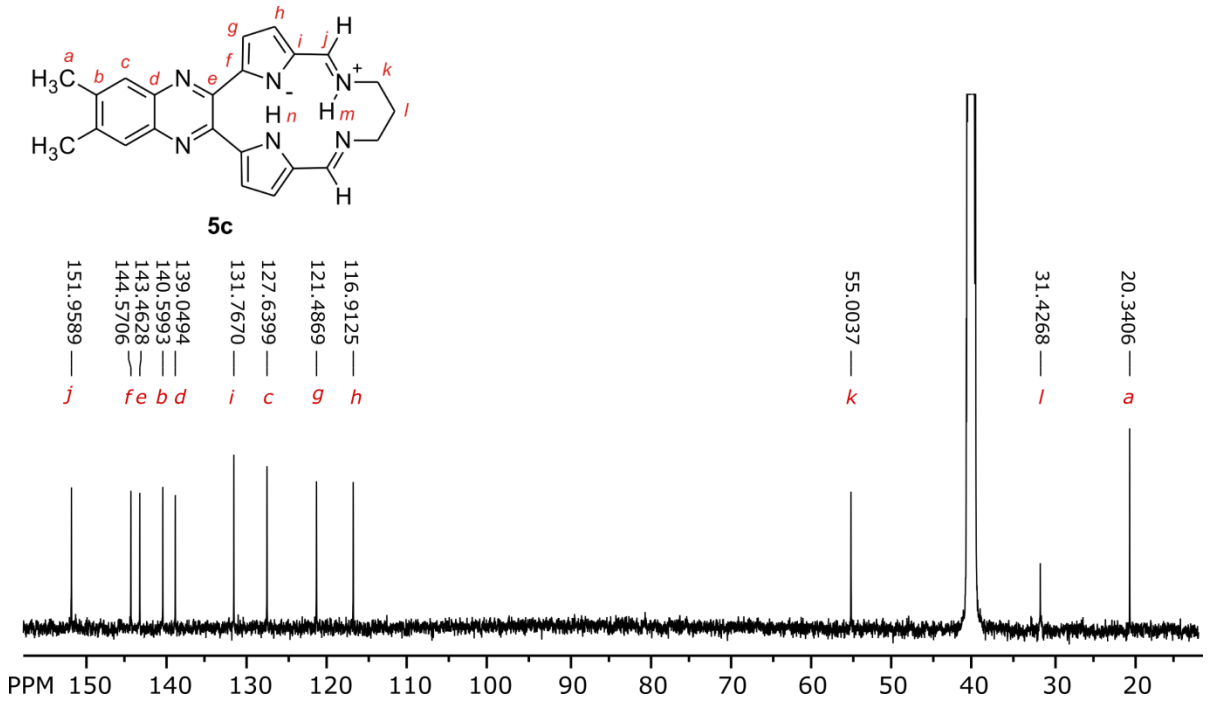

Figure S27. 125.7 MHz ^{13}C NMR spectrum of macrocycle (free ligand) **5c** recorded in DMSO-d_6 at 303 K.

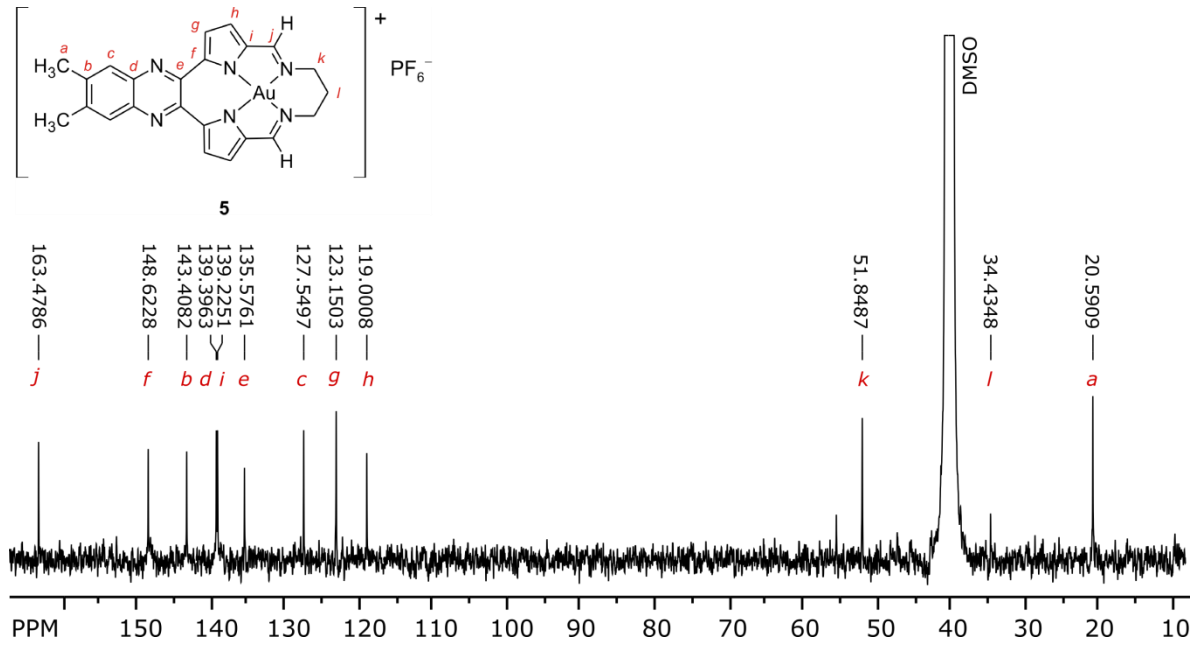

Figure S28. 125.7 MHz ^{13}C NMR spectrum of compound **5** recorded in DMSO-d_6 at 303 K.

2.2.4 Spectral Characterization: High Resolution Mass Spectrometry

Single Mass Analysis
Tolerance = 5.0 PPM / DBE: min = -1.5, max = 50.0
Element prediction: Off
Number of isotope peaks used for i-FIT = 3

Monoisotopic Mass, Even Electron Ions
10 formula(e) evaluated with 1 results within limits (all results (up to 1000) for each mass)
Elements Used:
C: 20-25 H: 15-20 N: 5-10 Au: 0-1

Kate Gillham
Au macrocycle 2 (0.017)

TOF MS ES+
1.81e+003

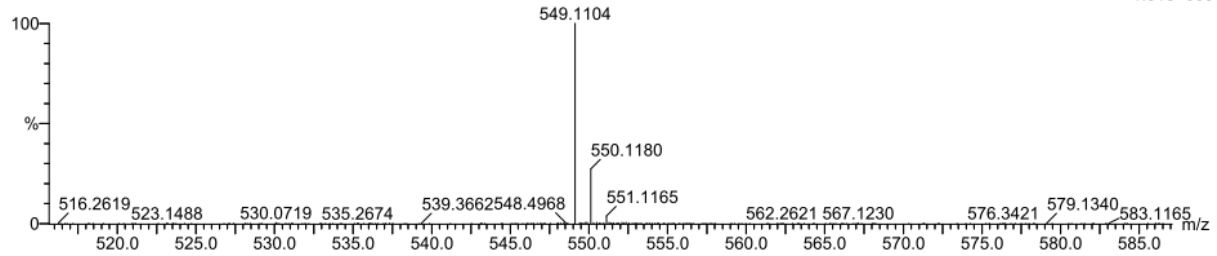

Minimum:				-1.5			
Maximum:		5.0	5.0	50.0			
Mass	Calc. Mass	mDa	PPM	DBE	i-FIT	i-FIT (Norm)	Formula
549.1104	549.1102	0.2	0.4	17.5	61.5	0.0	C21 H16 N6 Au

Figure S29. HRMS of compound **1**.

Single Mass Analysis
Tolerance = 5.0 PPM / DBE: min = -1.5, max = 50.0
Element prediction: Off
Number of isotope peaks used for i-FIT = 3

Monoisotopic Mass, Even Electron Ions
10 formula(e) evaluated with 1 results within limits (all results (up to 1000) for each mass)
Elements Used:
C: 20-25 H: 15-25 N: 5-10 Au: 0-1

Kate Gilham
aumacrodim 5 (0.069) Cm (1:5)

TOF MS ES+
3.66e+004

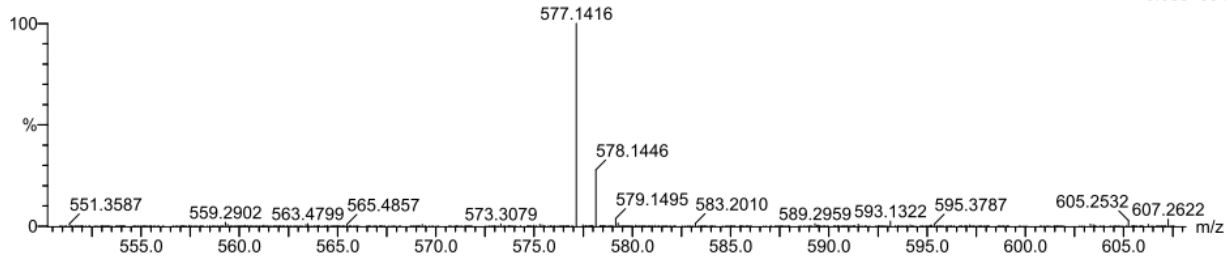

Minimum:				-1.5			
Maximum:		5.0	5.0	50.0			
Mass	Calc. Mass	mDa	PPM	DBE	i-FIT	i-FIT (Norm)	Formula
577.1416	577.1415	0.1	0.2	17.5	221.6	0.0	C23 H20 N6 Au

Figure S30. HRMS of compound **2a**.

Single Mass Analysis
Tolerance = 5.0 PPM / DBE: min = -1.5, max = 50.0
Element prediction: Off
Number of isotope peaks used for i-FIT = 3

Monoisotopic Mass, Even Electron Ions
10 formula(e) evaluated with 1 results within limits (all results (up to 1000) for each mass)
Elements Used:
C: 20-25 H: 15-20 N: 5-10 Au: 0-1

Kate Gillham
aumacrobu-pf6 2 (0.017) Cm (1:4)

TOF MS ES+
1.76e+004

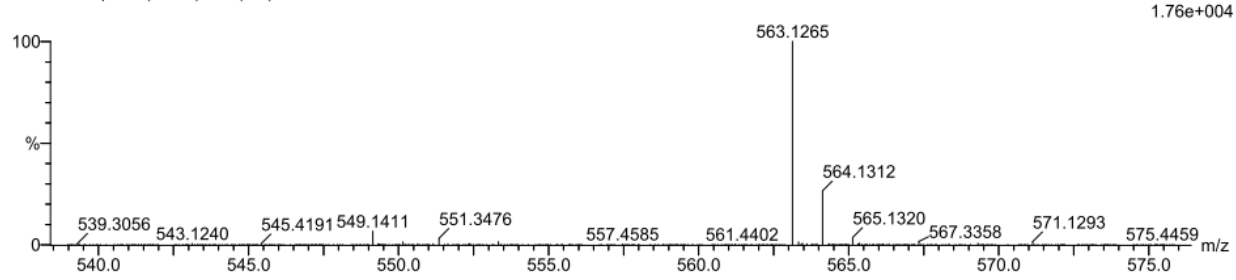

Minimum:				-1.5			
Maximum:		5.0	5.0	50.0			
Mass	Calc. Mass	mDa	PPM	DBE	i-FIT	i-FIT (Norm)	Formula
563.1265	563.1259	0.6	1.1	17.5	207.2	0.0	C22 H18 N6 Au

Figure S31. HRMS of compound **3**.

Single Mass Analysis
Tolerance = 5.0 PPM / DBE: min = -1.5, max = 50.0
Element prediction: Off
Number of isotope peaks used for i-FIT = 3

Monoisotopic Mass, Even Electron Ions
30 formula(e) evaluated with 1 results within limits (all results (up to 1000) for each mass)
Elements Used:
C: 20-25 H: 15-20 N: 0-10 Cl: 0-1 Au: 0-1

Kate Ackerman
aumacrocl 2 (0.017) Cm (1:59)

TOF MS ES+
4.04e+005

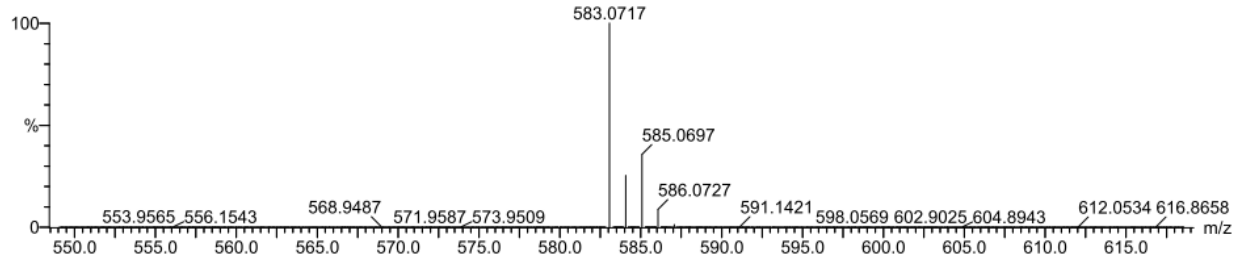

Minimum:				-1.5			
Maximum:		5.0	5.0	50.0			
Mass	Calc. Mass	mDa	PPM	DBE	i-FIT	i-FIT (Norm)	Formula
583.0717	583.0712	0.5	0.9	17.5	476.7	0.0	C21 H15 N6 Cl Au

Figure S32. HRMS of compound **4**.

Single Mass Analysis
Tolerance = 5.0 PPM / DBE: min = -1.5, max = 50.0
Element prediction: Off
Number of isotope peaks used for i-FIT = 3

Monoisotopic Mass, Even Electron Ions
4 formula(e) evaluated with 1 results within limits (all results (up to 1000) for each mass)
Elements Used:
C: 20-25 H: 20-25 N: 0-10

Kate Ackerman
dmmacropr 31 (0.512)

TOF MS ES+
6.28e+003

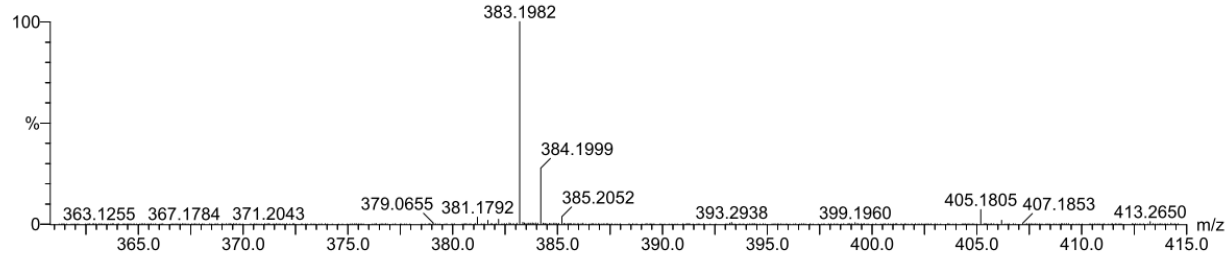

Minimum:				-1.5			
Maximum:		5.0	5.0	50.0			
Mass	Calc. Mass	mDa	PPM	DBE	i-FIT	i-FIT (Norm)	Formula
383.1982	383.1984	-0.2	-0.5	15.5	157.4	0.0	C23 H23 N6

Figure S33. HRMS of free base macrocycle **5c**.

Single Mass Analysis
Tolerance = 50.0 PPM / DBE: min = -1.5, max = 50.0
Element prediction: Off
Number of isotope peaks used for i-FIT = 3

Monoisotopic Mass, Even Electron Ions
8 formula(e) evaluated with 1 results within limits (all results (up to 1000) for each mass)
Elements Used:
C: 20-25 H: 20-25 N: 5-10 Au: 0-1

Kate Ackerman
audmmacropr 6 (0.086)

TOF MS ES+
3.32e+004

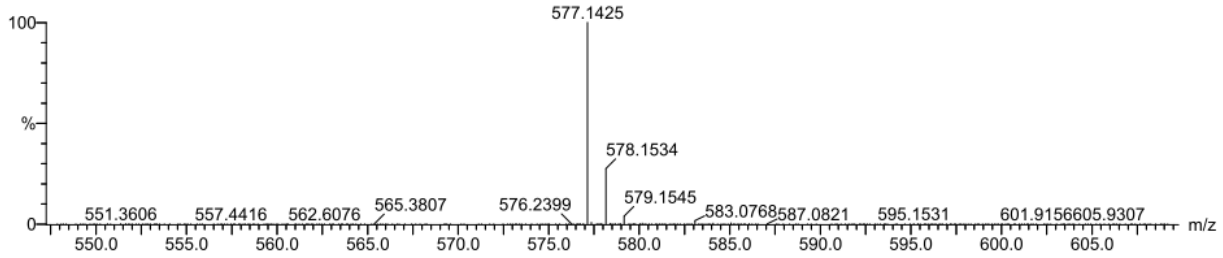

Minimum:				-1.5			
Maximum:		5.0	50.0	50.0			
Mass	Calc. Mass	mDa	PPM	DBE	i-FIT	i-FIT (Norm)	Formula
577.1425	577.1415	1.0	1.7	17.5	107.1	0.0	C23 H20 N6 Au

Figure S34. HRMS of compound **5**.

2.3 NCI Cytotoxicity Data

*2.3.1 Single-Dose NCI-60 Data for Compounds **1–5***

Developmental Therapeutics Program
One Dose Mean Graph

NSC: D-754844 / 1 | **Conc:** 1.00E-5 Molar | **Test Date:** Nov 15, 2010
Experiment ID: 1011OS53 | **Report Date:** Dec 22, 2010

Panel/Cell Line	Growth Percent
Leukemia	
CCRF-CEM	86.98
HL-60(TB)	105.50
K-562	74.10
MOLT-4	93.26
RPMI-8226	77.51
SR	91.90
Non-Small Cell Lung Cancer	
A549/ATCC	40.56
EKVX	52.25
HOP-62	52.77
NCI-H226	76.24
NCI-H23	83.41
NCI-H322M	95.28
NCI-H460	84.34
NCI-H522	48.82
Colon Cancer	
COLO 205	97.45
HCC-2998	113.11
HCT-116	89.32
HCT-15	104.35
HT29	100.05
KM12	100.64
SW-620	92.77
CNS Cancer	
SF-268	47.63
SF-295	27.44
SF-539	74.28
SNB-19	30.68
SNB-75	42.60
U251	15.37
Melanoma	
LOX IMVI	88.58
MALME-3M	76.94
M14	74.25
MDA-MB-435	103.39
SK-MEL-2	80.87
SK-MEL-28	91.02
SK-MEL-5	46.11
UACC-257	88.98
UACC-62	76.02
Ovarian Cancer	
IGROV1	78.78
OVCAR-3	109.55
OVCAR-4	84.90
OVCAR-5	122.23
OVCAR-8	57.00
SK-OV-3	99.85
Renal Cancer	
786-0	62.87
A498	54.83
ACHN	96.48
CAKI-1	86.87
RXF 393	97.43
SN12C	21.60
TK-10	106.88
UO-31	84.82
Prostate Cancer	
PC-3	76.83
DU-145	93.34
Breast Cancer	
MCF7	59.05
MDA-MB-231/ATCC	97.36
HS 578T	42.19
BT-549	78.98
T-47D	80.05
MDA-MB-468	30.70
Mean	76.68
Delta	61.31
Range	106.86

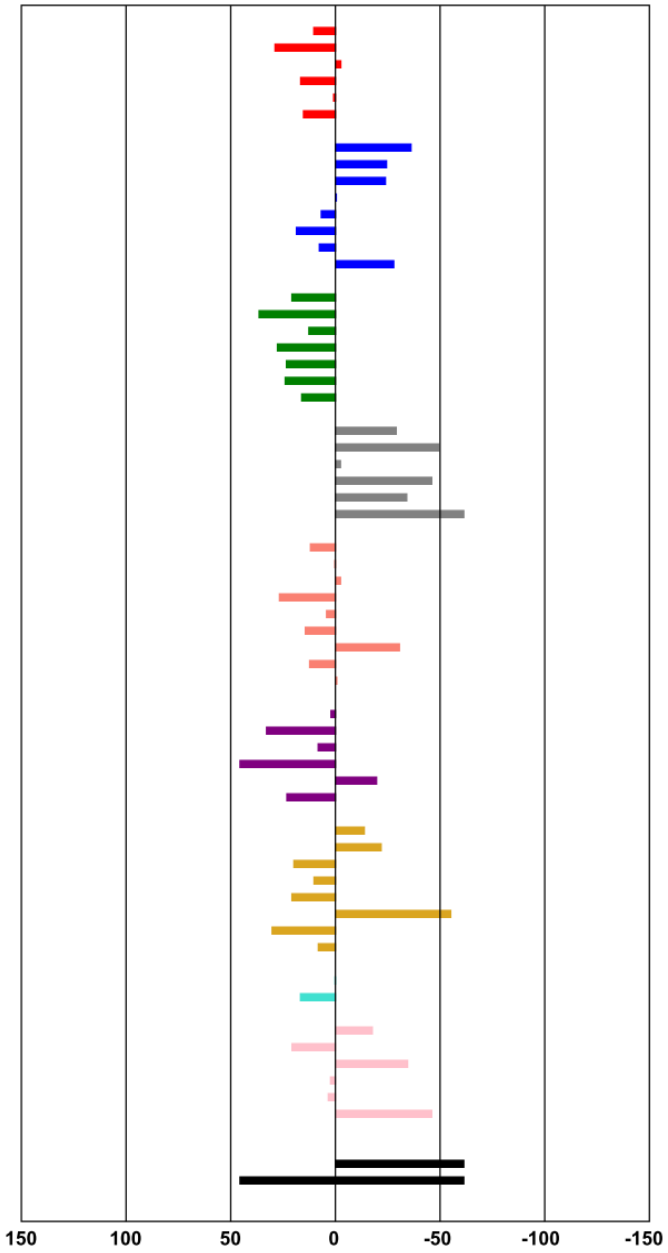

Figure S35. NCI-60 single-dose cytotoxicity screen for compound **1** (propyl-bridged macrocycle).

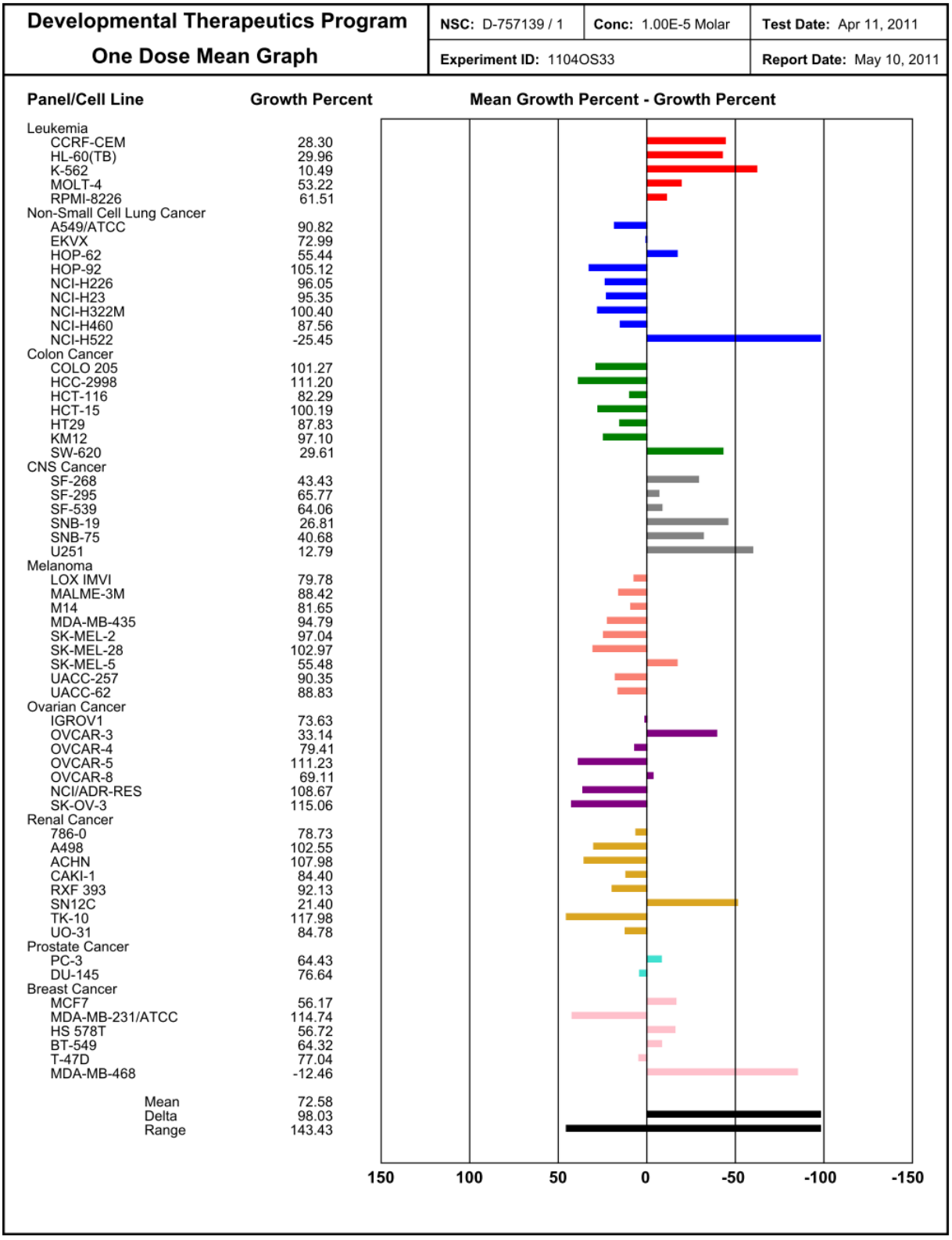

Figure S36. NCI-60 single-dose cytotoxicity screen for compound **2a** (2,2-dimethylpropyl-bridged macrocycle).

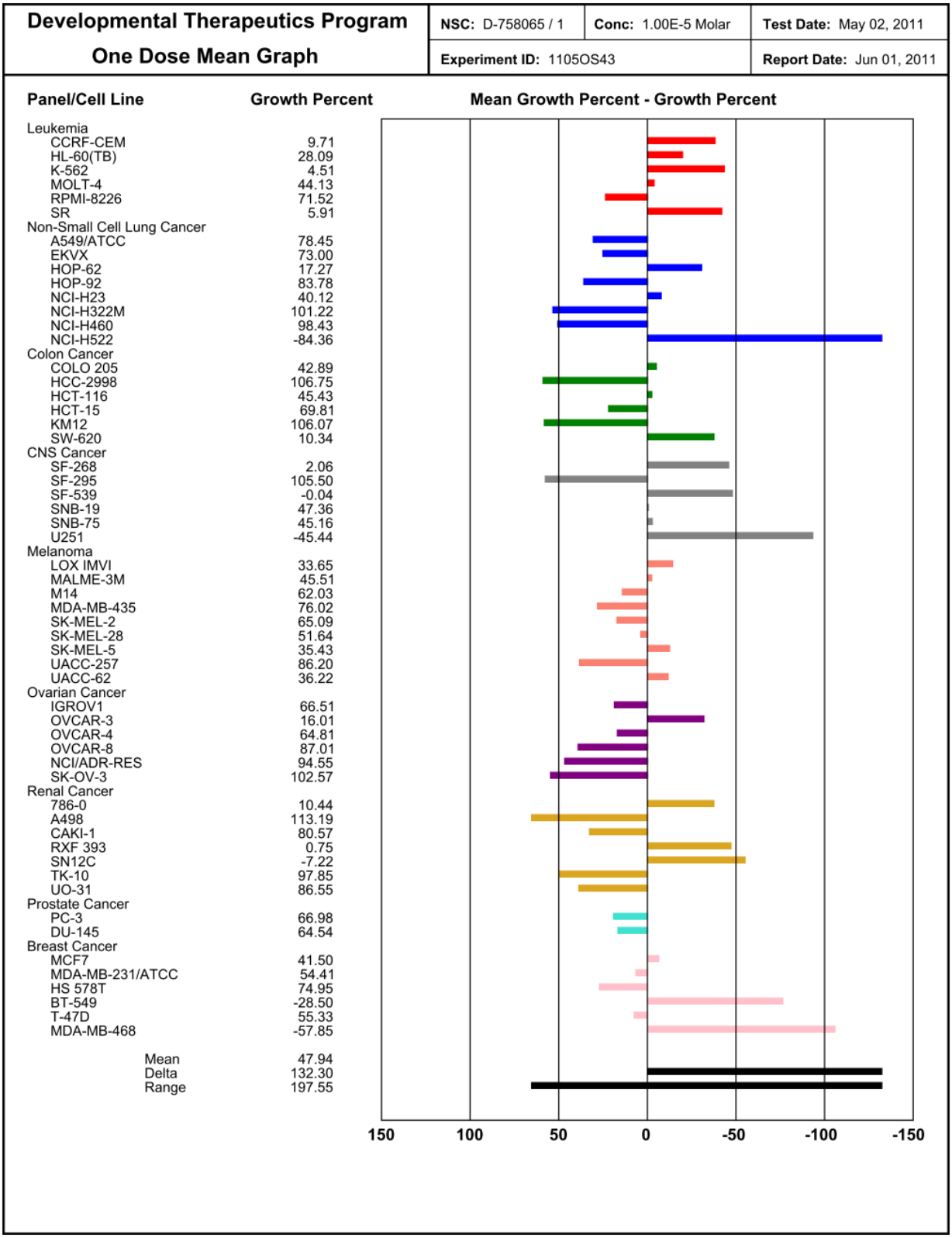

Figure S37. NCI-60 single-dose cytotoxicity screen for compound **3** (butyl-bridged macrocycle).

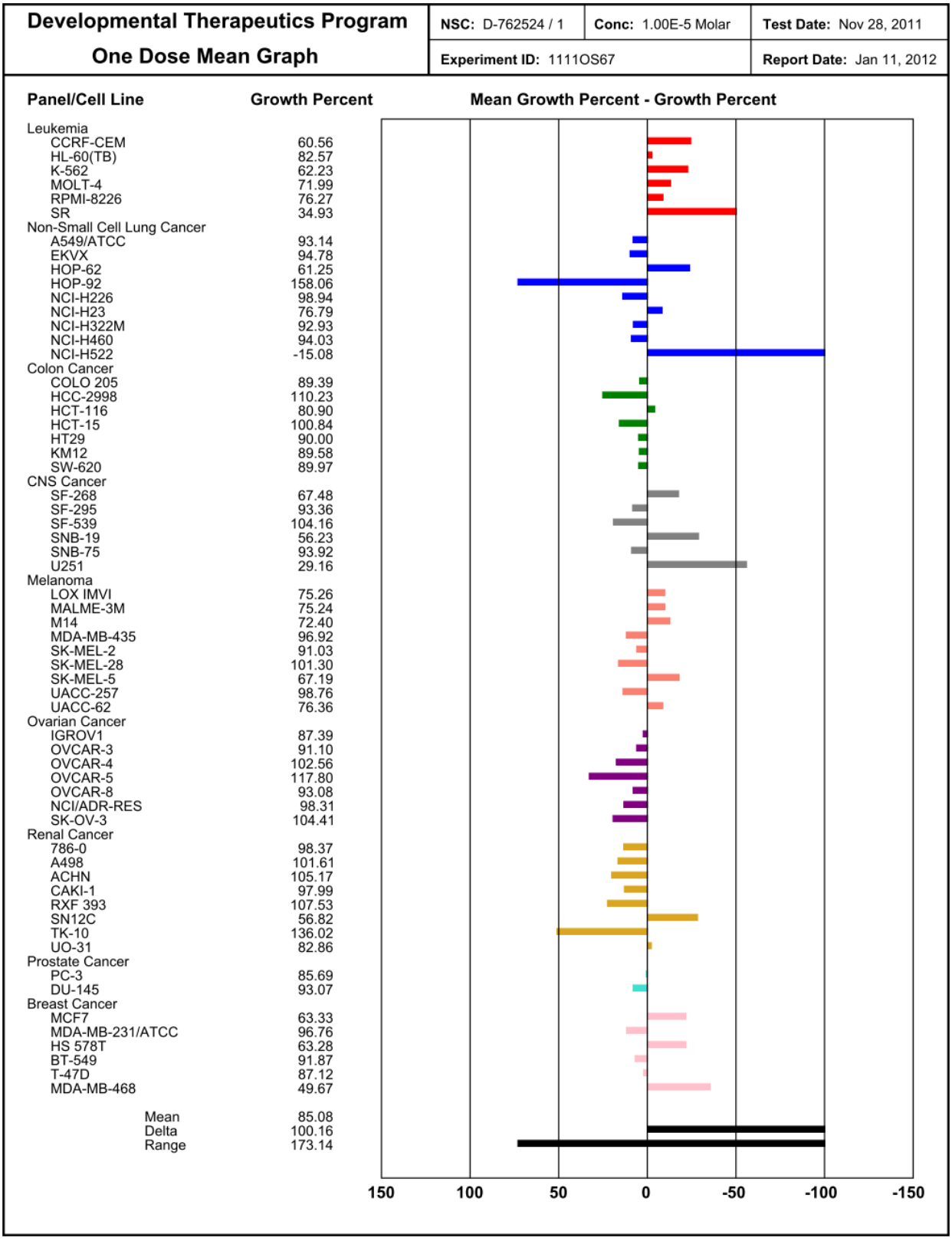

Figure S38. NCI-60 single-dose cytotoxicity screen for compound **4**.

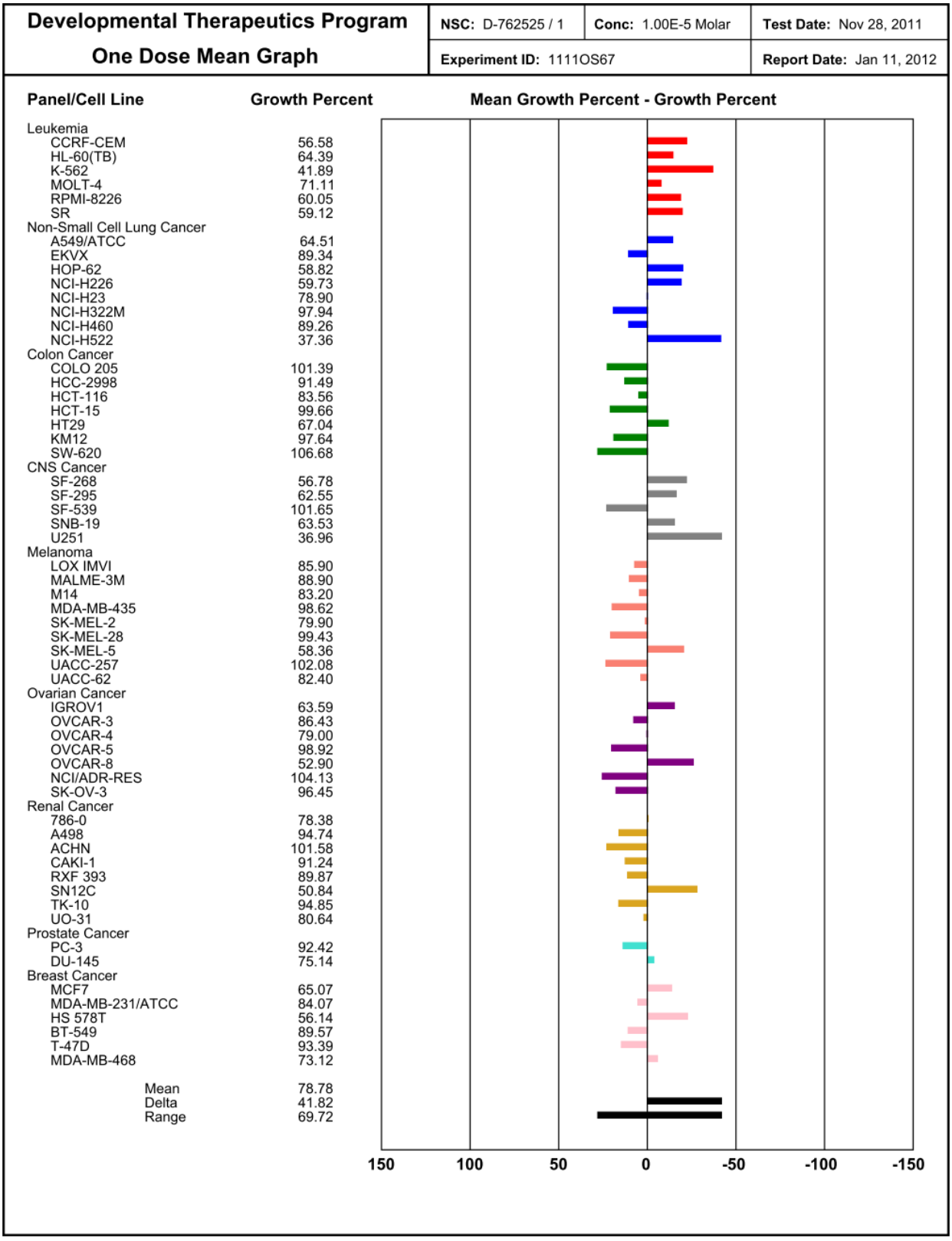

Figure S39. NCI-60 single-dose cytotoxicity screen for compound **5**.

2.3.2 *Five-Dose NCI-60 Cytotoxicity Screen Data for Compounds **2a** and **3***

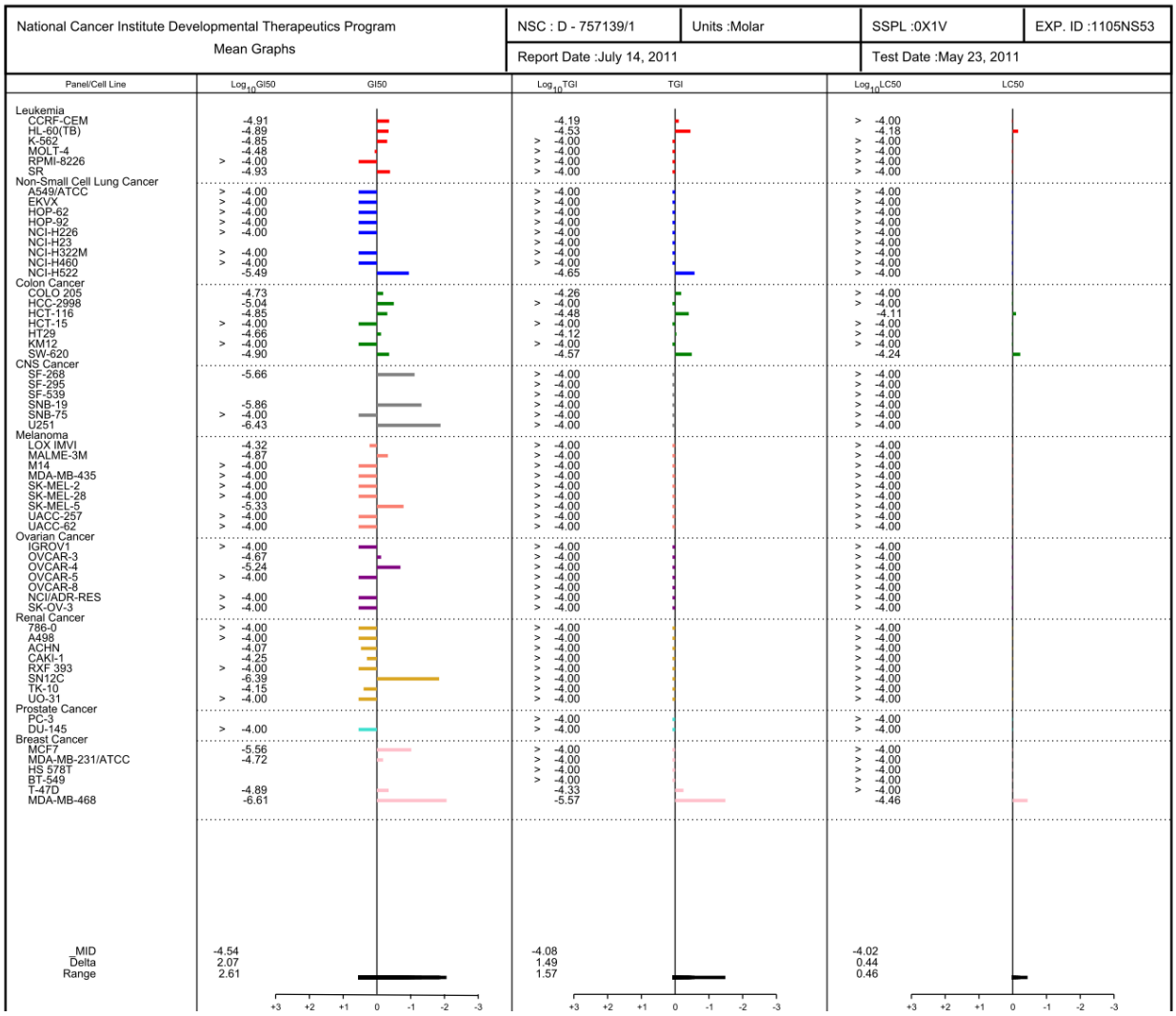

Figure S40. Summary of the five-dose cytotoxicity screen data for **2a** (60 human cancer cell lines, NCI-60 screen). Note that only compounds **2a** and **3** were sufficiently cytotoxic in the single-dose screens to warrant full five-dose screens.

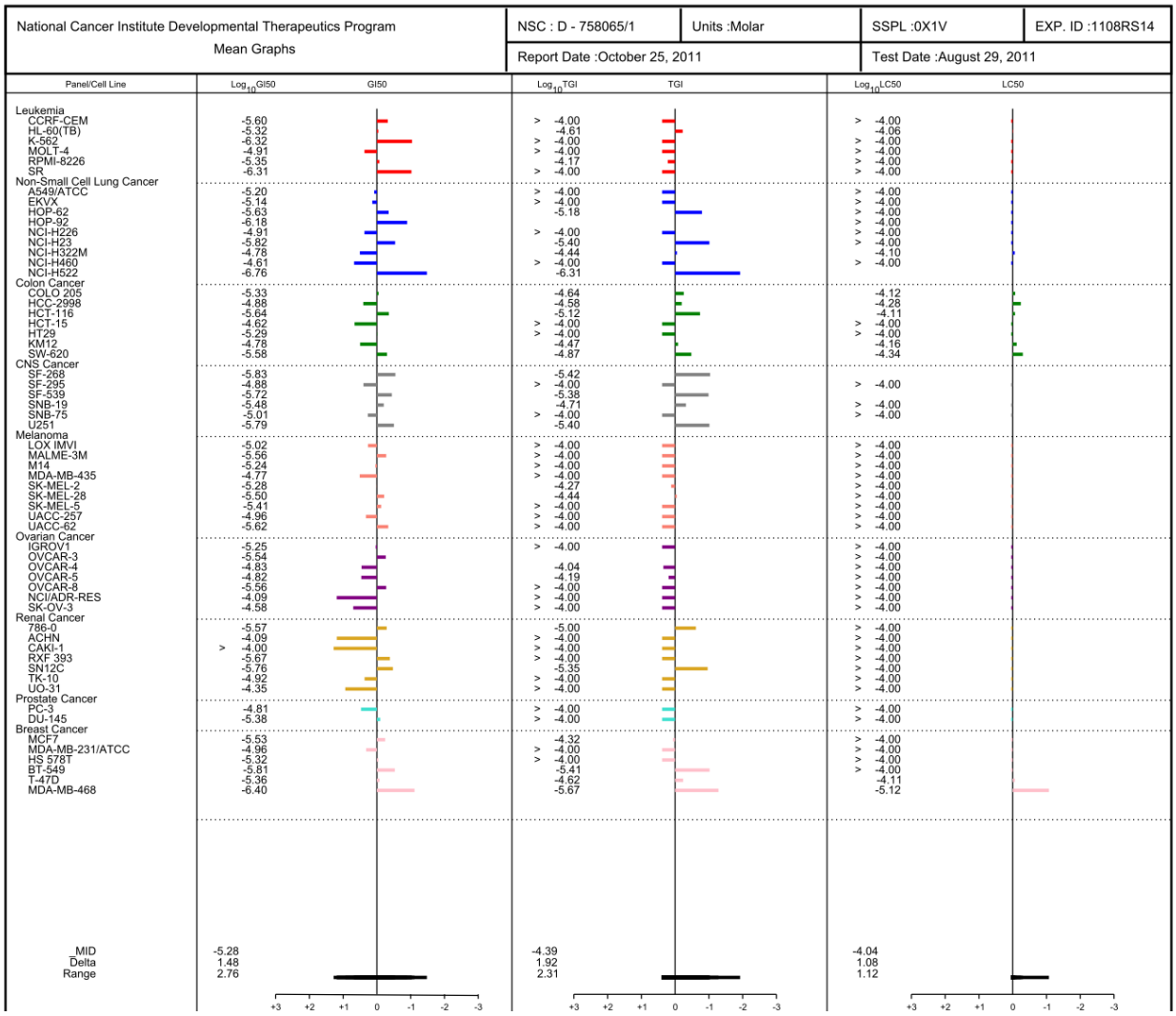

Figure S41. Summary of the repeat 5-dose cytotoxicity screen data for **3** (60 human cancer cell lines, NCI-60 screen). Compound **3** was subsequently selected for further biological evaluation (hollow fibre *in vivo* cytotoxicity assays).

*2.3.3 NCI Animal Toxicology and Cytotoxicity Assays for Compound **3***

Nontumored Animal Toxicity Assay for S758065

Report generated on 27-Jul-2013

EXPERIMENT: AAZ-607 / 0 / 8B	**TUMOR: NO CELLS**	**HOST: Athymic Nudes**	**IMPLANT DATE: 03-APR-2012**
MEMO NO:	**SOURCE/LINE: 0**	**SOURCE: APA**	**STAGING DATE: 03-APR-2012**
BOOK NO:	**IMPLANT SITE: 0**	**SEX: F**	**EVALUATION DATE: 20-APR-2012**

TREATMENT

Grp	NSC	Dose/Units	Rt.	Schedule	Death Days	Surv/Total Day 17
4	D-S758065	100.00 mg/kg/dose	IP	QD X 1, Day 0	--	1/1
5	D-S758065	200.00 mg/kg/dose	IP	QD X 1, Day 0	--	1/1
6	D-S758065	400.00 mg/kg/dose	IP	QD X 1, Day 0	--	1/1

VEHICLES

Grp 4	->	NSC # S758065 / 2 (Dose = 100.00)	: in 100% DMSO	(Smooth suspension - homogeneous)	200.0 mg/ml	Inj. Vol.: 0.5 ul/gm body wt
Grp 5	->	NSC # S758065 / 2 (Dose = 200.00)	: in 100% DMSO	(Smooth suspension - homogeneous)	200.0 mg/ml	Inj. Vol.: 1 ul/gm body wt
Grp 6	->	NSC # S758065 / 2 (Dose = 400.00)	: in 100% DMSO	(Smooth suspension - homogeneous)	200.0 mg/ml	Inj. Vol.: 2 ul/gm body wt

NOTE: All treatment was administered according to exact body weight.

Figure S42. Summary of the NCI animal (nude mice) toxicity assay/determination for compound **3**. The data indicate a 100% survival rate for the mice subjects over the full dose range tested. This class of compounds is evidently well-tolerated by the live animal subjects used for the tests, a result that might reflect the redox-inert nature of the complex.

NSC: 758065

It was tested against the following disease types and cell lines:

Experiment ID: HF1900

Panel Name	Cell Name	Schedule	Route	High Dose
Breast Cancer	MDA-MB-231	QD X 4	IP	150 mg/kg/dose
Non-Small Cell Lung Cancer	NCI-H23	QD X 4	IP	150 mg/kg/dose
Colon Cancer	SW-620	QD X 4	IP	150 mg/kg/dose

Experiment ID: HF1901

Panel Name	Cell Name	Schedule	Route	High Dose
Colon Cancer	COLO 205	QD X 4	IP	150 mg/kg/dose
Melanoma	LOX IMVI	QD X 4	IP	150 mg/kg/dose
Ovarian Cancer	OVCAR-3	QD X 4	IP	150 mg/kg/dose

Experiment ID: HF1902

Panel Name	Cell Name	Schedule	Route	High Dose
Non-Small Cell Lung Cancer	NCI-H522	QD X 4	IP	150 mg/kg/dose
CNS Cancer	U251	QD X 4	IP	150 mg/kg/dose
Melanoma	UACC-62	QD X 4	IP	150 mg/kg/dose

Experiment ID: HF1903

Panel Name	Cell Name	Schedule	Route	High Dose
Melanoma	MDA-MB-435	QD X 4	IP	150 mg/kg/dose
Ovarian Cancer	OVCAR-5	QD X 4	IP	150 mg/kg/dose
CNS Cancer	SF-295	QD X 4	IP	150 mg/kg/dose

Your compound was scored as follows:

IP Score	4 out of 48
SC Score	0 out of 48
Total	4 out of 96
Cell Kill	N

Figure S43. Summary of the NCI hollow fibre cytotoxicity assay data for compound **3** over 12 standard cancer cell lines. The experimental protocol for this assay and the scoring methodology is available from the NCI's website (http://dtp.cancer.gov/branches/btb/hfa.html). In short, compound **3** was insufficiently active/cytotoxic in a live animal model setting to warrant continued investigation. (A minimum IP score of 8 is required for progression to mouse xenograft studies.) Reasons for failure of the compound at this stage of the biological testing regimen are currently undetermined but may include poor physiological and/or cellular transport, off-target binding, and removal by efflux pumps. There is, however, every indication that compound **3** is a "hit compound" worthy of further investigation, structural optimization and/or reformulation into a possible lead metallodrug candidate.

2.4 Enzyme Inhibition Assays

2.4.1 Topoisomerase I (Top1) Inhibition

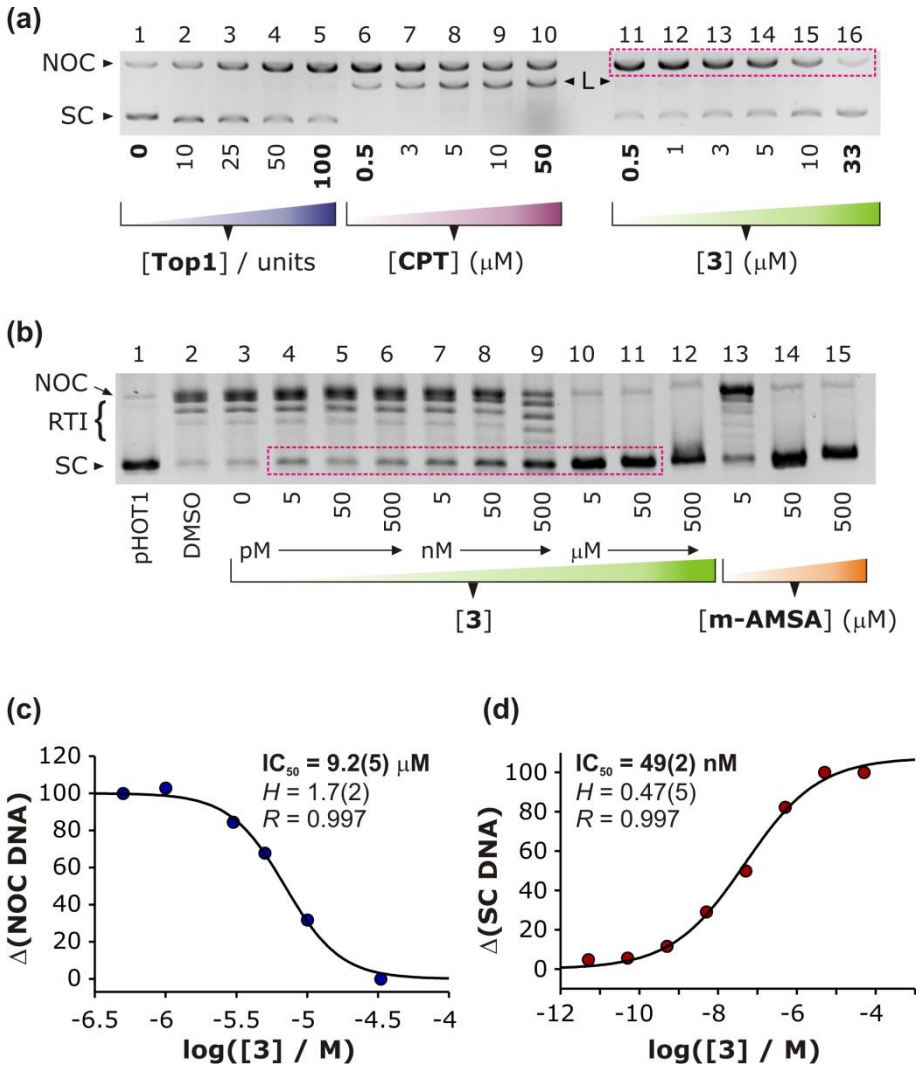

Figure S44. Parts (a) and (b): re-display of the gels shown in Figure 6 of the main text for compound **3** with critical reaction products (dashed rectangles) that may be assayed via standard dose-response functions, $f(x) = 100/(1 + (10^{x}/\boldsymbol{A})^{\boldsymbol{B}})$, where ***A*** corresponds to the IC_{50} value (compound concentration effecting 50% inhibition) and ***B*** is the Hill coefficient. (c) Dose-response function for NOC (nicked-open circular) DNA generated in our new product trapping assay shown in the highlighted rectangle in Part (a); the IC_{50}, Hill coefficient (H), and the correlation coefficient of the nonlinear least-squares fit are indicated on the graph. (d) Dose-response function for SC (supercoiled) DNA generated in a standard Top1 inhibition assay (highlighted rectangle) shown in Part (b); the IC_{50}, Hill coefficient (H), and the correlation coefficient of the nonlinear least-squares fit are indicated on the graph. Note that the IC_{50} values differ for the assays due to the markedly different reaction conditions employed in each case.

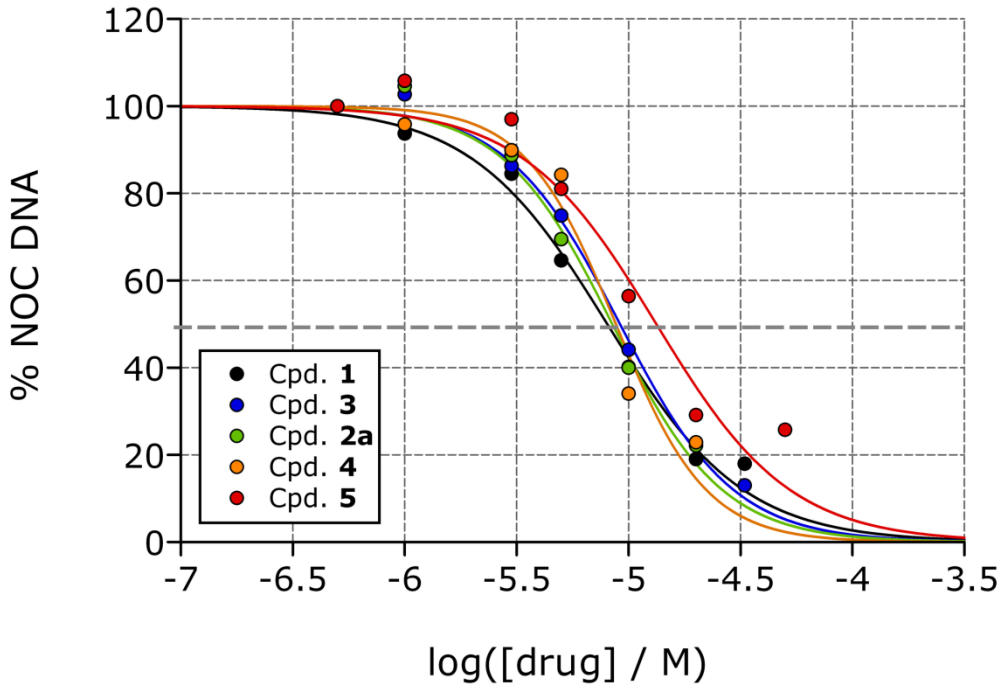

Compound	IC_{50} (μM)	Hill Coefficient	R_{fit}
1	8.0(5)	1.4(1)	0.995
2a	8.5(6)	1.8(2)	0.993
3	9.2(5)	1.7(2)	0.997
4	8.8(9)	2.2(4)	0.981
5	13(2)	2.5(3)	0.974

Figure S45. Analysis of the amount of nicked-open circular DNA (NOC DNA) generated in the reaction of Top1 with pHOT1 plasmid DNA as a function of the concentration of the gold(III) macrocycle present in the reaction solution (see method in Section 1.4.4 and Figure 6b in the main text or Parts (a) and (c) of Figure S44). The data for each compound have been fitted to a standard dose-response function, $f(x) = 100/(1 + (10^{x}/\boldsymbol{A})^{\boldsymbol{B}})$, where ***A*** corresponds to the IC_{50} value (compound concentration effecting 50% inhibition) and ***B*** is the Hill coefficient. For compounds **1–5**, the mean IC_{50} value and Hill coefficient measure 9(2) μM and 1.9(4), respectively.

2.5 Molecular Simulations

*2.5.1 Major Groove Intercalation of Compound **3** at a TA Site in Duplex DNA is Favoured*

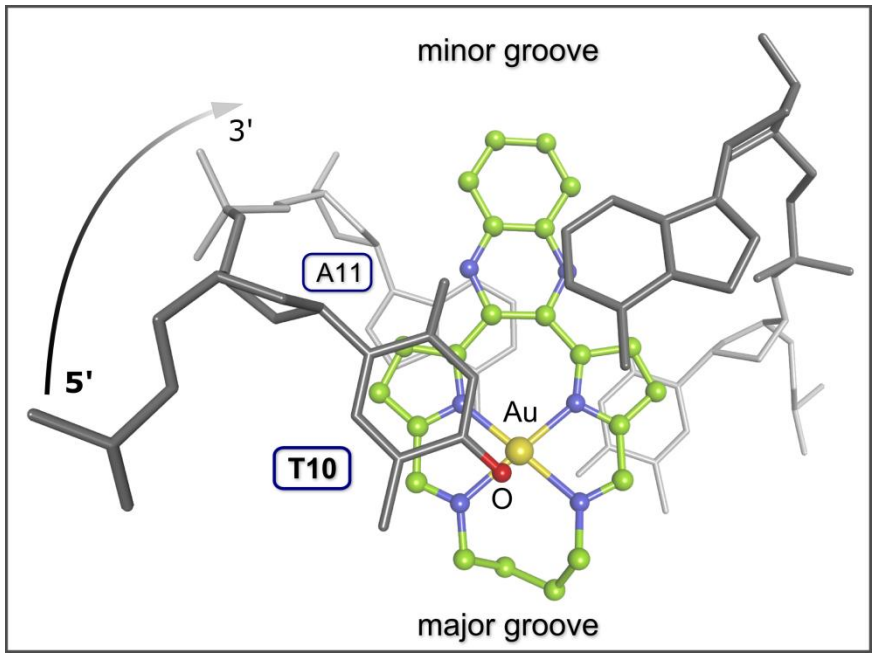

Figure S46. Close-up view of the AMMP/SP4-simulated structure of the binding pocket (T10-A11) of the lowest-energy intercalation adduct (major groove insertion) formed between the 22-bp DNA duplex typically used as a substrate for crystallization of Top1 complexed to DNA[22] and compound **3**. The full DNA sequence used in the simulation is given below (binding site highlighted in blue):

```
5'-1 2 3 4 5 6 7 8 9 10 11 12 13 14 15 16 17 18 19 20 21 22-3'
   A A A A A G A C T T  A  G  A  A  A  A  A  T  T  T  T  T
   T T T T T C T G A A  T  C  T  T  T  T  T  A  A  A  A  A
```

The viewpoint is roughly perpendicular to the plane of the AuN_4 coordination group. The π-stacking between the nucleobases and the pyrrole and quinoxaline ring systems of compound **3** is highlighted by the perspective along with the juxtaposition of the carbonyl oxygen atom (red sphere) of T10 and the Au^{3+} ion (yellow sphere) of the intercalator. The Au···O distance is 3.13 Å (see main text for details). The structure of **3** is shown as a ball and stick model with the following color scheme: C, green; N, blue; Au, gold. The DNA is rendered as a stick model in shades of grey. Hydrogen atoms have been omitted for clarity.

2.5.2 Intercalation via the Minor Groove at a TA Binding Site is Less Favoured

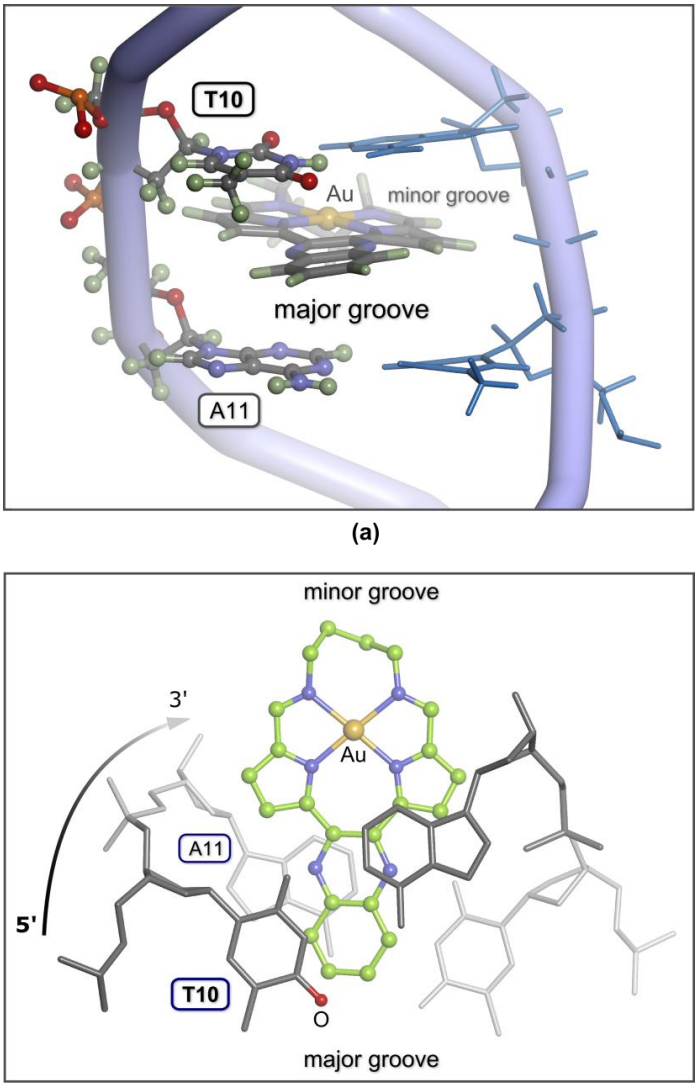

Figure S47. Close-up views of the AMMP/SP4-simulated structure of the binding pocket (T10-A11) of the minor groove intercalation adduct formed between the 22-bp DNA duplex typically used as a substrate for crystallization of Top1 complexed to DNA[22] and compound **3**. The full DNA sequence used in the simulation is given in Figure S46. (a) View from the major groove side (quinoxaline ring edge of compound **3**) highlighting the nonplanarity of the Au^{3+} macrocycle. The distinct conformational distortion upon intercalation via the minor groove is one of the factors underpinning the higher energy of this conformation relative to the global minimum (Figure S46). (b) Top view of the minor groove intercalation adduct highlighting partial intercalation of the Au^{3+} macrocycle and the practically negligible π–π overlap of the pyrrole rings with the T and A bases of the binding pocket. This view clearly explains why the minor groove T10-A11 intercalation adduct is 45.6 kJ mol^{-1} higher in energy than the lowest-energy conformation (Figure S46). Rendering models for Part (a): ball-and-stick for T10-A11, predominantly stick for **3**, and thin blue sticks for the bases complementary to T10-A11; standard CPK colours are used with the exception of H (olive green). The same rendering scheme used in Figure S46 has been used in Part (b).

*2.5.3 Compound **3** forms a Significantly Less-Stable A10-T11 Intercalation Adduct*

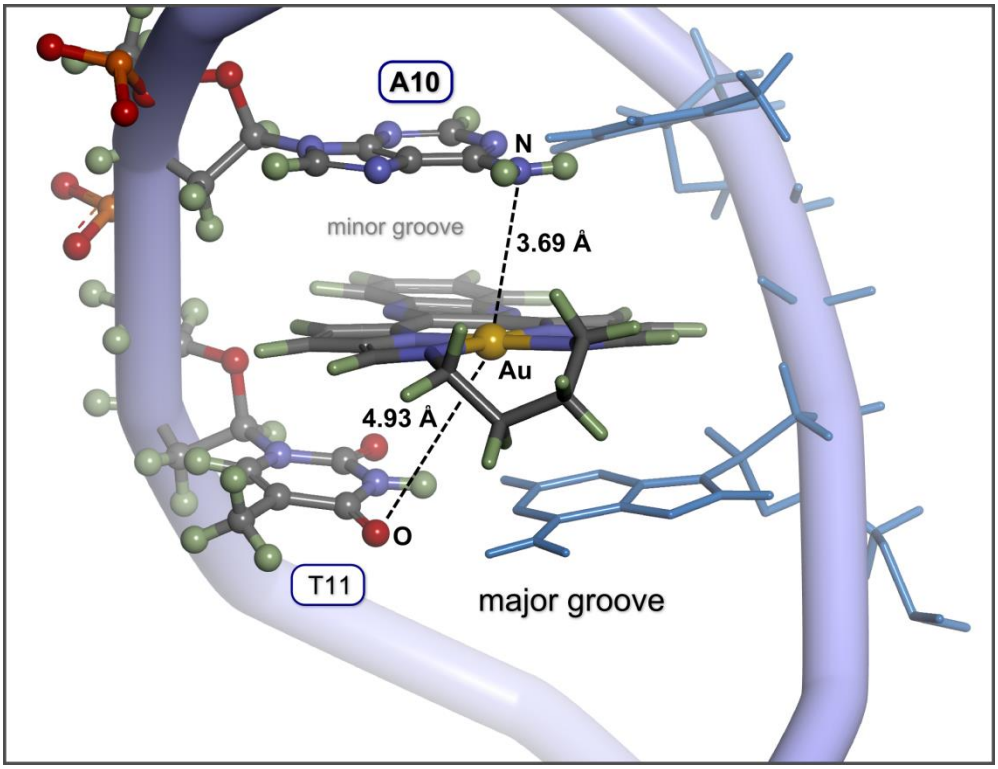

Figure S48. Close-up view of the AMMP/SP4-simulated structure of the DNA binding pocket and intercalator (compound **3**; major groove intercalation adduct) when the nucleotide sequence is switched (mutated) from the normal T10-A11 adjacent pair to an A10-T11 adjacent pair in the 22-bp DNA duplex typically used as a substrate for crystallization of Top1 complexed to DNA[22]. The full DNA sequence used in the simulation is given below (binding site highlighted in red):

```
5'-1 2 3 4 5 6 7 8 9 10 11 12 13 14 15 16 17 18 19 20 21 22-3'
  A A A A A G A C T A  T  G  A  A  A  A  A  T  T  T  T  T
  T T T T T C T G A T  A  C  T  T  T  T  T  A  A  A  A  A
```

Notably, there are no suitably short $Au^{3+}\cdots X$ contacts, where X is a heteroatom, to suggest a strongly electrostatically-stabilized binding interaction. The Au···O and Au···N distances highlighted are longer than the sum of the van der Waals radii of the interacting atoms ($r_{VDW[Au,O]}$ = 3.18 Å; $r_{VDW[Au,N]}$ = 3.21 Å). The above isomeric A10-T11 intercalation structure is 82.0 kJ mol^{-1} (19.6 kcal mol^{-1}) higher in energy than the global minimum energy structure (E_{rel} = 0.0 kJ mol^{-1}) in which the preferred dinucleotide sequence T10-A11 is present. Rendering models: ball-and-stick for A10-T11, predominantly stick for **3**, and thin blue sticks for the bases complementary to A10-T11; standard CPK colours are used with the exception of H (olive green).

2.6 Surface Plasmon Resonance (SPR)

*2.6.1 Intercalation of DNA by **3***

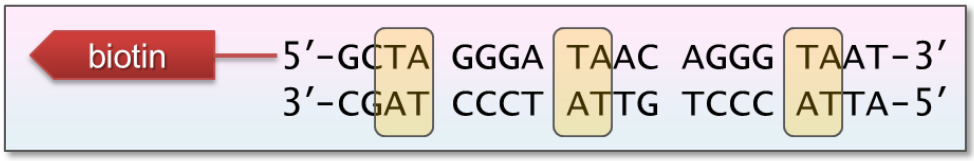

Figure S49. On-chip DNA duplex sequence with TA sites highlighted. This DNA sequence was used for all SPR work either as the analyte (without the biotin tag) or as the immobilized target (biotin tag bound to covalently attached avidin on the commercial SPR chip surface).

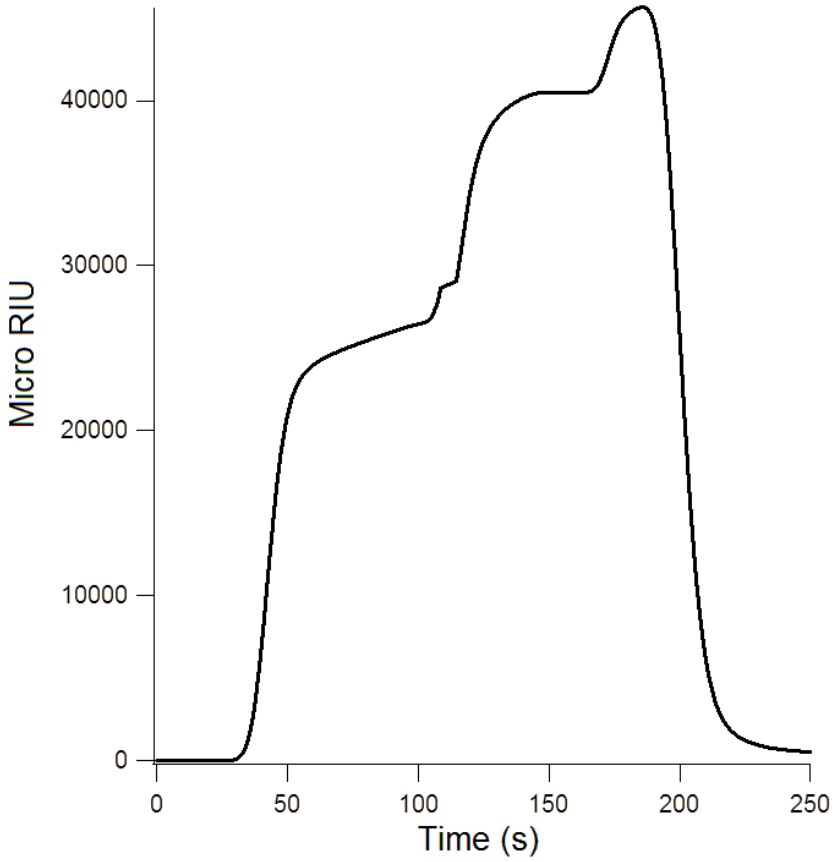

Figure S50. Graph of the time-dependent SPR response function (pH 7.4, 37 °C) obtained for flow-equilibration of compound **3** (50 nM) with the target, chip-immobilized DNA sequence shown in Figure S49. Three association events in the time domains 35–60 s, 110–140 s, and 160–175 s precede dissociation of **3** from the chip (time > 180 s). The data are consistent with binding of **3** at the three highlighted (target) TA sites; each site has a unique microscopic binding constant.

*2.6.2 Compound **3** Inhibits DNA Binding by mTop1 (Y723F Mutant Top1)*

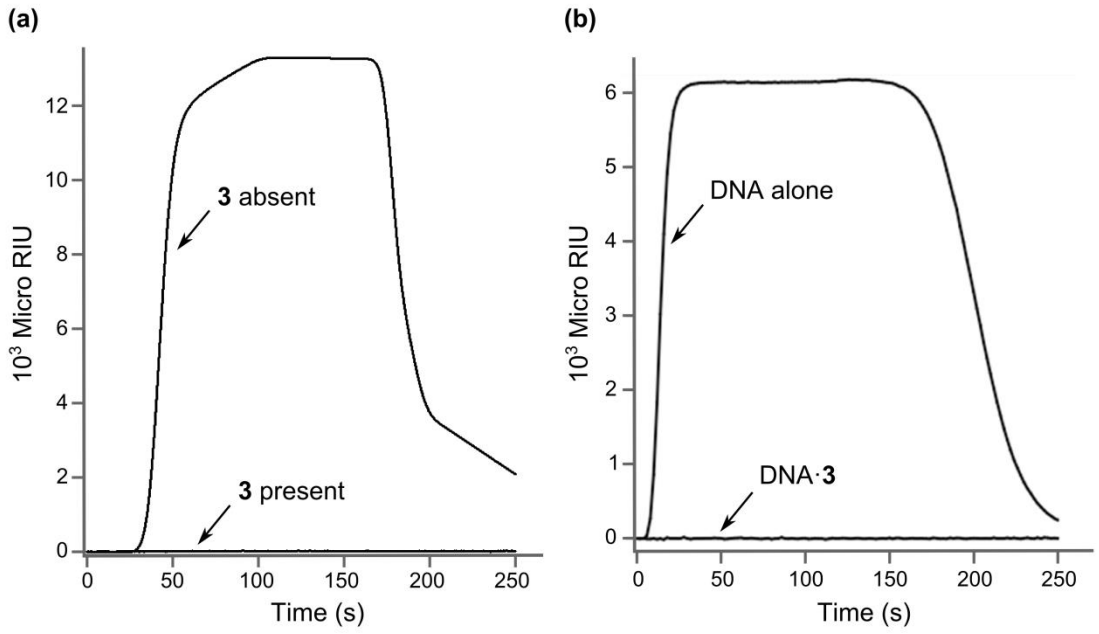

Figure S51. (a) Binding of mTop1 (Y723F mutant Top1) to the chip-immobilized DNA target in Figure S49. A buffered solution of mTop1 (1.5 ng μL^{-1}, pH 7.4, 37 °C) was flow equilibrated over the chip for 250 s. The hump-shaped SPR response function reflects association of mTop1 with the DNA (40–100 s), saturation of the target (100–160 s), and desorption of mTop1 from the chip (> 160 s). In the second experiment, the buffered solution of mTop1 contained compound **3** at a concentration of 50 nM. No SPR response function was obtained (baseline data in figure), proving that **3** blocks DNA binding by mTop1. (b) Binding of DNA with the sequence shown in Figure S49 (minus the biotin tag) to catalytically inactive mTop1 bound to the surface of the SPR chip. A buffered solution of the DNA substrate (0.35 ng μL^{-1}, pH 7.4, 37 °C) was flow-equilibrated over the chip for 250 s to give the hump-shaped SPR response function. The data reflect DNA uptake by the enzyme (association, 5–20 s), followed by saturation (20–170 s), and desorption (> 170 s). In the second experiment, the buffered DNA solution contained compound **3** at a concentration of 50 nM (equilibrated for 5 min with the DNA at 37 °C prior to injection). No SPR response was detected (baseline data in the figure), proving that **3** blocks mTop1 from binding the DNA substrate.

*2.6.3 Compound **3** Does Not Bind to mTop1 (Y723F Mutant Top1)*

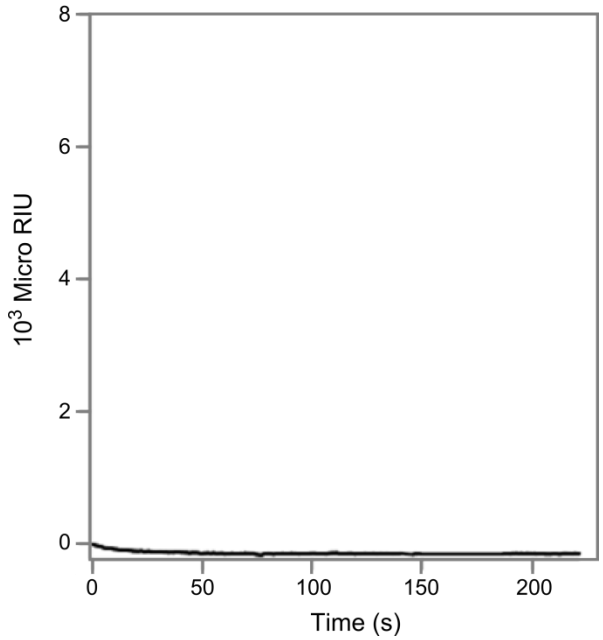

Figure S52. SPR response for the reaction of compound **3** (500 nM in 1X HBS buffer solution at 37 °C) with catalytically inactive mTop1 (Y723F mutant Top1) bound to the surface of the SPR chip. The lack of an SPR response function clearly indicates that compound **3** does not bind to the protein. (1X HBS buffer solution: 10 mM HEPES, pH 7.4, 150 mM NaCl, 3 mM EDTA, 10% DMSO.)

*2.6.4 SPR Derived Binding Constants for **1** and **3***

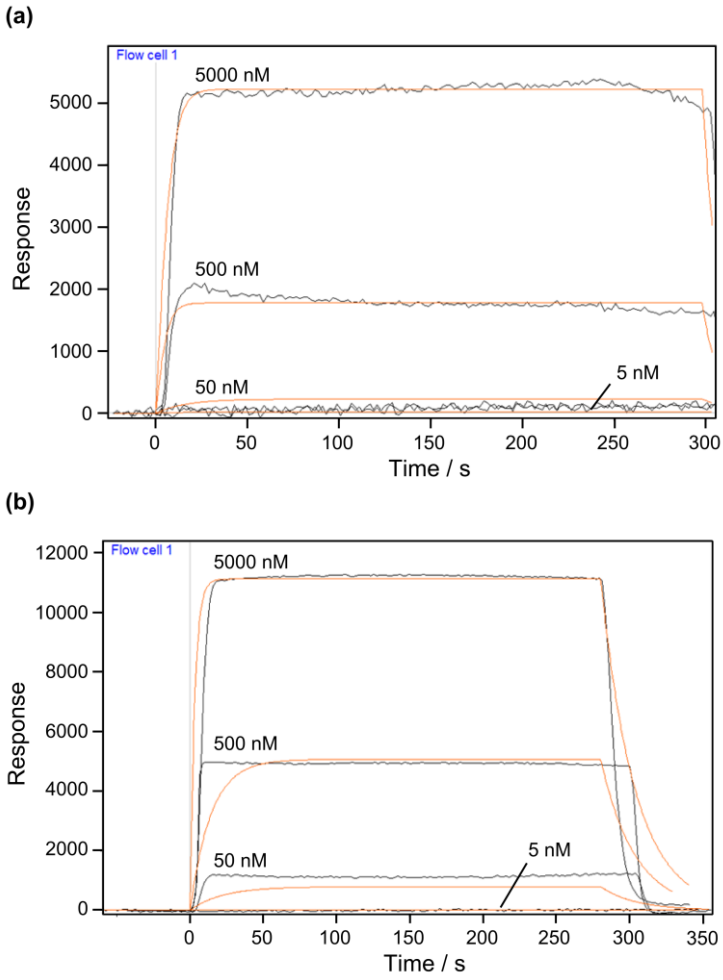

Figure S53. SPR experiments to determine the macroscopic binding constants of **1** (a) and **3** (b) to the 20-bp DNA target depicted in Figure S49. The experiments were conducted as described in Section 1.4.6 at pH 7.4 and 37 °C. The rate and equilibrium data are summarized in Table S4. The best fits to the response profiles (standard association-dissociation rate profile equation available in the instrument's analytical software) are depicted in red. The modest fits afforded derived rate data accurate to only two significant figures at best.

2.7 Additional Topoisomerase Assays

2.7.1 DNA Unwinding Assay Using Supercoiled pHOT1 Plasmid DNA

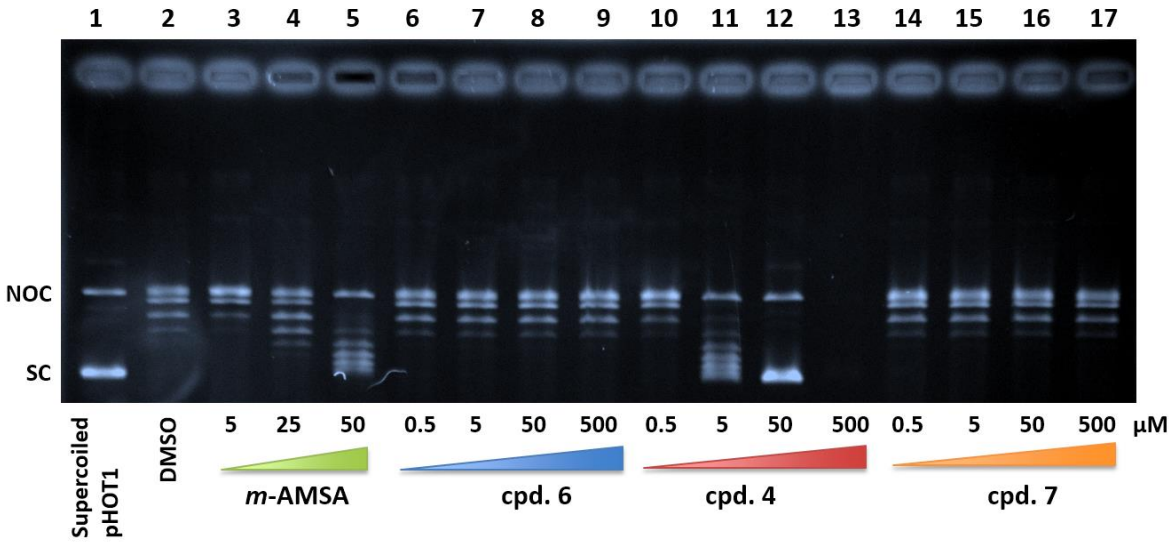

Figure S54. DNA unwinding assay performed with supercoiled pHOT1 plasmid DNA (100 ng per reaction) as the substrate and Top1 (10 units, lanes 2–17). The gel was run for 2h at 25 V in the absence of ethidium bromide. Abbreviations: NOC, nicked-open circular DNA; SC, supercoiled; *m*-AMSA, 4'-(9-acridinylamino)methanesulfon-*m*-anisidide (DNA intercalator control). Compound **6** is the free-base propyl-bridged macrocycle, compound **4** is the Au^{3+} macrocycle with a 2-chloropropyl bridge, and compound **7** is the Ni^{2+} macrocycle with a propyl bridge. Lane 1, SC pHOT1 (no Top1); lane 2, relaxed pHOT1; lanes 3–17, increasing concentrations of the indicated compounds. Only the Au^{3+} macrocycle, compound **4**, matches and surpasses the DNA unwinding capability of *m*-AMSA. The assay indicates that even at a concentration of 5 μM, **4** exceeds the DNA unwinding ability of the DNA intercalator control at 50 μM. Furthermore, neither the free base macrocycle **6** nor the Ni^{2+} macrocycle **7** are DNA intercalators.

Description of some limitations and strengths of the DNA unwinding assay. According to the theory,[31] addition of an intercalator to relaxed circular dsDNA induces positive supercoiling because *Wr* = 0 initially for the relaxed plasmid and binding of the intercalator decreases *Tw*, requiring a compensatory increase in *Wr* (eq 1).

$$Lk = Tw + Wr \quad (1)$$

This torque increase is sensed by Top1 present in the reaction; the enzyme effects relaxation of the substrate and in so doing changes the linking number *Lk* relative to that of the relaxed plasmid (Lk_0). Denaturation of Top1 and drug extraction yields negatively supercoiled DNA in the form of

different topoisomers bands (which satisfy the relationship ΔLk = ±1). The banding pattern is manifest when the drug concentration is high enough to effect intercalation, but not high enough to inhibit Top1 (which may occur in the case of catalytic inhibitors of the enzyme). For drug-saturated plasmid DNA under conditions that lead to full inhibition of Top1, the linking number of the drug-bound plasmid will remain equal to that of the relaxed plasmid ($Lk^{sat} = Lk_0$). Because of the greatly reduced twist accompanying saturating intercalation ($Tw^{sat} << Tw_0$), $Wr^{sat} >> Wr_0$ and the fully positively supercoiled plasmid is recovered after work-up. In a one-dimensional gel electrophoresis experiment, the band migrates equivalently to the native, negatively supercoiled plasmid and it is not possible to determine from the assay whether the maximally supercoiled DNA reaction product (e.g. lane 8, Figure 4c, main text) is the result solely of intercalator-induced torque, or high-dose catalytic inhibition of Top1 by the compound.[31,32]

*2.7.2 Top2 Kinetoplast DNA Decatenation Assay for **3***

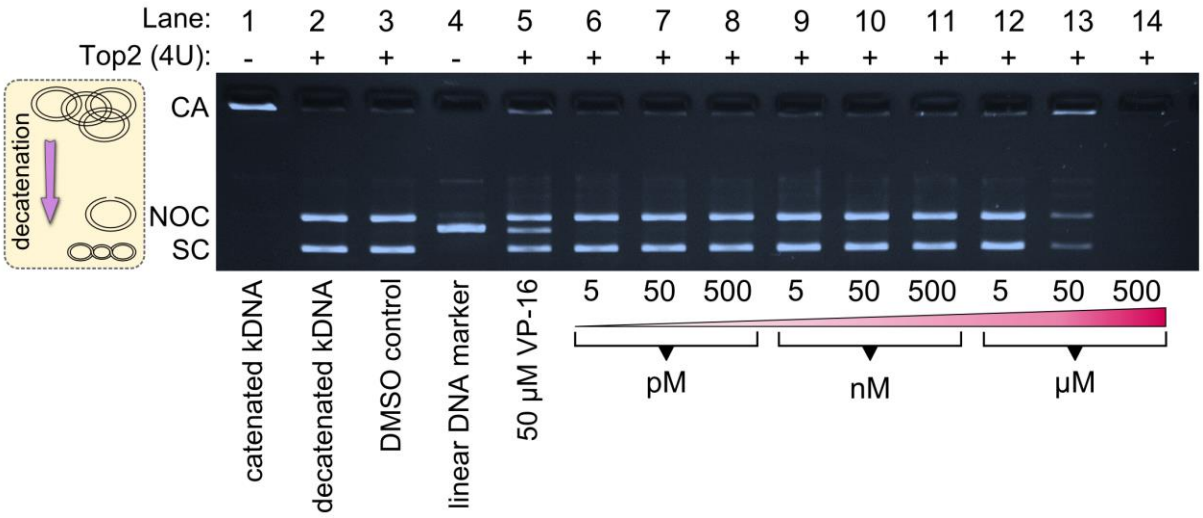

Figure S55. Electrophoretic analysis of a Top2α kinetoplast DNA (kDNA) decatenation assay (1% agarose gel, 0.5 µg mL^{-1} ethidium bromide, EB). The enzyme concentration was 4 units (U) per µL and 200 ng μL^{-1} of kDNA was used in the reaction (50 ng per well). Etoposide (VP-16) at a concentration of 50 µM was used as the Top2α poison control. All annotated lanes, unless otherwise indicated, contain Top2α. In contrast to the lane containing VP-16, none of the lanes with **3** (6–14) exhibit linear DNA as a reaction product. This indicates that **3** is not an interfacial poison of Top2α. However, catalytic inhibition of the enzyme occurs at [**3**] = 50 µM as evidenced by the diminished intensity of the SC and NOC DNA bands and the trapping of catenated kDNA in the well. At [**3**] = 500 µM the DNA appears to have "vanished". This is caused by saturation of the EB binding sites by the metallointercalator such that the DNA cannot take up the dye for conventional visualization by EB emission. Abbreviations: NOC, nicked-open circular; SC, supercoiled; CA, catenated.

*2.7.3 Product-Trapping Assay (High Top1:DNA Ratio) for Compound **1***

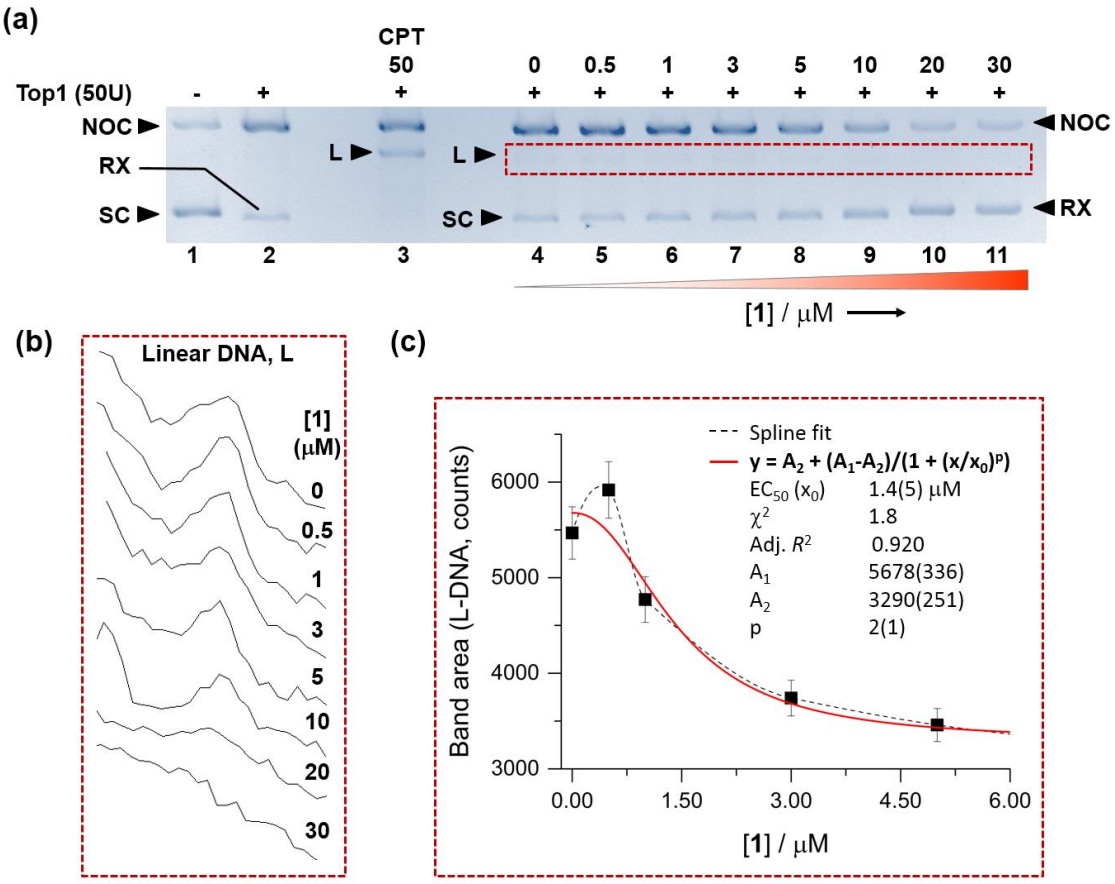

Figure S56. (a) Gel-based product-trapping assay using a high Top1:DNA ratio (50 units of Top1 per reaction) and 0 mM NaCl ([pHOT1] = 31.3 ng/well in all reactions) for increasing compound **1** concentrations from 0.5 to 30 μM (lanes 4–11). Lane 1, supercoiled pHOT1 plasmid DNA substrate in the absence of Top1; Lane 2, relaxed pHOT1 DNA; Lane 3, reaction products in the presence of 50 μM camptothecin (CPT; Top1 interfacial poison control). Abbreviations: SC, supercoiled; NOC, nicked-open circular; RX, relaxed; L, linear. (b) Band profiles for the low-intensity linear DNA bands evident in lanes 4–11 of the gel. (c) Nonlinear fit (sigmoidal dose-response function) of the linear DNA band integrated intensities (lanes 4–11) with increasing [**1**]. Error bars are set at 5%. The Akima spline fit (dashed line) suggests that the linear DNA concentration increases slightly at [**1**] = 500 nM before decreasing along the path of a normal dose-response function. Collectively, the data show that a minor quantity of linear DNA (< 1%) is generated in the reaction and that the yield is dose-dependent. It is important to note that the ability of **1** to generate linear DNA by trapping ternary drug-DNA-Top1 covalent cleavage complexes is weak compared with CPT (lane 3). However, the data clearly suggest that at low concentrations, compound **1** may act as a weak interfacial poison of Top1. This observation explains the positive readout seen in the solid-phase assay plotted in Figure 6a of the main text for concentrations of **1** between 0.1 and 1 μM. Note that [L-DNA] > 0 when [**1**] = 0 because the action of Top1 at a high concentration causes not only elevated single-strand nicks (yielding NOC DNA) but also some double-strand breaks (yielding linear DNA), even in the absence of an IFP like CPT.

2.8 DNA Melting Curve Analyses: Intercalation

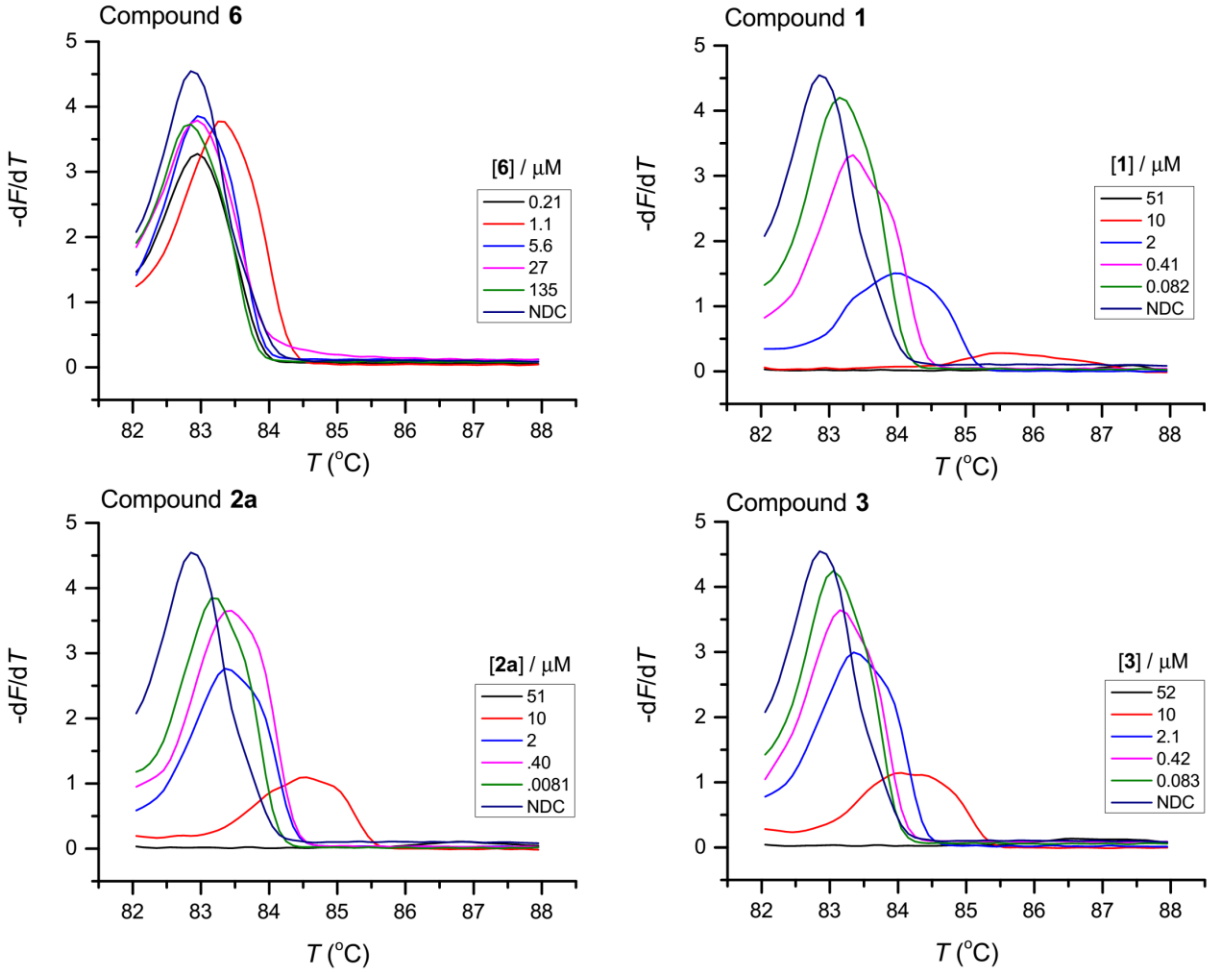

Figure S57. High-resolution melt (HRM) curves for a linear 291-bp dsDNA fragment (pH 8.4) derived from the human ACTN3 gene as a function of the concentration of compounds **1**–**3** and **6**. The plots reflect the negative first derivative of the fluorescence intensity (–d*F*/d*T*, 510 nm) from the DNA-intercalating reporter dye (CYBR ® Green) used to monitor strand separation. (NDC; no drug control, DMSO.) Relative to the metal-free macrocycle (**6**), the Au^{3+} macrocycles all induce an upward shift in the melting point of the DNA substrate consistent with intercalation of the DNA. The effect is most pronounced for **1**. Compound **6** has a negligible effect on the DNA melting point (mean = 83.0(1) °C), confirming that the Au^{3+} ion is required for intercalative binding.

3. Supplementary Tables

Table S1. Crystal system data, X-ray data collection, and structure refinement details for compounds **1**–**3**.

	1	**2b**	**3**
Crystal data			
Chemical formula	$C_{21}H_{16}AuN_6{\cdot}F_6P$	$C_{23}H_{20}AuN_6{\cdot}CF_3O_3S$	$C_{22}H_{18}AuN_6{\cdot}F_6P{\cdot}C_2H_3N$
M_r	694.33	726.49	749.41
Crystal system, space group	Monoclinic, $P2/c$	Monoclinic, Cc	Orthorhombic, $Pna2_1$
Temperature (K)	173(2)	120(2)	100(2)
a, b, c (Å)	16.473 (5), 6.980 (5), 18.804 (5)	17.092 (5), 25.520 (5), 13.625 (5)	43.9022 (11), 6.7597 (2), 48.8964 (12)
β (°)	105.675 (5)	119.057 (5)	90.0
V (Å^3)	2081.7 (17)	5195 (3)	14510.8 (7)
Z	4	8	24
Radiation type	Mo $K\alpha$	Mo $K\alpha$	Cu $K\alpha$
μ (mm^{-1})	7.22	5.80	12.76
Crystal size (mm)	0.50 × 0.02 × 0.01	0.3 × 0.1 × 0.07	0.12 × 0.02 × 0.02
Data collection			
Diffractometer	Xcalibur, Sapphire2	Xcalibur, Sapphire2	Bruker X8 Prospector
Absorption correction	Multi-scan *CrysAlis RED*, Oxford Diffraction Ltd., Version 1.171.33.55.	Multi-scan *CrysAlis RED*, Oxford Diffraction Ltd., Version 1.171.33.55	Numerical *SADABS*: Area-Detector Absorption Correction. (1996) Siemens Industrial Automation, Inc.: Madison, WI.
T_{min}, T_{max}	0.497, 1.000	0.404, 1.000	0.310, 0.812
No. of measured, independent and observed [$I > 2\sigma(I)$] reflections	14581, 4010, 3153	18989, 7796, 5734	101016, 24413, 20623
R_{int}	0.060	0.073	0.098
Refinement			
$R[F^2 > 2\sigma(F^2)]$, $wR(F^2)$, S	0.032, 0.073, 0.94	0.05, 0.105, 0.94	0.052, 0.113, 1.06
No. of reflections	4010	7796	24413
No. of parameters	316	665	2114
No. of restraints	0	455	2247
H-atom parameters (treatment)	Constrained	Constrained	Constrained
Weighting function			$w = 1/[\sigma^2(F_o^2) + (0.0319P)^2 + 102.1494P]$ where $P = (F_o^2 + 2F_c^2)/3$
$\Delta\rangle_{max}$, $\Delta\rangle_{min}$ (e Å^{-3})	2.28, -1.45	2.42, -1.60	2.02, -2.00

Table S2. Selected mean crystallographic and calculated structural and conformational parameters for compounds **1**–**3**.[a]

	1			2b			3		
	X-ray	**DFT**	**MM**	**X-ray**	**DFT**	**MM**	**X-ray**	**DFT**	**MM**
Bond distances (Å)									
$Au–N_{pyrrole}$	1.99(1)	1.98	1.95	1.98(1)	1.98	1.95	1.98(1)	1.99(1)	1.96
$Au–N_{imine}$	2.01(1)	2.02	1.99	2.00(1)	2.02	1.99	2.02(2)	2.05(5)	2.03(1)
C=N	1.31(1)	1.33	1.26	1.32(5)	1.33	1.27	1.30(3)	1.33	1.27
Bond angles (°)									
$N_{pyrrole}–Au–N_{pyrrole}$	99.2(2)	99.1	97.5	100.2(1.6)	99.1	97.3	97.1(8)	97.4	98.0
cis- $N_{pyrrole}–Au–N_{imine}$	81.8(1)	82.1	82.6(1)	81.7(1.0)	82.3	82.7(1)	81.9(8)	81.8(1)	81.4(2)
trans- $N_{pyrrole}–Au–N_{imine}$	177.7(1)	178.6	179.8(2)	177.8(7)	178	179.8(1)	177(1)	176.9(1)	179.0(1)
$N_{imine}–Au–N_{imine}$	97.2(2)	96.7	97.4	96.4(6)	96.2	97.2	99.2(4)	99.3	99.3
$C–N_{pyrrole}–C$	108.5(1)	109.2	109.5(1)	110(2)	109	109.4(1)	108(1)	108.6	109.0(1)
$C–N_{imine}–C$	124.1(5)	124.5	124(1))	124(2)	125	123(1)	121(2)	121.6(5)	119.7(7)
Conformation (pm)[b]									
| Au |	11.2	3.6	3.3	3(2)	7.1	0.0	5.7(31)	1.1	3.0
$\|N_{imine}\|$	6.3(4)	4(0)	6(3)	4(3)	9(0)	1(1)	15.5(8.8)	13(3)	6(5)
$\|N_{pyrrole}\|$	8.8(2)	1(0)	1(1)	2(1)	1(0)	2(0)	3.1(2.6)	2(0)	1(1)
$\|C_{imine}\|$	1.7(8)	2(0)	6(2)	4(1)	3(0)	8(1)	11.7(7.6)	11(1)	7(1)
$\|C_{alpha}\|$	1(1)	1(1)	2(1)	3(2)	3(1)	2(1)	5.6(4.2)	3(1)	2(1)
$\|C_{beta}\|$	16(2)	5(1)	3(2)	3.3(20)	9(0)	4(3)	10.5(7.3)	4(3)	6(6)
$\|C_{quinoxaline}\|$	5(1)	1(0)	3(2)	3.7(16)	1(0)	2(0)	4.0(3.3)	2(1)	2(2)
$\|N_{quinoxaline}\|$	5(4)	0(0)	3(3)	7.8(53)	0(0)	2(0)	7.1(5.4)	6(0)	2(2)
$\|C_{benzene}\|$	3(2)	2(1)	2(2)	6.2(4.2)	3(2)	3(2)	7.7(6.5)	5(2)	2(2)

[a] Estimated standard deviations are given in parentheses (when relevant). [b] Conformational parameters are mean absolute perpendicular displacements of the indicated atoms from the 25-atom mean plane of the Au(III) macrocycle. For crystallographic data, averages are for all cations in the asymmetric unit (ASU) where the ASU contains more than one cation.

Note: both the *in vacuo* DFT and the MM-simulated structures are in good agreement with the X-ray crystal structures of **1**–**3**, particularly when comparing bond distances and bond angles. The conformations of **1**–**3** are mildly distorted from planarity in the crystalline solid state due, in part, to lattice packing interactions. The DFT- and MM-calculated structures are, expectedly, somewhat less distorted as they do not take into account the nonbonded interactions that affect the experimental structures.

Table S3. Summary of spectroscopic and computational data required for three-dimensional analysis of the factors that control the solution phase calf thymus DNA binding affinities of **1**–**5**.

Complex	Log($P_{o/w}$)[a]	Bridge Volume (Å^3)[b]	C_{50} (M)[c]	K_{app} (M^{-1})[c]
1	0.776(29)	258.4	1.63(12) x 10^{-5}	4.2 x 10^6
2a	1.01(31)	351.6	2.98(20) x 10^{-5}	2.3 x 10^6
3	0.878(45)	309.1	3.67(29) x 10^{-5}	1.9 x 10^6
4	1.065(50)	300.9	1.67(17) x 10^{-5}	4.1 x 10^6
5	1.022(19)	258.4	1.56(11) x 10^{-5}	4.4 x 10^6

[a] The log(Po/w) data were recorded as described in Section 1.2.1. [b] The van der Waals volumes of the macrocycle alkyl bridges were calculated using Vega ZZ 3.0.0[19]. [c] The experimental variables for the spectroscopic titrations were: [ethidium bromide, EB] = 1.50 x 10^{-5} M; K_{EB} = 4.6(1.1) x 10^6 M^{-1} (bp); K_{app} = (K_{EB} x [EB]) / C_{50}, where C_{50} is the concentration of **1**, **2a**, and **3**–**5** that leads to 50% quenching of the EB fluorescence intensity (see Section 1.2.2).

Table S4. SPR-derived macroscopic rate and equilibrium constant data for the reaction of complexes **1** and **3** with the chip-immobilized 20-bp duplex DNA target depicted in Figure S49.[a]

Complex	k_{on} (s^{-1})	k_{off} (s^{-1})	K_A	K_D
1	1.6×10^4	4.5×10^{-2}	3.6×10^5	2.8×10^{-6}
3	1.3×10^4	4.3×10^{-2}	3.0×10^5	3.4×10^{-6}

[a] K_A and K_D are association and dissociation constants, respectively.

Table S5. Empirical free energy penalties for DNA base pair separation (ΔG) and MM-calculated relative energies (E_{rel}) for the intercalation of **3** at the indicated base pair site for a 22-bp DNA duplex sequence favoured by human topoisomerase I (Top1). All unique base pairs closest to the mid-point of the DNA duplex were selected for analysis.

Duplex DNA sequence:[a]

5'-A A A A A G A C T **T** **A** G A A A A A T T T T T-3'

1 2 3 4 5 6 7 8 9 **10** **11** 12 13 14 15 16 17 18 19 20 21 22

Index	Base Pair	ΔG (kcal/mol)[b]	E_{rel} major groove (kcal/mol)[c]	E_{rel} minor groove (kcal/mol)[c]
1	AA	0.88	-	-
2	AA	0.88	-	-
3	AA	0.88	-	-
4	AA	0.88	-	-
5	AG	0.67	85.7, D	94.7, D
6	GA	1.02	139.7, D	73.2, D
7	AC	0.57	78.4, D	306.2, U
8	CT	0.67	82.2, D	125.4, U
9	TT	0.88	107.3, D	74.4, U
10	**TA**	0.17	0.0, D	10.9, U
11	AG	0.67	85.9, U	182.1, U
12	GA	1.02	138.2, U	96.4, D
13	AA	0.88	116.4, U	193.0, U
14	AA	0.88	111.2, U	142.6, D
15	AA	0.88	-	-
16	AA	0.88	-	-
17	AT	0.37	38.9, D	24.0, D
18	TT	0.88	-	-
19	TT	0.88	-	-
20	TT	0.88	-	-
21	TT	0.88	-	-

[a] The dsDNA sequence favoured by Top1 is known;[22] single-strand nick site (base pair) for formation of the covalent Top–DNA cleavage complex is highlighted in red (T10–A11). [b] ΔG is the free energy penalty for helix unwinding calculated using WEB-THERMODYN;[23] this empirically-based value is calculated from experimental thermodynamic data[33] and measures helix stability for adjacent base pairs (as done here), or any user-specified oligonucleotide sequence. [c] Relative energy calculated using an augmented version of the SP4 force field[18] and intercalation of **3** via minor or major groove insertion at the target base pair. The energy value reflects the lowest-energy conformation from between 3 and 15 geometry optimization runs for the target structure. D, butyl chain of **3** is oriented downstream (points to the 3' terminus); U, butyl chain of **3** is oriented upstream (points to the 5' terminus). See main text for details.

Table S6. NCI-60 five-dose cytotoxicity screen data for compound **3** (butyl-bridged macrocycle). Parameters: GI50, concentration inducing 50% growth inhibition; IC50, concentration inducing 100% growth inhibition; LC50, concentration causing a 50% cell kill.

Panel	Cell Line	Endpoint	-Log(Value)
Leukemia	HL-60(TB)	GI50	5.83
Leukemia	HL-60(TB)	IC50	5.33
Leukemia	HL-60(TB)	LC50	4
Leukemia	HL-60(TB)	TGI	4.08
Leukemia	MOLT-4	GI50	5.63
Leukemia	MOLT-4	IC50	5.29
Leukemia	MOLT-4	LC50	4
Leukemia	MOLT-4	TGI	4
Leukemia	SR	GI50	6.58
Leukemia	SR	IC50	
Leukemia	SR	LC50	4
Leukemia	SR	TGI	4
Non-Small Cell Lung Cancer	A549/ATCC	GI50	5.18
Non-Small Cell Lung Cancer	A549/ATCC	IC50	4.92
Non-Small Cell Lung Cancer	A549/ATCC	LC50	4
Non-Small Cell Lung Cancer	A549/ATCC	TGI	4
Non-Small Cell Lung Cancer	EKVX	GI50	4.85
Non-Small Cell Lung Cancer	EKVX	IC50	4.16
Non-Small Cell Lung Cancer	EKVX	LC50	4
Non-Small Cell Lung Cancer	EKVX	TGI	4
Non-Small Cell Lung Cancer	HOP-62	GI50	5.75
Non-Small Cell Lung Cancer	HOP-62	IC50	5.4
Non-Small Cell Lung Cancer	HOP-62	LC50	4.08
Non-Small Cell Lung Cancer	HOP-62	TGI	5.23
Non-Small Cell Lung Cancer	HOP-92	GI50	
Non-Small Cell Lung Cancer	HOP-92	IC50	4
Non-Small Cell Lung Cancer	HOP-92	LC50	4
Non-Small Cell Lung Cancer	HOP-92	TGI	4
Non-Small Cell Lung Cancer	NCI-H226	GI50	4.71
Non-Small Cell Lung Cancer	NCI-H226	IC50	4.37
Non-Small Cell Lung Cancer	NCI-H226	LC50	4
Non-Small Cell Lung Cancer	NCI-H226	TGI	4.29
Non-Small Cell Lung Cancer	NCI-H23	GI50	5.48
Non-Small Cell Lung Cancer	NCI-H23	IC50	5.13
Non-Small Cell Lung Cancer	NCI-H23	LC50	4
Non-Small Cell Lung Cancer	NCI-H23	TGI	4.12
Non-Small Cell Lung Cancer	NCI-H322M	GI50	4.71
Non-Small Cell Lung Cancer	NCI-H322M	IC50	4.4

Non-Small Cell Lung Cancer	NCI-H322M	LC50	4.03
Non-Small Cell Lung Cancer	NCI-H322M	TGI	4.37
Non-Small Cell Lung Cancer	NCI-H460	GI50	4.49
Non-Small Cell Lung Cancer	NCI-H460	IC50	4.43
Non-Small Cell Lung Cancer	NCI-H460	LC50	4
Non-Small Cell Lung Cancer	NCI-H460	TGI	4
Non-Small Cell Lung Cancer	NCI-H522	GI50	6.84
Non-Small Cell Lung Cancer	NCI-H522	IC50	6.55
Non-Small Cell Lung Cancer	NCI-H522	LC50	0
Non-Small Cell Lung Cancer	NCI-H522	TGI	6.53
Colon Cancer	COLO 205	GI50	5.55
Colon Cancer	COLO 205	IC50	5.26
Colon Cancer	COLO 205	LC50	4
Colon Cancer	COLO 205	TGI	4.64
Colon Cancer	HCC-2998	GI50	4.77
Colon Cancer	HCC-2998	IC50	4.52
Colon Cancer	HCC-2998	LC50	4.2
Colon Cancer	HCC-2998	TGI	4.48
Colon Cancer	HCT-116	GI50	5.41
Colon Cancer	HCT-116	IC50	5.31
Colon Cancer	HCT-116	LC50	4
Colon Cancer	HCT-116	TGI	4.49
Colon Cancer	HCT-15	GI50	4.58
Colon Cancer	HCT-15	IC50	4.43
Colon Cancer	HCT-15	LC50	4
Colon Cancer	HCT-15	TGI	4
Colon Cancer	HT29	GI50	5.21
Colon Cancer	HT29	IC50	5.04
Colon Cancer	HT29	LC50	4
Colon Cancer	HT29	TGI	4.45
Colon Cancer	KM12	GI50	4.77
Colon Cancer	KM12	IC50	4.53
Colon Cancer	KM12	LC50	4.16
Colon Cancer	KM12	TGI	4.46
Colon Cancer	SW-620	GI50	5.98
Colon Cancer	SW-620	IC50	5.81
Colon Cancer	SW-620	LC50	4
Colon Cancer	SW-620	TGI	5.31
CNS Cancer	SF-268	GI50	6.19
CNS Cancer	SF-268	IC50	5.85
CNS Cancer	SF-268	LC50	0
CNS Cancer	SF-268	TGI	5.63
CNS Cancer	SF-295	GI50	4.65

CNS Cancer	SF-295	IC50	4.33
CNS Cancer	SF-295	LC50	4
CNS Cancer	SF-295	TGI	4.07
CNS Cancer	SF-539	GI50	5.73
CNS Cancer	SF-539	IC50	5.43
CNS Cancer	SF-539	LC50	0
CNS Cancer	SF-539	TGI	5.37
CNS Cancer	SNB-19	GI50	5.07
CNS Cancer	SNB-19	IC50	4.77
CNS Cancer	SNB-19	LC50	4.26
CNS Cancer	SNB-19	TGI	4.64
CNS Cancer	SNB-75	GI50	5.32
CNS Cancer	SNB-75	IC50	4.15
CNS Cancer	SNB-75	LC50	4
CNS Cancer	SNB-75	TGI	4.41
CNS Cancer	U251	GI50	5.83
CNS Cancer	U251	IC50	5.59
CNS Cancer	U251	LC50	4.95
CNS Cancer	U251	TGI	5.41
Melanoma	LOX IMVI	GI50	5.97
Melanoma	LOX IMVI	IC50	5.76
Melanoma	LOX IMVI	LC50	4
Melanoma	LOX IMVI	TGI	4
Melanoma	MALME-3M	GI50	5.28
Melanoma	MALME-3M	IC50	4
Melanoma	MALME-3M	LC50	4
Melanoma	MALME-3M	TGI	4
Melanoma	M14	GI50	4.75
Melanoma	M14	IC50	4.42
Melanoma	M14	LC50	4
Melanoma	M14	TGI	4
Melanoma	MDA-MB-435	GI50	4.77
Melanoma	MDA-MB-435	IC50	4.54
Melanoma	MDA-MB-435	LC50	4
Melanoma	MDA-MB-435	TGI	4
Melanoma	SK-MEL-2	GI50	4.66
Melanoma	SK-MEL-2	IC50	4
Melanoma	SK-MEL-2	LC50	4
Melanoma	SK-MEL-2	TGI	4
Melanoma	SK-MEL-28	GI50	4.89
Melanoma	SK-MEL-28	IC50	4.47
Melanoma	SK-MEL-28	LC50	4
Melanoma	SK-MEL-28	TGI	4.35

Melanoma	SK-MEL-5	GI50	5.55
Melanoma	SK-MEL-5	IC50	5.26
Melanoma	SK-MEL-5	LC50	4
Melanoma	SK-MEL-5	TGI	4.44
Melanoma	UACC-257	GI50	4.87
Melanoma	UACC-257	IC50	4
Melanoma	UACC-257	LC50	4
Melanoma	UACC-257	TGI	4
Melanoma	UACC-62	GI50	5.21
Melanoma	UACC-62	IC50	4.73
Melanoma	UACC-62	LC50	4
Melanoma	UACC-62	TGI	4.28
Ovarian Cancer	IGROV1	GI50	5.67
Ovarian Cancer	IGROV1	IC50	5.33
Ovarian Cancer	IGROV1	LC50	4
Ovarian Cancer	IGROV1	TGI	4
Ovarian Cancer	OVCAR-3	GI50	5.67
Ovarian Cancer	OVCAR-3	IC50	5.37
Ovarian Cancer	OVCAR-3	LC50	4
Ovarian Cancer	OVCAR-3	TGI	
Ovarian Cancer	OVCAR-4	GI50	4.77
Ovarian Cancer	OVCAR-4	IC50	4.48
Ovarian Cancer	OVCAR-4	LC50	4.15
Ovarian Cancer	OVCAR-4	TGI	4.46
Ovarian Cancer	OVCAR-5	GI50	4.65
Ovarian Cancer	OVCAR-5	IC50	4.38
Ovarian Cancer	OVCAR-5	LC50	4.05
Ovarian Cancer	OVCAR-5	TGI	4.35
Ovarian Cancer	OVCAR-8	GI50	5.51
Ovarian Cancer	OVCAR-8	IC50	5.3
Ovarian Cancer	OVCAR-8	LC50	4
Ovarian Cancer	OVCAR-8	TGI	4
Ovarian Cancer	NCI/ADR-RES	GI50	4
Ovarian Cancer	NCI/ADR-RES	IC50	4
Ovarian Cancer	NCI/ADR-RES	LC50	4
Ovarian Cancer	NCI/ADR-RES	TGI	4
Ovarian Cancer	SK-OV-3	GI50	4.57
Ovarian Cancer	SK-OV-3	IC50	4.21
Ovarian Cancer	SK-OV-3	LC50	4
Ovarian Cancer	SK-OV-3	TGI	4.06
Renal Cancer	786-0	GI50	5.66
Renal Cancer	786-0	IC50	5.4
Renal Cancer	786-0	LC50	0

Renal Cancer	786-0	TGI	
Renal Cancer	A498	GI50	4.43
Renal Cancer	A498	IC50	4
Renal Cancer	A498	LC50	4
Renal Cancer	A498	TGI	4
Renal Cancer	ACHN	GI50	4.35
Renal Cancer	ACHN	IC50	4.05
Renal Cancer	ACHN	LC50	4
Renal Cancer	ACHN	TGI	4
Renal Cancer	CAKI-1	GI50	4
Renal Cancer	CAKI-1	IC50	4
Renal Cancer	CAKI-1	LC50	4
Renal Cancer	CAKI-1	TGI	4
Renal Cancer	RXF 393	GI50	6.4
Renal Cancer	RXF 393	IC50	5.88
Renal Cancer	RXF 393	LC50	4
Renal Cancer	RXF 393	TGI	
Renal Cancer	SN12C	GI50	5.77
Renal Cancer	SN12C	IC50	5.5
Renal Cancer	SN12C	LC50	4.37
Renal Cancer	SN12C	TGI	5.31
Renal Cancer	TK-10	GI50	4.33
Renal Cancer	TK-10	IC50	4
Renal Cancer	TK-10	LC50	4
Renal Cancer	TK-10	TGI	4
Renal Cancer	UO-31	GI50	4
Renal Cancer	UO-31	IC50	4
Renal Cancer	UO-31	LC50	4
Renal Cancer	UO-31	TGI	4
Prostate Cancer	PC-3	GI50	4.86
Prostate Cancer	PC-3	IC50	4.44
Prostate Cancer	PC-3	LC50	4
Prostate Cancer	PC-3	TGI	4
Prostate Cancer	DU-145	GI50	5.47
Prostate Cancer	DU-145	IC50	5.15
Prostate Cancer	DU-145	LC50	4
Prostate Cancer	DU-145	TGI	4
Breast Cancer	MCF7	GI50	5.14
Breast Cancer	MCF7	IC50	4.83
Breast Cancer	MCF7	LC50	4.15
Breast Cancer	MCF7	TGI	4.6
Breast Cancer	MDA-MB-231/ATCC	GI50	4.92
Breast Cancer	MDA-MB-231/ATCC	IC50	4

Breast Cancer	MDA-MB-231/ATCC	LC50	4
Breast Cancer	MDA-MB-231/ATCC	TGI	4
Breast Cancer	HS 578T	GI50	4
Breast Cancer	HS 578T	IC50	4
Breast Cancer	HS 578T	LC50	4
Breast Cancer	HS 578T	TGI	4
Breast Cancer	BT-549	GI50	5.81
Breast Cancer	BT-549	IC50	5.46
Breast Cancer	BT-549	LC50	0
Breast Cancer	BT-549	TGI	5.46
Breast Cancer	T-47D	GI50	5.79
Breast Cancer	T-47D	IC50	4.72
Breast Cancer	T-47D	LC50	4
Breast Cancer	T-47D	TGI	4.59
Breast Cancer	MDA-MB-468	GI50	5.95
Breast Cancer	MDA-MB-468	IC50	5.59
Breast Cancer	MDA-MB-468	LC50	5.06
Breast Cancer	MDA-MB-468	TGI	5.51

Table S7. NCI-60 cytotoxicity data for the most sensitive cell lines to compound **3**. (IC_{50}, compound concentration inducing 100% growth inhibition.)

Cancer	**Cell Line**	**IC_{50}/μM**
non-small cell lung	NCI-H522	0.28
renal	RXF 393	1.3
central nervous system	SF-268	1.4
colon	SW-620	1.5
melanoma	LOX IMVI	1.7
central nervous system	U251	2.6
breast	MDA-MB-468	2.6
renal	SN12C	3.2
breast	BT-549	3.5
central nervous system	SF-539	3.7
non-small cell lung	HOP-62	4.0
renal	786-0	4.0
ovarian	OVCAR-3	4.3
leukemia	HL-60(TB)	4.7
ovarian	IGROV1	4.7
colon	HCT-116	4.9

Table S8. Cartesian coordinates and thermochemical parameters of the lowest-energy conformations of **1**–**3** calculated by DFT methods (PBE1PBE/LANL2DZ).

Compound 1

Center Number	Atomic Number	Atomic Type	Coordinates (Angstroms) X	Y	Z
1	79	0	14.571989	-15.670925	-0.059621
2	6	0	16.477032	-8.465192	0.451811
3	6	0	15.691079	-9.642863	0.321254
4	6	0	15.847676	-7.235083	0.479843
5	6	0	14.263720	-9.542189	0.220577
6	6	0	14.424363	-7.134693	0.379450
7	6	0	13.639508	-8.265055	0.251670
8	7	0	16.275799	-10.863685	0.290727
9	6	0	15.548964	-11.993976	0.169306
10	7	0	13.524267	-10.669613	0.096647
11	6	0	14.095869	-11.891484	0.066799
12	6	0	13.055899	-12.921714	-0.075868
13	6	0	11.879706	-14.839502	-0.260998
14	7	0	13.159635	-14.283232	-0.119897
15	6	0	10.940784	-13.781840	-0.308503
16	6	0	11.665334	-12.598674	-0.192854
17	6	0	16.444476	-13.160717	0.163101
18	6	0	17.869105	-13.036238	0.244651
19	6	0	18.430275	-14.310088	0.219657
20	7	0	16.158764	-14.494766	0.091594
21	6	0	17.355488	-15.225719	0.125138
22	6	0	11.828061	-16.239272	-0.314804
23	7	0	12.980638	-16.903786	-0.238130
24	6	0	17.218118	-16.619442	0.065273
25	7	0	15.984722	-17.115670	-0.026293
26	6	0	13.097517	-18.364961	-0.222666
27	6	0	14.403524	-18.858752	-0.859118
28	6	0	15.663897	-18.545971	-0.041692
29	1	0	17.554268	-8.564581	0.526589
30	1	0	16.434524	-6.327421	0.579311
31	1	0	13.961963	-6.153025	0.404907
32	1	0	12.559171	-8.212266	0.174263
33	1	0	9.870022	-13.881460	-0.412711
34	1	0	11.291405	-11.589013	-0.185794
35	1	0	18.375705	-12.088684	0.313825
36	1	0	19.480581	-14.559312	0.265037
37	1	0	10.889694	-16.779220	-0.415376
38	1	0	18.076628	-17.286127	0.091409
39	1	0	13.036473	-18.723661	0.815229
40	1	0	12.246240	-18.787693	-0.771134
41	1	0	14.332925	-19.949084	-0.948512
42	1	0	14.503468	-18.457440	-1.875029
43	1	0	15.528699	-18.899440	0.990974
44	1	0	16.515951	-19.088845	-0.470044

```
Zero-point correction=                           0.345660 (Hartree/Particle)
 Thermal correction to Energy=                    0.365520
 Thermal correction to Enthalpy=                  0.366464
 Thermal correction to Gibbs Free Energy=         0.297053
 Sum of electronic and zero-point Energies=          -1271.759505
 Sum of electronic and thermal Energies=             -1271.739644
 Sum of electronic and thermal Enthalpies=           -1271.738700
 Sum of electronic and thermal Free Energies=        -1271.808112
```

Compound 2

Center Number	Atomic Number	Atomic Type	Coordinates (Angstroms) X	Y	Z
1	6	0	-4.792669	-0.717112	0.066927
2	6	0	-4.792680	0.717075	0.066731
3	6	0	-6.025176	-1.425665	0.086773
4	6	0	-6.025197	1.425614	0.086356
5	6	0	-7.210522	-0.715158	0.105454
6	6	0	-7.210533	0.715094	0.105238
7	6	0	-2.432730	-0.730545	0.026879
8	6	0	-2.432736	0.730533	0.026766
9	7	0	-3.613469	-1.382773	0.048378
10	7	0	-3.613488	1.382746	0.048064
11	6	0	-1.329330	1.703604	0.014698
12	6	0	-1.329318	-1.703601	0.014791
13	6	0	-1.547231	-3.117411	0.080842
14	6	0	-0.312747	-3.761408	0.041931
15	6	0	0.671230	-2.748837	-0.051034
16	7	0	0.019935	-1.506895	-0.064403
17	6	0	-1.547280	3.117426	0.080517
18	6	0	-0.312791	3.761428	0.042128
19	7	0	0.019938	1.506923	-0.064254
20	6	0	0.671219	2.748877	-0.050787
21	6	0	2.070982	-2.701262	-0.137387
22	7	0	2.646468	-1.502718	-0.214013
23	6	0	2.070972	2.701317	-0.137064
24	7	0	2.646454	1.502758	-0.213655
25	6	0	4.083066	-1.278343	-0.382864
26	6	0	4.083043	1.278383	-0.382629
27	6	0	4.622482	-0.000040	0.307142
28	6	0	4.313036	-0.000204	1.812541
29	6	0	6.150347	0.000008	0.092081
30	79	0	1.300012	0.000021	-0.161119
31	1	0	-6.001648	-2.509814	0.086219
32	1	0	-6.001686	2.509764	0.085492
33	1	0	-8.159131	-1.242484	0.120489
34	1	0	-8.159150	1.242410	0.120109
35	1	0	-2.525860	-3.561749	0.146266
36	1	0	-0.133722	-4.826423	0.074039
37	1	0	-2.525936	3.561746	0.145668
38	1	0	-0.133778	4.826443	0.074313
39	1	0	2.679389	-3.602351	-0.146222
40	1	0	2.679410	3.602384	-0.145772
41	1	0	4.314723	-1.225505	-1.457366
42	1	0	4.617689	-2.144720	0.029770
43	1	0	4.314631	1.225725	-1.457154
44	1	0	4.617686	2.144685	0.030134
45	1	0	4.748079	0.883861	2.292980
46	1	0	4.747951	-0.884445	2.292761
47	1	0	3.238423	-0.000110	2.026758
48	1	0	6.607030	-0.882924	0.552825
49	1	0	6.414487	0.000221	-0.973128
50	1	0	6.607007	0.882738	0.553224

Zero-point correction= 0.401532 (Hartree/Particle)
Thermal correction to Energy= 0.424419
Thermal correction to Enthalpy= 0.425363
Thermal correction to Gibbs Free Energy= 0.349904
Sum of electronic and zero-point Energies= -1350.224725
Sum of electronic and thermal Energies= -1350.201837
Sum of electronic and thermal Enthalpies= -1350.200893
Sum of electronic and thermal Free Energies= -1350.276352

Compound 3

Center Number	Atomic Number	Atomic Type	Coordinates (Angstroms) X	Y	Z
1	79	0	1.501871	0.031488	-0.111876
2	6	0	-5.885835	1.372644	0.011912
3	6	0	-4.644029	0.679804	0.027901
4	6	0	-7.061439	0.650106	0.086252
5	6	0	-4.625841	-0.752140	0.115411
6	6	0	-7.043103	-0.777338	0.178901
7	6	0	-5.849211	-1.472977	0.193657
8	7	0	-3.473760	1.357475	-0.031804
9	6	0	-2.285914	0.716844	-0.020552
10	7	0	-3.439141	-1.403283	0.115291
11	6	0	-2.268222	-0.736188	0.042571
12	6	0	-1.148391	-1.685766	0.029538
13	6	0	0.846277	-2.727391	-0.069697
14	7	0	0.203434	-1.480629	-0.065352
15	6	0	-0.131200	-3.741731	0.030103
16	6	0	-1.363258	-3.098972	0.092979
17	6	0	-1.188209	1.690952	-0.064294
18	6	0	-1.436851	3.099434	-0.095695
19	6	0	-0.217037	3.768319	-0.105411
20	7	0	0.171308	1.514721	-0.060208
21	6	0	0.785766	2.774244	-0.084013
22	6	0	2.236570	-2.695087	-0.207003
23	7	0	2.834823	-1.507525	-0.265437
24	6	0	2.182878	2.773504	-0.050392
25	7	0	2.815814	1.602309	-0.048565
26	6	0	4.262198	-1.372646	-0.581189
27	6	0	5.123114	-0.873390	0.583685
28	6	0	4.677102	0.469398	1.183878
29	6	0	4.276816	1.524117	0.136056
30	1	0	-5.876594	2.454830	-0.056706
31	1	0	-8.016676	1.165446	0.075756
32	1	0	-7.984772	-1.314027	0.237025
33	1	0	-5.811890	-2.554658	0.260818
34	1	0	0.052030	-4.806241	0.050246
35	1	0	-2.341761	-3.541481	0.168219
36	1	0	-2.427298	3.521236	-0.102061
37	1	0	-0.057877	4.836703	-0.125285
38	1	0	2.826178	-3.604601	-0.292208
39	1	0	2.751528	3.698901	-0.002932
40	1	0	4.633931	-2.351026	-0.912014
41	1	0	4.355444	-0.701330	-1.443477
42	1	0	5.150966	-1.632197	1.374526
43	1	0	6.147946	-0.781199	0.199733
44	1	0	3.836586	0.323842	1.873898
45	1	0	5.498100	0.864997	1.792009
46	1	0	4.616920	2.516790	0.454221
47	1	0	4.758992	1.320577	-0.828674

Zero-point correction= 0.374990 (Hartree/Particle)
Thermal correction to Energy= 0.396135
Thermal correction to Enthalpy= 0.397079
Thermal correction to Gibbs Free Energy= 0.324482
Sum of electronic and zero-point Energies= -1310.982047
Sum of electronic and thermal Energies= -1310.960902
Sum of electronic and thermal Enthalpies= -1310.959958
Sum of electronic and thermal Free Energies= -1311.032556

Table S9. Conformational changes to the 22-bp DNA duplex (see Figure S48) caused by major groove intercalation of **3** at the highlighted T10-A11 step for the lowest-energy (global minimum) conformation. The geometric and trigonometric data were calculated with W3DNA.[34,35]

Base pair	Shear (Å)	Stretch (Å)	Stagger (Å)	Buckle (°)	Propeller Twist (°)	Opening (°)	Shift (Å)	Slide (Å)	Rise (Å)	Tilt (°)	Roll (°)	Twist (°)
A-T	-0.2	0.3	-1.4	-3.2	-21.1	-17.4	0.0	0.0	0.0	0.0	0.0	0.0
A-T	-0.3	0.0	-0.7	-6.9	-20.0	3.9	1.3	0.9	3.2	-2.6	8.0	30.8
A-T	0.0	0.3	-0.5	8.3	-16.3	0.1	-0.1	0.4	2.8	-1.4	9.1	26.7
A-T	-0.2	0.2	-0.6	3.7	-26.0	-9.4	-0.2	0.6	3.2	-0.5	4.7	39.5
A-T	-0.3	0.2	-0.5	-4.1	-17.4	-5.2	-0.1	-0.2	3.3	-0.9	2.9	37.5
G-C	-0.4	0.2	0.2	-6.6	-11.2	-4.1	0.3	-0.9	3.3	-4.6	-0.4	33.0
A-T	1.1	0.0	0.7	-4.2	-16.5	-5.4	-0.6	-0.6	3.3	-3.0	-2.6	40.7
C-G	-0.4	0.2	0.5	4.6	-12.1	-1.0	0.6	-0.8	3.3	1.5	-10.0	28.3
T-A	-0.4	0.2	1.4	-12.3	-22.5	-4.4	0.0	-1.3	3.7	-3.4	3.0	37.4
T-A	1.2	-0.1	0.2	-12.5	-23.5	7.9	0.1	-0.4	3.4	9.1	-1.2	40.5
A-T	-0.7	0.1	0.1	-8.6	-5.6	3.4	0.7	1.0	7.2	-1.5	-10.8	31.0
G-C	-1.5	0.1	0.5	11.4	1.4	-1.3	-0.8	0.6	3.0	-3.4	0.6	27.0
A-T	0.2	0.4	0.4	10.5	-22.1	-1.1	0.1	-0.3	3.5	3.2	-1.1	45.8
A-T	-0.3	0.1	0.7	8.0	-20.1	-1.8	0.1	-0.9	3.2	-3.3	-2.3	30.8
A-T	0.8	0.3	-0.2	0.8	-25.6	-7.6	-0.8	-0.7	3.4	4.5	-0.9	41.5
A-T	0.0	0.2	-0.3	-2.5	-22.7	2.2	0.7	-0.3	3.2	2.9	-3.9	31.4
A-T	-0.1	0.1	-0.3	-9.3	-29.0	2.0	-0.2	0.0	3.2	-0.6	1.1	36.5
T-A	0.0	0.2	0.1	3.7	-25.5	-0.5	0.2	-1.1	2.8	-2.2	6.5	33.8
T-A	-1.0	0.2	0.2	-4.1	-28.3	-2.4	0.2	-0.2	3.3	-1.2	3.9	32.8
T-A	0.8	0.1	-0.3	-8.1	-14.1	0.6	-0.1	0.5	3.4	-0.1	-0.8	46.6
T-A	-0.5	0.5	0.5	-16.5	-26.4	10.0	-0.1	0.1	3.4	-6.0	-2.6	30.5
T-A	1.1	0.0	0.5	-11.7	-7.3	5.1	-0.5	0.0	3.3	-4.7	1.3	39.1
Sum	-1.1	3.9	1.0	-59.4	-411.9	-26.4	0.9	-3.5	**72.3**	-18.2	4.6	741.2
Ave.	-0.1	0.2	0.0	-2.7	-18.7	-1.2	0.0	-0.2	3.3	-0.8	0.2	33.7
s.u. (ave.)	0.7	0.1	0.6	8.1	7.9	6.0	0.5	0.6	1.1	3.5	4.9	9.4

Table S10. Conformational changes to the 22-bp DNA duplex caused by minor groove intercalation of **3** at the highlighted T10-A11 step for the lowest-energy minor groove intercalation adduct (see Figure S49). The geometric and trigonometric data were calculated with W3DNA.[34,35]

Base pair	Shear (Å)	Stretch (Å)	Stagger (Å)	Buckle (°)	Propeller Twist (°)	Opening (°)	Shift (Å)	Slide (Å)	Rise (Å)	Tilt (°)	Roll (°)	Twist (°)
A-T	0.3	0.2	-1.9	-8.3	-33.4	-16.6	0.0	0.0	0.0	0.0	0.0	0.0
A-T	-0.1	-0.2	-1.3	-5.6	-26.9	2.7	1.0	1.1	3.1	-2.2	4.3	30.3
A-T	0.2	0.5	-0.2	3.2	-14.1	0.1	-0.2	0.3	2.9	-10.0	9.4	26.5
A-T	-0.5	0.3	-0.5	-7.8	-29.9	-11.6	-0.4	0.3	3.5	-1.7	3.4	37.7
A-T	-0.7	0.1	0.1	-2.8	-15.8	-7.8	-0.2	-0.4	3.0	-3.5	-3.3	36.2
G-C	-0.1	0.3	0.6	-3.4	-16.2	-1.7	0.6	-1.0	3.2	-1.5	-4.4	36.4
A-T	1.0	-0.1	0.7	-2.0	-19.3	-8.5	-0.6	-0.7	3.1	-0.4	-1.4	39.5
C-G	0.1	0.5	0.1	9.2	-22.4	-1.2	0.8	-0.5	3.3	4.4	-10.0	29.9
T-A	-0.4	0.0	1.3	-15.8	-22.2	-5.7	0.0	-1.5	4.2	-2.0	2.4	36.0
T-A	1.6	-0.1	0.2	-6.9	-12.9	10.1	0.5	-0.2	3.1	8.3	-3.1	41.8
A-T	-1.0	0.3	0.5	-6.0	-6.8	1.3	0.6	0.6	7.0	-2.7	-0.9	24.6
G-C	-1.2	0.0	0.7	10.7	-2.8	-6.0	-1.1	0.5	3.1	-1.9	-10.3	32.3
A-T	1.1	0.6	0.6	12.4	-29.5	-3.1	0.4	-0.2	3.7	8.2	-2.8	47.3
A-T	0.0	0.2	0.1	4.3	-25.2	-1.4	0.2	-1.1	3.2	1.5	3.2	29.0
A-T	0.7	0.3	-0.1	0.7	-23.0	-10.1	-0.7	-0.6	3.2	0.2	-0.1	38.7
A-T	0.2	0.1	-0.2	-3.8	-23.9	0.4	0.7	-0.3	3.3	5.2	-4.0	34.3
A-T	0.1	0.1	-0.5	-12.4	-28.3	-5.0	-0.3	-0.1	3.4	0.0	0.7	35.8
T-A	-0.6	0.2	-0.1	2.4	-29.0	5.8	0.7	-1.2	2.7	-0.8	5.9	30.0
T-A	-1.1	0.2	-0.1	-6.2	-27.7	-1.9	0.1	-0.2	3.2	0.6	8.4	34.5
T-A	0.8	0.1	-0.1	-12.7	-16.5	0.5	-0.2	0.6	3.5	-2.1	-2.3	48.5
T-A	-0.8	0.4	0.5	-14.7	-29.8	10.8	0.0	0.1	3.2	-7.2	2.4	28.3
T-A	1.2	0.0	0.2	-10.0	-11.4	-0.2	-0.7	0.0	3.2	-3.2	1.5	40.7
Sum	0.8	3.8	0.5	-75.3	-466.8	-49.3	1.1	-4.3	**71.9**	-11.0	-1.1	738.4
Ave.	0.0	0.2	0.0	-3.4	-21.2	-2.2	0.1	-0.2	3.3	-0.5	-0.1	33.6
s.u. (ave.)	0.8	0.2	0.7	8.0	8.2	6.6	0.6	0.6	1.1	4.3	5.0	9.7

Table S11. Conformational of the lowest-energy structure of the 22-bp DNA duplex used for macromolecular simulations in this study. The geometric and trigonometric data were calculated with W3DNA[34,35] and serve as the reference for the intercalator-free 22-bp oligonucleotide. The DNA sequence is that given in Figure S48.

Base pair	Shear (Å)	Stretch (Å)	Stagger (Å)	Buckle (°)	Propeller Twist (°)	Opening (°)	Shift (Å)	Slide (Å)	Rise (Å)	Tilt (°)	Roll (°)	Twist (°)
A-T	-0.6	0.1	-0.3	-8.3	-8.3	-7.3	0.0	0.0	0.0	0.0	0.0	0.0
A-T	-0.1	0.3	-0.1	-2.1	-10.5	-9.2	-0.1	-0.3	3.2	-0.2	-2.6	38.5
A-T	0.1	0.3	-0.1	0.7	-12.6	-10.1	-0.1	-0.4	3.3	0.5	-3.4	37.0
A-T	0.1	0.3	0.0	1.7	-13.5	-10.3	0.0	-0.4	3.3	0.3	-3.2	36.3
A-T	0.1	0.3	0.3	3.1	-13.3	-10.9	0.0	-0.5	3.3	-0.3	-4.1	35.8
G-C	-0.4	0.2	0.4	1.0	-11.4	-8.6	0.2	-0.6	3.4	1.1	-5.1	32.8
A-T	0.0	0.3	0.6	2.8	-11.9	-11.8	0.0	-0.4	3.3	0.0	-3.4	38.6
C-G	0.3	0.2	0.7	-2.2	-9.4	-9.0	0.0	-0.7	3.5	-1.8	-1.5	36.5
T-A	-0.1	0.3	0.5	-3.5	-13.2	-11.5	-0.2	-0.7	3.4	0.2	-6.5	33.8
T-A	0.1	0.3	0.4	-1.7	-11.2	-10.8	0.1	-0.6	3.3	0.8	-5.2	35.6
A-T	-0.1	0.3	0.4	2.0	-9.5	-10.6	0.0	-0.3	3.2	-0.1	-5.5	36.9
G-C	-0.4	0.2	0.2	1.1	-9.5	-8.2	0.2	-0.5	3.4	2.5	-6.1	33.0
A-T	0.0	0.3	-0.1	-0.1	-13.2	-10.8	0.1	-0.3	3.4	3.1	-1.3	39.0
A-T	0.1	0.3	-0.1	1.9	-13.8	-10.2	0.1	-0.4	3.3	0.3	-2.6	35.8
A-T	0.1	0.3	0.0	2.7	-14.4	-10.4	0.0	-0.4	3.3	0.6	-2.9	35.8
A-T	0.1	0.3	0.2	3.3	-14.8	-10.9	0.0	-0.5	3.3	-0.1	-3.4	35.7
A-T	0.1	0.3	0.5	3.6	-12.8	-11.1	0.0	-0.6	3.3	-1.9	-4.0	35.9
T-A	-0.1	0.3	0.6	-3.3	-12.8	-11.1	0.0	-0.8	3.6	-0.1	-3.9	34.0
T-A	-0.1	0.3	0.2	-2.6	-14.1	-10.9	0.0	-0.6	3.3	1.8	-4.3	36.0
T-A	0.0	0.3	0.0	-1.1	-13.0	-10.3	0.0	-0.5	3.3	0.2	-3.8	36.2
T-A	0.1	0.3	-0.1	2.1	-10.5	-9.2	0.1	-0.4	3.3	-0.3	-3.6	36.9
T-A	0.7	0.1	-0.3	8.4	-8.2	-6.9	0.2	-0.3	3.2	0.3	-2.8	38.5
Sum	-0.2	5.9	3.7	9.5	-261.9	-219.9	0.5	-10.0	**69.8**	7.0	-79.2	758.5
Ave.	0.0	0.3	0.2	0.4	-11.9	-10.0	0.0	-0.5	3.2	0.3	-3.6	34.5
s.u. (ave.)	0.3	0.1	0.3	3.4	2.0	1.3	0.1	0.2	0.7	1.1	1.5	7.9

Table S12. High resolution melting point data for a 291-bp dsDNA fragment (amplicon) derived from real-time PCR of a portion of the human gene ACTN3 corresponding to exon 15 vs. compound concentration.

[**1**]/M	*T*m(**1**)/°C	[**2a**]/M	*T*m(**2a**)/°C	[**3**]/M	*T*m(**3**)/°C	[**6**]/M	*T*m(**6**)/°C
5.10E-05	87.25	5.05E-05	86.75	5.20E-05	87.25	1.35E-04	82.85
1.02E-05	85.75	1.01E-05	85.00	1.04E-05	84.80	2.65E-05	82.95
2.04E-06	83.95	2.02E-06	83.90	2.08E-06	83.85	5.3E-06	82.95
4.08E-07	83.30	4.04E-07	83.37	4.16E-07	83.50	1.06E-06	83.35
8.16E-08	83.10	8.08E-08	83.13	8.32E-08	83.00	2.12E-07	82.95
0	82.85	0	82.85	0	82.85	0	82.85

4. References and Notes

(1) Wang, L.; Zhu, X. J.; Wong, W. Y.; Guo, J. P.; Wong, W. K.; Li, Z. Y. *Dalton Trans.* **2005**, 3235-3240.

(2) Munro, O. Q., Akerman, M. P., Akerman, K. J.: Gold Complexes. In *WIPO*; A61K 31/28 (2006.01) ed.; WIPO, Ed.; University of KwaZulu-Natal: PCT/IB2011/052572, 2011.

(3) Felsenfeld, G.; Hirschman, S. Z. *J. Mol. Biol.* **1965**, *13*, 407-427.

(4) Marmur, J. *J. Mol. Biol.* **1961**, *3*, 208-218.

(5) Chen, L.-M.; Liu, J.; Chen, J.-C.; Tan, C.-P.; Shi, S.; Zheng, K.-C.; Ji, L.-N. *J. Inorg. Biochem.* **2008**, *102*, 330-341.

(6) CrysAlis-RED. **2010**.

(7) Sheldrick, G. M. *Acta Crystallogr., Sect. A* **2008**, *64*, 112-122.

(8) Dolomanov, O. V.; Bourhis, L. J.; Gildea, R. J.; Howard, J. A. K.; Puschmann, H. *J. Appl. Crystallogr.* **2009**, *42*, 339-341.

(9) Spek, A. *Acta Crystallogr., Sect. A* **1990**, *46*, c34.

(10) Schneider, C. A.; Rasband, W. S.; Eliceiri, K. W. *Nat. Methods* **2012**, *9*, 671-675.

(11) Cyril, V.; Muller, M. T. *Anal. Biochem.* **2012**, *421*, 607-616.

(12) Wilson, C. R.; Fagenson, A. M.; Ruangpradit, W.; Muller, M. T.; Munro, O. Q. *Inorg. Chem.* **2013**, *52*, 7889-7906.

(13) Mills, M.; Yang, N.; Weinberger, R.; Vander Woude, D. L.; Beggs, A. H.; Easteal, S.; North, K. *Human Mol. Genetics* **2001**, *10*, 1335-1346.

(14) Maciejewska, A.; Sawczuk, M.; Cieszczyk, P.; Mozhayskaya, I. A.; Ahmetov, I. I. *J. Sports Sci.* **2012**, *30*, 101-113.

(15) Pereira, A.; Costa, A.; Leitao, J.; Monteiro, A.; Izquierdo, M.; Silva, A.; Bastos, E.; Marques, M. *BMC Geriatrics* **2013**, *13*, 131.

(16) Tran, N. T.; Wang, T. H.; Lin, C. Y.; Tsai, Y. C.; Lai, C. H.; Tai, Y.; Yung, B. Y. *Bioconjug. Chem.* **2011**, *22*, 1394-1401.

(17) Inc., K.: KyPlot 5.0.2: Data Analysis and Visualization. 5.0.2 ed.; KyenceLab Inc., 2011; pp Statistical and graphing software.

(18) Weber, I. T.; Harrison, R. W. *Protein Eng.* **1999**, *12*, 469-474.

(19) Pedretti, A.; Villa, L.; Vistoli, G. *J. Comput.-Aided Mol. Design* **2004**, *18*, 167-173.

(20) Martin, L. Y.; DeHayes, L. J.; Zompa, L. J.; Busch, D. H. *J. Am. Chem. Soc.* **1974**, *96*, 4046-4048.

(21) Narayana, N.; Weiss, M. A. *J. Mol. Biol.* **2009**, *385*, 469-490.

(22) Redinbo, M. R.; Stewart, L.; Kuhn, P.; Champoux, J. J.; Hol, W. G. *Science* **1998**, *279*, 1504-1513.

(23) Huang, Y.; Kowalski, D. *Nucleic Acids Res.* **2003**, *31*, 3819-3821.

(24) Frisch, M. J. T., G. W.; Schlegel, H. B.; Scuseria, G. E.; Robb, M. A.; Cheeseman, J. R.; Scalmani, G.; Barone, V.; Mennucci, B.; Petersson, G. A.; Nakatsuji, H.; Caricato, M.; Li, X.; Hratchian, H. P.; Izmaylov, A. F.; Bloino, J.; Zheng, G.; Sonnenberg, J. L.; Hada, M.; Ehara, M.; Toyota, K.; Fukuda, R.; Hasegawa, J.; Ishida, M.; Nakajima, T.; Honda, Y.; Kitao, O.; Nakai, H.; Vreven, T.; Montgomery, Jr., J. A.; Peralta, J. E.; Ogliaro, F.; Bearpark, M.; Heyd, J. J.; Brothers, E.; Kudin, K. N.; Staroverov, V. N.; Kobayashi, R.; Normand, J.; Raghavachari, K.; Rendell, A.; Burant, J. C.; Iyengar, S. S.; Tomasi, J.; Cossi, M.; Rega, N.; Millam, J. M.; Klene, M.; Knox, J. E.; Cross, J. B.; Bakken, V.; Adamo, C.; Jaramillo, J.; Gomperts, R.; Stratmann, R. E.; Yazyev, O.; Austin, A. J.; Cammi, R.; Pomelli, C.; Ochterski, J. W.; Martin, R. L.; Morokuma, K.; Zakrzewski, V. G.; Voth, G. A.; Salvador, P.; Dannenberg, J. J.; Dapprich, S.; Daniels, A. D.; Farkas, Ö.; Foresman, J. B.; Ortiz, J. V.; Cioslowski, J.; Fox, D. J. **2009**.

(25) Becke, A. D. *J. Chem. Phys.* **1993**, *98*, 5648-5652.

(26) McLean, A. D.; Chandler, G. S. *J. Chem. Phys.* **1980**, *72*, 5639-5648.

(27) Adamo, C.; Barone, V. *J. Chem. Phys.* **1999**, *110*, 6158-6169.

(28) Hay, P. J.; Wadt, W. R. *J. Chem. Phys.* **1985**, *82*, 270-283.

(29) Dennington, R.; Keith, T.; Millam, J. *Semichem Inc.* **2009**.

(30) Ditchfield, R. *Mol. Phys.* **1974**, *27*, 789-807.
(31) Pommier, Y.; Covey, J. M.; Kerrigan, D.; Markovits, J.; Pham, R. *Nucleic Acids Res.* **1987**, *15*, 6713-6731.
(32) Fujii, N.; Yamashita, Y.; Saitoh, Y.; Nakano, H. *J. Biol. Chem.* **1993**, *268*, 13160-13165.
(33) Breslauer, K. J.; Frank, R.; Blocker, H.; Marky, L. A. *Proc. Natl. Acad. Sci. USA* **1986**, *83*, 3746-3750.
(34) Lu, X. J.; Olson, W. K. *Nucleic Acids Res.* **2003**, *31*, 5108-5121.
(35) Zheng, G.; Lu, X.-J.; Olson, W. K. *Nucleic Acids Res.* **2009**, *37*, W240-W246.